MEMORY AND COUPLING IN NANOCRYSTAL OPTOELECTRONIC DEVICES

Jessamyn A. Fairfield

A DISSERTATION

in

Physics and Astronomy

Presented to the Faculties of the University of Pennsylvania in Partial Fulfillment of the Requirements for the Degree of Doctor of Philosophy

2011

Supervisor of Dissertation

_____

Marija Drndic, Associate Professor, Physics and Astronomy

Graduate Group Chairperson

_____

Alan T. Johnson, Professor, Physics and Astronomy

Dissertation Committee:

Marija Drndic, Associate Professor
Charles Kane, Professor
Randall Kamien, Professor
Alan T. Johnson, Professor
Joshua Klein, Associate Professor

Acknowledgments

Experimental scientific work is often a collaboration, and with that in mind I would like to thank Lauren Willis for TEM imaging, e-beam lithography, lots of advice on fabrication processes, and many scientific discussions; Matt Puster for e-beam lithography and brainstorming; Tali Dadosh for e-beam lithography, tips on how to do good optical lithography, and advice about experimental directions; Chris Merchant for career advice and processing aid; and Michael Fischbein for original Labview code as well as tips on doing AFM and EFM. I have also gotten excellent advice about experiments and scientific writing from Professor Jay Kikkawa, and useful advice about working with nanocrystals from Professor Chris Murray. And of course, my advisor, Professor Marija Drndic, has taught me a lot about science, writing, funding, and experiments in my time at Penn.

Many people read this manuscript and provided thoughtful comments, such as my advisor, coworkers, friends, parents, and step-parents. I appreciate every fresh eye that found something I missed, somewhere I misspoke, or some error I made.

I'm also very grateful for the many longtime friends I had at other schools who were going through the graduate school grind at the same time as I was and could commiserate: Juhi Saha, Jessica Richman, Scott McCalla, Stephanie "Field" McCalla, Andrew Marshall, and Jeanine Wood, you all helped keep me sane. And to my friends here who listened to me as I tried to sort out what grad school was supposed to be about, such as Rose Mutiso, Vicky Doan-Nguyen, Michael Turk, Patrick Vora, Aline Normoyle, and Jennifer Mosher, thank you. I also owe a great deal to my guitar teacher, Ron Bennett, and my unofficial ultrarunning coach, Melanie Lyon, for developing my outlets for the frustration of failed experiments or destroyed devices.

I got a lot of support and encouragement in this endeavor from the two people who have supported me for the longest time, and never stopped pushing me to succeed: my parents, Eric Fairfield and Peggy Hubbard.

And I really could not have done this without my partner in life, who is himself a very very recent Penn Ph.D. in computer science. Ben, thank you for being there for me through this experience. I'm very proud of you, and I am eternally glad that we walked this road together.

ABSTRACT

MEMORY AND COUPLING IN NANOCRYSTAL OPTOELECTRONIC DEVICES

Jessamyn A. Fairfield

Dr. Marija Drndic

Optoelectronic devices incorporating semiconducting nanocrystals are promising for many potential applications. Nanocrystals whose size is below the exciton Bohr radius have optical absorption and emission that is tunable with size, due to the quantum confinement of the charge carriers. However, the same confinement that yields these optical properties also makes electrical conduction in a film of nanocrystals occur via tunneling, due to the high energy barrier between nanocrystals. Hence, the extraction of photo-generated charge carriers presents a significant challenge. Several approaches to optimizing the reliability and efficiency of optoelectronic devices using semiconducting nanocrystals are explored herein. Force microscopy is used to investigate charge behavior in nanocrystal films. Plasmonic structures are lithographically defined to enhance electric field and thus charge collection efficiency in two-electrode nanocrystal devices illuminated at plasmonically resonant wavelengths. Graphene substrates are shown to couple electronically with nanocrystal films, improving device conduction while maintaining carrier quantum confinement within the nanocrystal. And finally, the occupancy of charge carrier traps is shown to both directly impact the temperature-

dependent photocurrent behavior, and be tunable using a combination of illumination and electric field treatments. Trap population manipulation is robustly demonstrated and verified using a variety of wavelength, intensity, and time-dependent measurements of photocurrent in nanogap nanocrystal devices, emphasizing the importance of measurement history and the possibility of advanced device behavior tuning based on desired operating conditions. Each of these experiments reveals a path toward understanding and optimizing semiconducting nanocrystal optoelectronic devices.

Table of Contents

Acknowledgments ii
ABSTRACT iv
Table of Contents vi
List of Tables ix
List of Figures x
1 Introduction 1
1.1 Semiconducting Nanocrystals 1
1.2 Optoelectronic Measurements 2
1.3 Extracting the Physics 3
1.4 Scope of This Work 5
2 Nanocrystals: Scientific Background 6
Summary 6
2.1 Synthesis and Characterization 7
2.2 Quantum Properties 12
2.3 Optical Properties 14
2.4 Electronic Properties 18
2.5 Charge Localization and Trapping 19
2.6 Conduction in Nanocrystal Solids 21
2.7 Photocurrent in Nanocrystal Solids 24
3 Experimental Techniques 26
Summary 26
3.1 Membrane Fabrication 26
3.2 Electrode Fabrication 28
3.3 Nanocrystal Size Measurement 30
3.4 Device Integration 32

3.5 Two-electrode Measurements 33
3.6 Dark Current Measurements 36
3.7 Vacuum and Temperature Considerations....40
3.8 Annealing and Improving Conduction 41
4 Force Microscopy Studies 44
Summary 44
4.1 Atomic Force Microscopy 44
4.2 Blinking and AFM/TEM Correlations....45
4.3 Electrostatic Force Microscopy....48
4.4 EFM of Semiconducting Nanocrystals....49
4.5 EFM of Metal Nanocrystals....55
5 Plasmonic Field Enhancement....58
Summary 58
5.1 Plasmon Resonance in Nanoscale Metals....58
5.2 Theory of Plasmonic Response 60
5.3 Design of Plasmonic Metal Pillars 62
5.4 Photocurrent of Nanocrystals in Plasmonic Devices....64
6 Memory and Traps in Nanocrystal Films 68
Summary 68
6.1 Initial Measurements of Photocurrent Memory 70
6.2 Relative Photocurrent Ratio 78
6.3 Exciton Dynamics: Trap Manipulation....83
6.4 Illumination Intensity Measurements 87
6.5 Excitation and Treatment Wavelength Measurements....89
6.6 Photocurrent Behavior versus Treatment Time....93
6.7 Trap Population Manipulation Affects Photoconductivity 95
7 Coupling Nanocrystals to Graphene 97
Summary 97
7.1 Fluorescence Quenching....98
7.2 Absorption and Quantum Confinement....100

7.3 Graphene Nanoribbon Device 102
8 Conclusions 105
Bibliography 107

List of Tables

Table 6.1. Relative photocurrent ratios for several nanogap devices illuminated with 650 nm light, increasing or decreasing with different treatments. 82
Table 7.1. Mean fluorescence for mica/graphene/nanocrystal samples. 99

List of Figures

Figure 2.1.1. Synthesis diagram, showing nucleation, growth, and Ostwald ripening. 8
Figure 2.1.2. High-resolution TEM images of CdSe/ZnS nanocrystals on a carbon grid. 11
Figure 2.1.3. Wurtzite crystal structure.....12
Figure 2.3.1. Fluorescent emission of nanocrystals of various sizes. 15
Figure 2.3.2. Absorption and emission intensity vs. wavelength for nanocrystals studied. 16
Figure 3.1.1. (a) A schematic of a single SiN membrane and (b) a photograph of a wafer with many etch-defined chips and membranes. 27
Figure 3.2.1. Energy levels and work functions for 4 nm CdSe and several materials. ...29
Figure 3.2.2. Diagram of a Si/SiN chip with electrodes and nanocrystals on a SiN membrane. 30
Figure 3.3.1. Size histogram of 50 nanoparticles, each measured twice from TEM images. 31
Figure 3.4.1. Droplet drying after drop-casting on a device. 33
Figure 3.5.1. Cryostat in operation, with BNC breakout boxes and illumination window. 34
Figure 3.5.2. Diagram of electronics setup for current-voltage measurements. 35
Figure 3.5.3. Transmission electron micrographs of electrode pairs containing multilayer nanocrystal films. 36
Figure 3.6.1. A diagram of (a) primary and (b) secondary photocurrent. 37
Figure 3.6.2. Representative I-V dark current curves for a bare device, and a device with annealed nanocrystals. 38
Figure 3.6.3. I-V curve for one of the few devices with measurable dark current. 39
Figure 3.6.4. Plot of dark conductivity versus inverse temperature. 40
Figure 3.8.1. Nanocrystal spacing and energy levels (a) before and (b) after annealing,

adapted from Ref. [14] 42
Figure 4.2.1. (a) AFM topography, (b) AFM phase, and (c) TEM of the same nanorod cluster. 46
Figure 4.2.2. TEM, AFM, and integrated fluorescence for a nanorod cluster. 47
Figure 4.3.1. A diagram depicting the topography scan and the electrostatic force scan. 48
Figure 4.4.1. TEM of PbS nanocrystals. 50
Figure 4.4.2. EFM of bare electrodes, with the top electrodes at -6 V. 51
Figure 4.4.3. (a) AFM and (b) EFM for a two electrode device with PbS nanocrystals. .52
Figure 4.4.4. EFM phase data plotted versus film height. 53
Figure 4.5.1. TEM of Au nanocrystals. 55
Figure 4.5.2. (a) AFM, and EFM with (b) 2 V and (c) 4 V on the tip, for a drop-cast assembly of Au nanocrystals on SiN. 56
Figure 5.1.1. (a) Surface plasmon polaritons and (b) localized surface plasmon polaritons.[108] 59
Figure 5.2.1. Electric multipoles observed at a distance due to surface plasmon polaritons on a nanocrystal.[112] 61
Figure 5.3.1. Metal pillar arrays, (a) before and (b) after nanocrystal deposition. 63
Figure 5.3.2. Plasmon resonance shift versus interparticle gap, adapted from Ref. [118]. 64
Figure 5.4.1. I-V measurement with delay to account for hysteresis. 65
Figure 5.4.2. Normalized photocurrent plotted versus wavelength. Inset: Nanocrystal absorption. 66
Figure 6.1.1. (a) Schematic of the photodetector nanogap device. (b) TEM image of the electrodes prior to nanocrystal deposition. (c) Optical image of the device with 12 electrode pairs. (d) TEM images of several nanocrystals and a single nanocrystal. 70
Figure 6.1.2. Optical image of a device with annealed nanocrystals after measurement. 72
Figure 6.1.3. TEM of two nanogaps after measurement with nanocrystals annealed at 498K. 72
Figure 6.1.4. Device under illumination from a green laser. 74
Figure 6.1.5. I-V curves in the dark and under 532 nm illumination, for a device before and after nanocrystal deposition and laser or dark voltage treatments. 75

Figure 6.1.6. Photocurrent vs. voltage curves at various temperatures. 76
Figure 6.1.7. Photocurrent magnitudes for nanogap devices illuminated with 532 nm light. 77
Figure 6.2.1. Histogram of $R_{final}/R_{initial}$ on a logarithmic scale, including laser voltage treatments (green) and dark voltage treatments (blue). 79
Figure 6.2.2. Distribution of R values for nanogap devices. 80
Figure 6.2.3. Histogram of the ratio $R = I_{78K}/I_{295K}$ for two excitation wavelengths. 82
Figure 6.2.4. Photocurrent versus laser intensity (a) before and (b) after a dark voltage treatment. 83
Figure 6.3.1. Recombination and transport processes for charge carriers in a nanocrystal circuit. These processes are affected by the laser and dark voltage treatments. 85
Figure 6.4.1. Photocurrent versus illumination intensity at (a) 295K and (b) 77K. 87
Figure 6.5.1. Photocurrent vs. voltage curves for 650 nm, 532 nm, and 473 nm laser excitations. 90
Figure 6.5.2. Diagram showing photoexcitation of charge carriers from trap levels at various wavelengths of light. 91
Figure 6.6.1. $R_{final}/R_{initial}$ as a function of time for laser and dark voltage treatments. 93
Figure 6.7.1. Device illustration and exciton dynamics for observed photocurrent behavior. 96
Figure 7.1.1. Sample fluorescence image of nanocrystal film on graphene. 99
Figure 7.2.1. Absorption of nanocrystals on glass, and annealed nanocrystals on graphene. 101
Figure 7.3.1. Schematic of gold electrodes and graphene nanoribbon. 103
Figure 7.3.2. I-V curve for bare graphene nanoribbon. 104

1 Introduction

The work described here focuses on two of the grand challenges of optoelectronic nanocrystal based devices—reliability and efficiency. Experimental results are presented which characterize the optical and electronic properties of defects and coupled systems, discover new physics behind memory effects, and suggest how better understanding and control of defect structure and coupled electronic structures can be used to create robust nanocrystal based devices.

1.1 Semiconducting Nanocrystals

Semiconducting nanocrystals are recognized as revolutionary optoelectronic device components for applications as diverse as fluorescent tagging, light-emitting diodes, solar cells, and nanoelectronics. The size of nanocrystals, which is at the border between the quantum scale and the macro scale, gives them useful physical properties not seen in atoms or in bulk solids. Quantum confinement of carriers leads to delocalized charge carrier states whose energy depends on the nanocrystal size, thus the optical absorption and emission is tunable with nanocrystal size. For this reason, nanocrystals with sizes below the confinement limit are also called quantum dots. Difficult physics and engineering challenges, however, still remain in order to make the transition from nanocrystals in a research lab to nanocrystals in commercial devices. The most important factors for optoelectronic nanocrystal devices are reproducibility, reliability, and efficiency.

Reproducibility of nanocrystal size and composition has been solved previously by chemical synthesis. The challenges in reliability and efficiency spring from the underlying physics of confined carriers, conduction by tunneling, and defects in nanocrystals. In bulk semiconductor devices, defects are minimized by careful crystal growth and crystal edges that are a small fraction of the device volume. Nanocrystals, however, grow quickly, experience significant lattice strain, and have surface atoms that

are a sizable fraction of the device volume. And at small scales, discontinuities and defects can have a greater effect on device operation than they would in traditional bulk semiconductors. Both clever device engineering and a deep understanding of the physics will be necessary to optimize performance.

1.2 Optoelectronic Measurements

Many methods are available to study electrical behavior in nanocrystal devices. Drop-cast nanocrystal films can be placed between two electrodes, allowing voltage to be applied across the film. The induced current, which acts as a probe of conductivity, is then measured. The nanocrystal film can be illuminated with photons at a variety of wavelengths and intensities to produce photogenerated current. Structural information about the film, gathered using atomic force microscopy or transmission electron microscopy, can be correlated with electrostatic force microscopy data, which measures the spatially resolved conductivity of a film. Device design can also be taken beyond the two-electrode geometry. For example, metal pillars can be introduced to the nanogap, with plasmonic resonances that enhance the electric field experienced by the nanocrystal film. Graphene can be used as the substrate for the nanocrystals, to improve electrical conductivity between nanocrystals without sacrificing their optical properties. Each of these methods sheds light on part of the picture.

The connection between the assembly patterns of drop-cast nanocrystals and conduction in the resultant films can be probed using atomic and electrostatic force microscopy. Whereas diffusion dominates conduction in the bulk material, charge carriers travel from nanocrystal to nanocrystal by variable range hopping, which is a tunneling process. Films of semiconducting nanocrystals are non-uniform and insulating, meaning that charge does not propagate through the film easily. This is due to the many tunneling barriers present in a nanocrystal film, which yield a system of isolated conducting islands. For metal nanocrystals in low concentrations, drop-cast assembly yields diffusion-limited aggregates of nanocrystals, due to nanocrystal motion during solvent evaporation. The resulting fractal metal aggregates respond to nearby voltages by developing image charge, and their structure could be used to apply enhanced voltages to

semiconducting nanocrystals.

Applying a voltage across an electrode gap results in a uniform electric field in the gap. This field adds a directional component to the diffusion of charge, causing current to flow. Strong electric fields can also be excited by objects with plasmon resonances. For high carrier densities and sizes much smaller than the wavelength of incident light, the light can resonantly couple with the charge carriers. These driven oscillations are referred to as localized surface plasmon polaritons, and they can cause a strong electric field close to the nanoscale object. Placing an array of metal pillars in the active area of a nanogap device causes plasmonic enhancements of the electric field at certain wavelengths of light, determined by the pillar material, size, and spacing. For the lithographically defined gold pillars measured, the enhancement is small, though larger enhancements could be achieved for smaller plasmonic object spacing.

The insulating nature of nanocrystal films can also be bypassed by using another material for conduction. In a two-electrode device, graphene grown by chemical vapor deposition can be used as a substrate for nanocrystals. Nanocrystal luminescence is quenched by the graphene, indicating strong electrical coupling between the two materials. However, optical absorption measurements show that the characteristic nanocrystal absorption peaks are still present, indicating that the quantum confinement of nanocrystal energy states is maintained despite the coupling. Thus, graphene shows significant promise as a substrate for nanocrystal devices.

1.3 Extracting the Physics

Using two-electrode nanocrystal film devices, it is possible to conduct a detailed study of photoconductivity by applying light to the devices and measuring current. Many variables can be modified that affect photocurrent, including the wavelength and intensity of the light, and the temperature of the device. Although there are contradictions in the literature concerning the basic physics of photoconductivity in semiconducting nanocrystal arrays—specifically different observed temperature dependences for photoconductivity, with various explanations proposed—the work reported here demonstrates for the first time that there exists a reproducible relationship between

photoconductivity and temperature, once memory effects are taken into account. Specifically, it has been found that electric field induced population and optically induced depopulation of traps can reverse the temperature dependence of the photoconductivity. Photoconductivity of CdSe/ZnS nanocrystal arrays can be modified by cycling voltage under illumination or in the dark, and the effect exhibits saturation after a few hours. This provides a robust and reproducible procedure for controlling the trap population in nanocrystal nanogap devices.

The physical mechanism responsible is the manipulation of charge trap populations in nanocrystals, which are affected by applying light and electric fields. The trap occupancy modifies low-temperature photocurrent, changing the measured temperature dependence. With appropriate control of trap populations, a range of temperature-dependent behaviors previously attributed to material differences can in fact be reproduced in a single device. This provides a possible explanation for contradictory reports of the temperature dependence of photoconductivity in the literature. Dynamically controlling trap populations has the important benefit of achieving optimized photodetector sensitivity at low or high temperatures for light sources, photovoltaics, electronics, and other applications.

Interestingly, while sub-band gap illumination does not yield measurable photocurrents, it does affect the photoconductivity upon subsequent band gap illumination. Sub-band gap excitation is actually found to be more efficient for charge detrapping than excitations above the band gap. Different wavelengths of light excite trapped carriers into different band gap edge states, and charge carriers excited to higher states have a larger number of relaxation pathways available than those in the lowest conduction state. For example, they can relax into lower states, into trap states, or travel out of the nanocrystal via field-driven transport. It is possible that access to higher states could reduce the trap emptying efficiency, decreasing the memory effect. This conceptually supports the experimental result that sub-band gap energy photons are more efficient at trap manipulation in nanocrystal semiconducting films.

1.4 Scope of This Work

This thesis begins with an explanation of the chemical synthesis of cadmium-based semiconducting nanocrystals. The quantum confinement, energy levels, and optical properties of nanocrystals are discussed. Electronic properties of semiconducting nanocrystals are then explained, including electron and hole states in an individual nanocrystal, charge localization, film conduction, and photocurrent response. The experimental techniques used in this work are described in detail, such as substrate fabrication, lithography, dark and photocurrent measurements, and the effects of vacuum and temperature. Several microscopies are covered, including transmission electron microscopy, atomic force microscopy, and electrostatic force microscopy. Force microscope studies of both semiconducting and metal nanocrystals are discussed. Plasmonic devices, with integrated arrays of metal pillars whose plasmon resonance at a visible wavelength should enhance measured nanocrystal photocurrent, are reviewed and examined. The effects of charge traps on photocurrent temperature dependence and device memory are explored in detail, with time, wavelength, and intensity measurements corralled to support a trap population manipulation picture that allows tunable device properties. And finally, the coupling of nanocrystals with graphene is studied via optical and electronic measurements.

Together, these measurements paint a fascinating picture of semiconducting nanocrystals: their unusual basic physics, their difficult but interesting integration into photosensitive devices, and their unique place in the modern nanoscientist's toolbox.

2 Nanocrystals: Scientific Background

Summary

A nanocrystal is an object possessing a crystal lattice structure and an effective radius of less than about 50 nm. Spherical semiconducting nanocrystals, sometimes called quantum dots, have a growing number of optoelectronic applications as photodetectors,[1-5] solar cells,[6] and light emitters.[7] They have a high yield of excitons from photons, also called quantum yield, a bandgap that is widely tunable and covers the visible spectrum, and well-established synthesis protocols.[8-10] Nanocrystals with a core made of one material and a shell made of another are particularly interesting, because of their improved quantum yield, protection against oxidation, and confinement. In this work, "nanocrystals" refers to spherically symmetric nanocrystals, and in one chapter "nanorods" refers to nanocrystals with aspect ratios above 1:1.

Nanocrystals, which contain a few thousand to a few hundred thousand atoms, have properties that are intermediate between simple quantum properties and classical bulk properties. Their optical properties deviate from bulk properties: they have intense, narrow emission peaks that are useful for fluorescence tagging and spectroscopy, and can absorb photons to generate excitons that can be separated and collected as current.[11] The energy bandgap of nanocrystals is inversely proportional to their radius and can be tuned to many energies, including the entire visible spectrum. This is useful for the potential fabrication of optoelectronic devices such as solar cells, where a range of nanocrystal sizes could allow cells to fully utilize the solar spectrum. Light-sensitive artificial solids based on nanocrystal arrays are also useful as flexible model systems for the study of basic transport phenomena.[1, 12-14] However, nanocrystals possess unique challenges because of their size. They fluoresce intermittently[15] and their photocurrent can be diminished by the tunneling barriers between nanocrystals and by the presence of traps,

defects which spatially localize charge carriers.[9, 16] Control over the effects of traps would be a large step forward in the development of efficient nanocrystal solid devices.

Nanocrystals inhabit a particularly interesting region of the size spectrum for condensed matter physics. They exhibit significantly different behavior from individual atoms or their building blocks, but they do not possess the properties of bulk materials either. With hundreds of atoms, rather than one atom or a trillion atoms, nanocrystals bridge the quantum and macroscale worlds. To study the scientific properties of nanocrystals it cannot be assumed that they will behave as other systems do.

2.1 Synthesis and Characterization

Nanocrystals intended for use in ensembles in an optoelectronic device should ideally possess the following traits:

1. Nearly monodisperse in size.
2. Uniform in shape.
3. Uniform in chemical composition.
4. Crystalline with few defects in the lattice structure.
5. Nonreactive (passivated) due to a well-controlled surface chemistry.

Each of these properties affects the electrical and optical functionality of the nanocrystals, which will be discussed in more detail later in this chapter. Nanocrystals can be created by gas condensation, arc discharge, ion sputtering, and laser ablation, but chemical synthesis is the most convenient and inexpensive method of fabricating semiconducting nanocrystals which meet the criteria listed above.[11]

The nanocrystals used in this work are created commercially using a synthesis procedure based on the La Mer model for producing monodisperse colloids[17] that has been applied to cadmium nanocrystal growth.[10]

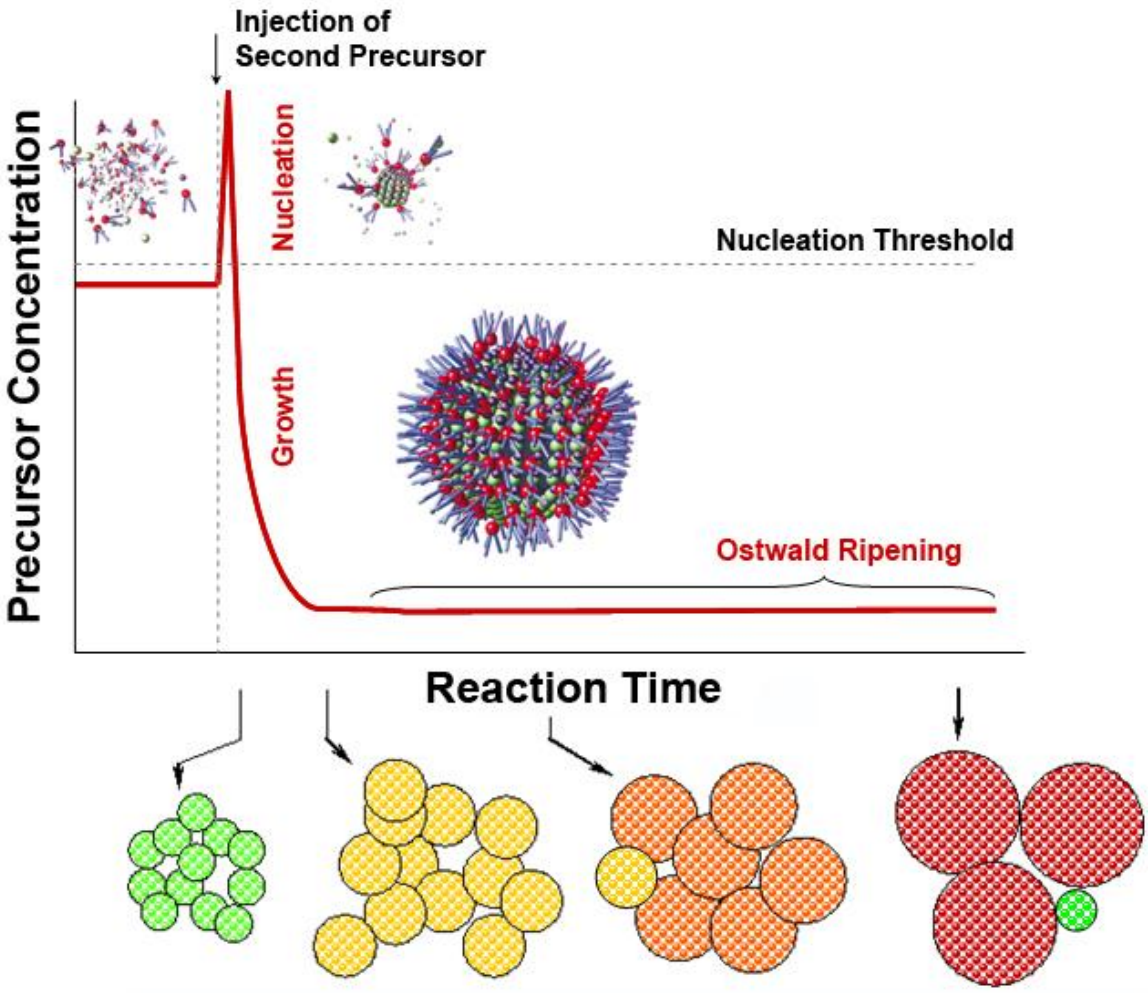

Figure 2.1.1. Synthesis diagram, showing nucleation, growth, and Ostwald ripening.

Nanocrystal synthesis can be divided into several stages, as shown in **Figure 2.1.1**: nucleation, growth, and ripening. La Mer showed that a narrow distribution of nanocrystal sizes can be obtained by minimizing the nucleation time and maximizing growth time.[17] This result is achieved by rapidly adding reagents to a reaction vessel to raise the precursor concentration above the nucleation threshold, at which point nucleation will occur to relieve the supersaturation.[18] To create CdSe nanocrystals capped with tri-*n*-octylphosphine oxide (TOPO), trioctylphosphine selenide and dimethyl cadmium precursors are injected into a heated coordinating solvent.[10] At high temperatures the coordinating ligand, TOPO, is frequently exchanged, which promotes

crystal formation. Many crystals nucleate simultaneously, but the nucleation occurs during a very short time. Once the supersaturation of the precursors is relieved by a short burst of nucleation, then the solution enters a growth phase, where the seeds continue to grow at a controlled rate as long as the solution is heated at a stable temperature. The brevity of the nucleation phase ensures that all the nucleation sites will be a similar size upon entering the growth phase, thus the nanocrystals will retain a focused size distribution as the existing nuclei grow with a uniform rate.[17] Although the formation of many small crystals is kinetically favored at the nucleation stage, after growth large crystals are favored thermodynamically due to their lower surface energy.[19] Thus, once the crystals reach a certain size, the smallest nanocrystals will dissolve due to their high surface energy and their material will be deposited on the larger nanocrystals, a process called Ostwald ripening.[20-22] Ostwald ripening broadens the size distribution of the nanocrystals, and a focused size distribution of small nanocrystals can be achieved by stopping the reaction before Ostwald ripening begins.[23] When the heat source is removed, the crystal growth effectively comes to a halt because the coordinating ligands act as a passivating cap, preventing the aggregation of nanocrystals and reducing their chemical reactivity.[10] The ligand can be replaced with a different capping ligand, by precipitation and redispersion in a concentrated solution of the new ligand,[23, 24] or can be completely removed via UV annealing or thermal annealing.[12, 25]

In this synthesis, the TOPO (or other coordinating solvent) plays several crucial roles. The ligand forms a coordination complex with one of the two precursors, selenium in the case of CdSe synthesis, a requirement because of the electronic properties of selenium. During the synthesis, the TOPO desorption rate, which is dependent on temperature, directly controls the rate of nanocrystal growth. To stop the reaction, the temperature is lowered, and once the TOPO desorption rate is low enough, the TOPO now acts as a passivating ligand, preventing surface degradation and precipitation. Ligands control growth rate and reaction mechanism, as well as particle shape and size distribution.[26] For device integration, the ligand's long length and electrical insulation act as barriers to conduction and performance, but in the synthesis the action of the ligand is integral.

The process described above, where nucleation begins when the precursor concentration is just above the nucleation threshold, results in nanocrystals which grow slowly and evenly in all directions. The nanocrystals are faceted due to the crystal lattice but approximately spherical. Other shapes can be created by adjusting the growth rate, which can favor certain crystal faces so that rods, stars, tetrapods, and other shapes form.[23]

For homogeneous nanocrystals, the addition of a shell consisting of several monolayers of a different but related material can improve the carrier confinement and the optical response of the nanocrystals. This is due to the importance of surface states and hence, surface quality in nanocrystals. The bonding and coordination of the surface atoms affects both the mechanical properties of the nanocrystal, by modulating the strain, and the electronic properties of the nanocrystal.[27] Adding a shell can also reduce the dielectric contrast between the nanocrystal and its surroundings.[28] For these reasons, core-shell nanocrystals are widely used in device studies, either as thin few-monolayer shells, thick shells, or multiple shells. Depositing the shell can be done using the same procedure described above for nanocrystal synthesis, at a lower temperature to prevent nucleation. However, the shell material must be chosen to have a similar surface energy and bandgap, must have a similar crystal lattice structure so that defects due to surface strain are minimized, must not nucleate or diffuse into the core, and must be deposited under conditions which do not destroy the core material. When the shell has a larger bandgap than the core, the carriers in the core experience stronger quantum confinement than carriers in core nanocrystals with no shell. Such core-shell nanocrystals are said to have Type I band alignment. If the shell has a smaller bandgap, one or both carriers may delocalize to the shell, which is called Type II band alignment.[29] For CdSe cores, ZnS is widely used as a shell material because it has a well-matched crystal lattice as well as Type I alignment.[9]

Once synthesized, nanocrystals can be examined to determine their structural characteristics. Transmission electron microscopy (TEM), where objects are imaged by an electron beam on a very thin substrate that is approximately transparent to electrons, is a powerful tool for characterization. TEM images can have much higher resolution than

optical microscopy, because the de Broglie wavelength of electrons which limits the resolution is very small compared to that of light.[30] In TEM images, objects which scatter electrons appear dark, and objects which allow electrons to pass through appear light. Thus metal electrodes look very dark in TEM, and semiconducting nanocrystals look less dark but are still visible against either amorphous carbon or silicon nitride substrates. The crystal lattice planes of a nanocrystal are often visible in high quality TEM images. Recently efforts have been made to observe nanocrystal synthesis itself in TEM, with either vapor phase or solution growth.[31, 32] But for synthesis performed outside the TEM, imaging the resultant nanocrystals in TEM allows one to verify their shape and size dispersity.

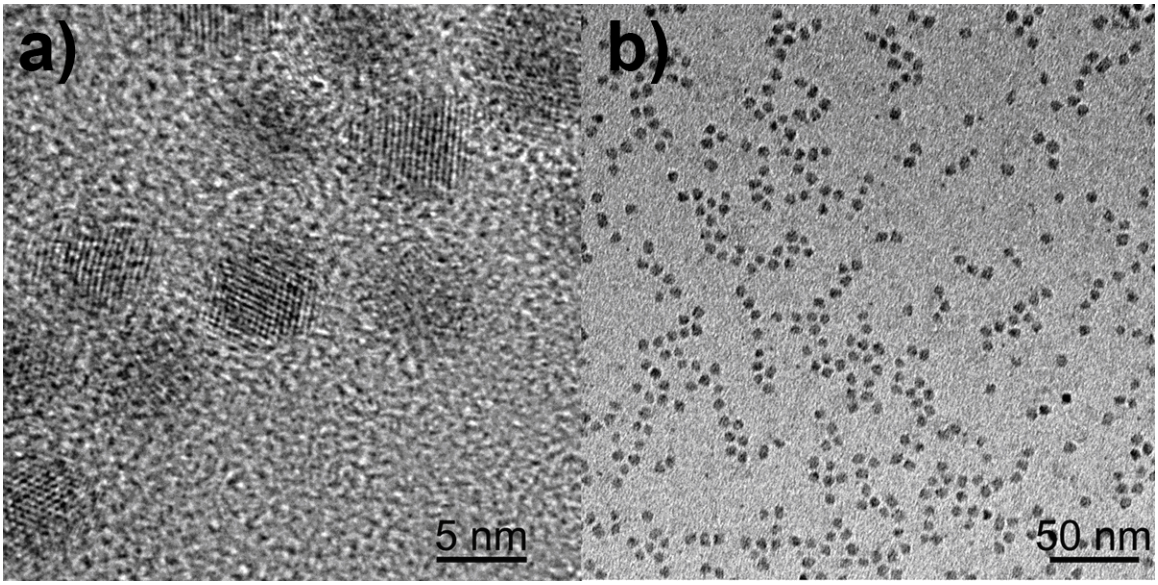

Figure 2.1.2. High-resolution TEM images of CdSe/ZnS nanocrystals on a carbon grid.

The nanocrystals used in much of this work were CdSe/ZnS core-shell spherical nanocrystals purchased from Sigma Aldrich, but fully characterized in the lab. The nanocrystals were capped with a mixture of hexadecylamine and trioctylphosphine ligands to prevent aggregation and passivate surface traps. TEMs of the nanocrystals are shown in **Figure 2.1.2**, with the crystal lattice planes clearly visible against the amorphous carbon substrate in the **Figure 2.1.2**a. CdSe nanocrystals have a wurtzite

crystal structure, as shown in **Figure 2.1.3**. The wurtzite lattice can be described as two interleaved hexagonal close-packed lattices, one for the Cd atoms and one for the Se atoms. Wurtzite is the name for the lattice as observed in binary compounds, but the same lattice with only one atom type is the diamond lattice, where each atom is tetrahedrally coordinated.[33]

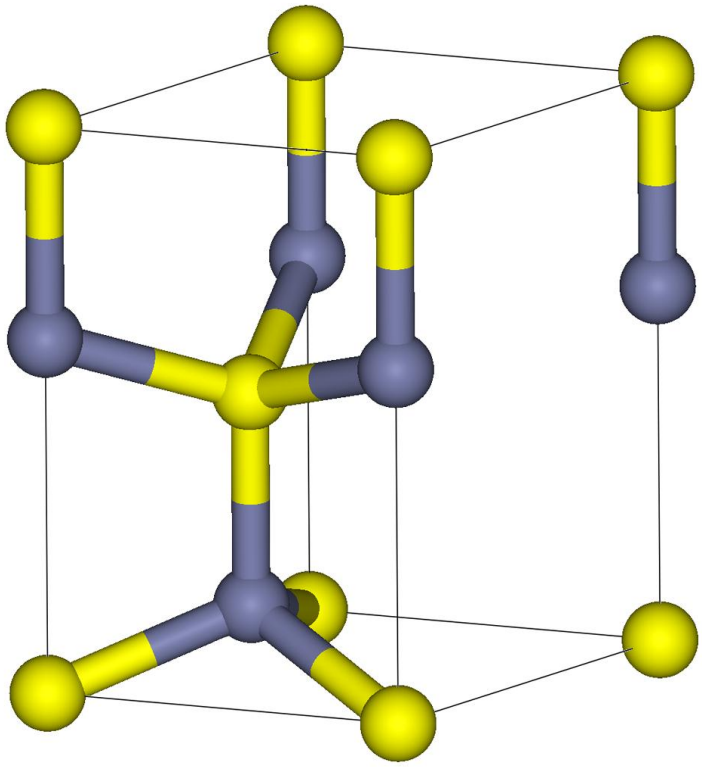

Figure 2.1.3. Wurtzite crystal structure.

2.2 Quantum Properties

Many of the interesting properties of nanocrystals stem from their quantum nature. Although bulk materials have bands of available electronic states, nanocrystals have quantized states due to the confinement introduced by their small diameter, which is

why they are sometimes called “artificial atoms” and “quantum dots”. Semiconducting nanocrystals still possess a band gap, as would the same material in bulk, but the states in the valence and conduction bands are quantized beyond what states are available in the bulk. This state quantization occurs as a result of the spatial restrictions on the charge carriers (electrons and holes) in the material. Whether a nanocrystal’s carriers experience quantum confinement or not can be determined by examining carrier behavior in the nanocrystal: namely, one can calculate the Bohr radius for a bound electron-hole pair, an exciton, within the nanocrystal material by using the Bohr formula and substituting the hole for the atomic nucleus:[34, 35]

$$a_B = \varepsilon \frac{m}{m_c} a_0 \tag{2-1}$$

The exciton Bohr radius, a_B, is given in the equation above in terms of ε, the dielectric constant of the material, m, the electron rest mass, m_c, the reduced exciton mass, and a_o, the Bohr radius of hydrogen. When the nanocrystal radius is significantly smaller than the exciton Bohr radius in that material, then carriers in the nanocrystal will experience quantum confinement and a reduced density of energy levels.[36] For CdSe, the exciton Bohr radius is between 2.4 and 2.9 nm,[15, 37] and experimentally nanocrystals with radii below approximately 3 nm begin to exhibit size-dependent optical properties.[38]

The simplest model for understanding the electronic structure of a nanocrystal is the quantum mechanical particle in a box. For a spherical nanocrystal, charge carriers within the nanocrystal are confined by the nanocrystal radius, which can alternately be written as the mathematical boundary condition

$$V = \begin{cases} 0 & r < R \\ \infty & r \geq R \end{cases}. \tag{2-2}$$

Thus the box described is a nanocrystal with radius R. The solution wavefunctions for such a particle, using spherical coordinates, are given by

$$\Psi_{n,l,m}(r,\theta,\phi) = \frac{C}{r} j_l(k_{n,l} r) Y_l^m(\theta,\phi), \tag{2-3}$$

where C is a normalization constant, $j_l(k_{n,l} r)$ are the l^{th}-order spherical Bessel

functions, and $Y_l^m(\theta,\phi)$ are the spherical harmonic functions. Enforcing the boundary conditions above yields $j_l(k_{n,l}R)=0$, which means that $k_{n,l}R=\lambda_{n,l}$ where $\lambda_{n,l}$ is the *n*th zero of j_l. The eigenenergies of carriers in the nanocrystal can now be written as

$$E_{n,l}=\frac{\hbar^2 k_{n,l}^2}{2m_c}=\frac{\hbar^2\lambda_{n,l}^2}{2m_c R^2}. \tag{2-4}$$

The energy dependence on R is the key to why nanocrystal energy levels change with the nanocrystal's size, leading to the dependence of absorption and emission spectra on particle radius.

The above analysis was applicable for spherical nanocrystals that are confined in all directions. Nanorods and nanowires have one axis along which they do not experience quantum confinement. Along that axis carrier transport can be thought of as a scattering process obeying the Landauer-Büttiker formalism, which relates the transmission fraction of incident carriers to conductance for a material with electrical leads.[39, 40]

The next sections will review several of the properties due to quantum confinement that make nanocrystals an interesting material to study. The optical absorption and emission of nanocrystals depend on their size. The electronic states of nanocrystals can be approximated by adding excitonic corrections to the quantum mechanical particle in a box. Carriers can be localized by lattice defects, and the resultant charge traps also affect the electronic properties of nanocrystals. When many nanocrystals are incorporated together into a self-assembled thin film, the film retains many of the optical properties of individual nanocrystals but its electronic transport, both in the dark and under illumination, is determined by the ease with which carriers can move between nanocrystals and the electrical quality of the contact to the electrode.

2.3 Optical Properties

When a nanocrystal is excited by a photon, the resultant exciton is delocalized over the nanocrystal, and the available excitonic states are determined by the confinement, which is to say, by the nanocrystal size and material.[18] For this reason, the optical properties of nanocrystals, such as the absorption and emission at different

wavelengths, are size dependent, as shown in **Figure 2.3.1**. Smaller nanocrystals have different electronic states, which change the energies of transition between states due to the quantum confinement of the electron in all spatial dimensions.

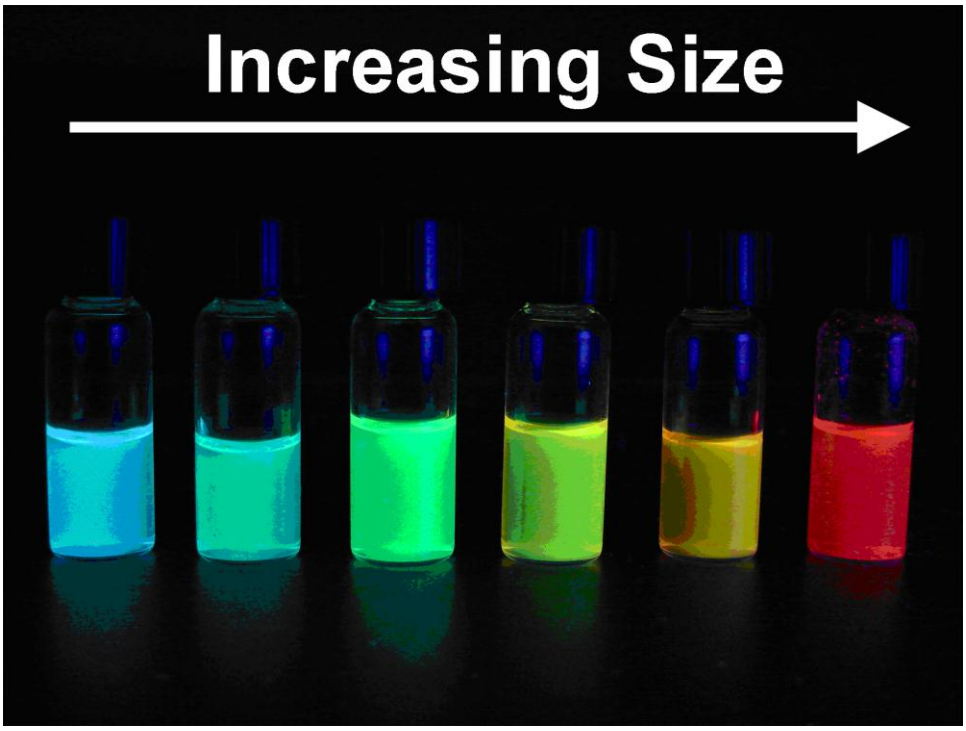

Figure 2.3.1. Fluorescent emission of nanocrystals of various sizes.

For nanocrystals below the quantum confinement threshold, discrete electronic states are available because the allowed momenta, or k-values, of the states have also been quantized. If the nanocrystal diameter is decreased, the separation between nanocrystal states increases, widening the bandgap in semiconducting nanocrystals and blueshifting the absorption and emission peak wavelengths. This corresponds to the energy dependence on $1/R^2$ shown in Equation 2-4. The bluest emission in **Figure 2.3.1** comes from the smallest CdSe nanocrystals pictured, on the left of the image.

The absorption and emission spectra for nanocrystals yield information about the electronic structure of the nanocrystals. The absorption spectra, which describe the wavelengths at which nanocrystals absorb incident photons and the extinction at those

wavelengths, are superpositions of several absorption peaks at energies corresponding to excited state transitions. The primary absorption peak corresponds to the band gap energy. The absorption spectra can be used to identify energy transitions[41] as well as to determine nanocrystal quality and investigate electronic coupling with substrates. Emission occurs when an absorbed photon creates an exciton which then radiatively recombines, emitting a new photon. The emission spectra for semiconducting nanocrystals have a Lorentzian profile that is slightly redshifted from the wavelength corresponding to the bandgap energy. The redshift of the emission peak relative to the first absorption peak is due to the Stokes shift, where some absorbed energy is dissipated in the nanocrystal as phonons. The width of the distribution depends on the size dispersity of the nanocrystals, with a larger size distribution leading to a broader emission peak.

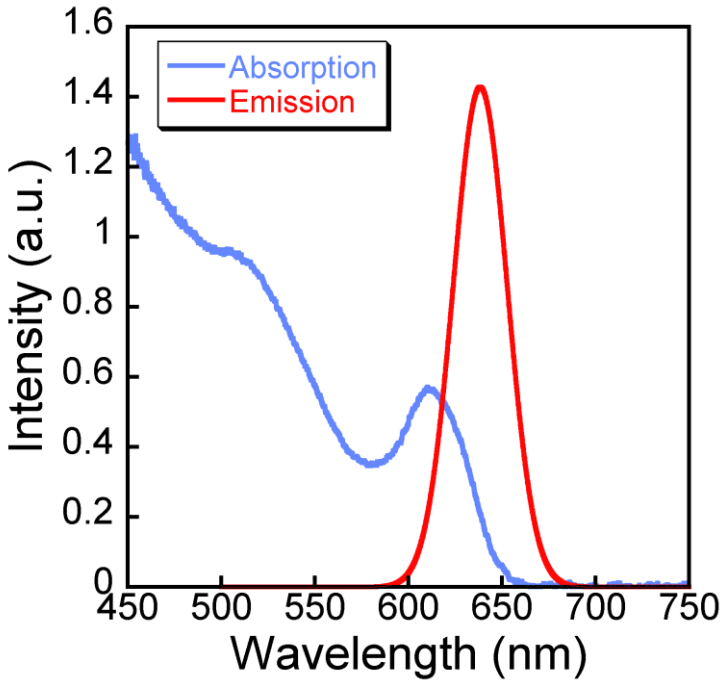

Figure 2.3.2. Absorption and emission intensity vs. wavelength for nanocrystals studied.

The absorption and emission spectra of CdSe/ZnS nanocrystals from Sigma-Aldrich in toluene solution were recorded using SpectraSuite from Ocean Optics (**Figure 2.3.2**). Emission data were gathered with the sample illuminated by an Ocean Optics LS-

450 with a 470 nm LED and filter. The light source for the absorption spectrum was an Ocean Optics LS-1 with a tungsten halogen bulb. The primary excitonic absorption peak was at 610 nm and the emission peak was at 638 nm. The reported quantum yield from Sigma-Aldrich is 30%.

The CdSe core size for a given absorption peak can be estimated using the empirical formula fitted by Yu et al.[42]:

$$D = (1.6122\times10^{-9})\lambda^4 - (2.6575\times10^{-6})\lambda^3 + (1.6242\times10^{-3})\lambda^2 - (0.4277)\lambda + (41.57) \quad (2\text{-}5)$$

Here D is the nanocrystal diameter in nm, and λ is the wavelength in nm of the first absorption peak. Adding a ZnS shell broadens and redshifts the absorption peak, with the magnitude of the redshift depending on the size of the nanocrystal.[8] This is due to the delocalization of the electron but not the hole into the shell; thus the largest proportion of the redshift comes from the first shell monolayer.[43]

Under continuous illumination, nanocrystals, like many other molecular and nanoscale systems, fluoresce intermittently. This fluorescence intermittency, also called "blinking," is observed in many molecules, fluorescent green protein, single light harvesting complexes, and single organic fluorophores in addition to nanocrystals.[44] The mechanism behind blinking is not well understood, although the most commonly accepted theory is that electrically neutral particles are in the off state, and charged particles are in the on or fluorescing state.[15, 45] Blinking can be observed in both individual nanocrystals and small ensembles of nanocrystals.[46-48] In semiconductor quantum dots, rods, and wires, the distributions of fluorescence on- and off-times of individual particles follow truncated power law (Levy) statistics.[44] Non-blinking nanocrystals have been fabricated by having a continuous transition from core to shell material, [49] by the addition of dopants,[50] and after treating nanocrystal films with thiols.[51] An analogous electrical switching has been observed in single CdSe nanorods.[52] Blinking and current switching are not observed in the device measurements in this thesis: blinking is not measured because optical output of electrical devices was not measured, and electrical switching is most likely not observed due to the ensemble averaging when many nanocrystals are measured together in a film.

2.4 Electronic Properties

Electronic measurements of nanocrystals are needed to complement the energy state information gleaned from optical measurements. Progress in this area has been slow due to the many experimental difficulties encountered; for instance, it is quite difficult to electrically contact a single nanocrystal lithographically, the nanocrystal is very sensitive to its electrical environment, and there can be a large variation between different nanocrystals.[53] Many successful single nanocrystal measurements have been done using scanning tunneling microscopy (STM), where the STM tip acts as one of the two electrodes contacting the nanocrystal.[54-56] Instead of examining a single crystal, it is possible to look at an ensemble of nanocrystals in a thin film, which has the advantages of ease of fabrication and averaging over slight nanocrystal differences. The case of a nanocrystal film will be discussed in more detail in the following section, but first the electronic states in a single nanocrystal are estimated using qualitative models.

As shown in Equation 2-4, the most important factor controlling the environment of a charge carrier in a nanocrystal is the nanocrystal size. The energy levels for a charge carrier in a nanocrystal are given in Equation 2-4, but to obtain electrical solutions that are of use in discussing photocurrent, terms for the exciton binding energy, E_{ex}, and the Coulomb interaction between the photogenerated electron and hole in small enough nanocrystals must be added. If the radius of the nanocrystal is much larger than the exciton Bohr radius, $R >> a_B$, then the carriers are weakly confined and the final exciton ground state energy will be

$$\hbar\omega = E_G - E_{ex} + \frac{\hbar^2\pi^2}{2(m_e + m_h)R^2}. \qquad (2\text{-}6)$$

This energy depends on the band gap energy E_G for a semiconducting nanocrystal, as well as the exciton binding energy and a term for the quantum size. For smaller nanocrystals, the quantization of states and the Coulomb interaction become more important. If the radius of the nanocrystal is much smaller than the exciton Bohr radius, $R << a_B$, then the carriers are strongly confined and the exciton ground state energy will be given by

$$\hbar\omega_{\nu} = E_G + E_{\nu}^{h}(R) + E_{\nu}^{e}(R) - 1.8\frac{e^2}{\kappa R}. \qquad (2\text{-}7)$$

The exciton binding energy has been replaced by the electron and hole energies in the quantized states whose energies match the incident photon energy, and the final term is a Coulombic correction whose value is calculated using first-order perturbation theory.[35] As the nanocrystal size decreases, the contribution from the Coulombic term will become less important, because of its $1/R$ dependence as opposed to the $1/R^2$ dependence of the other terms. The resultant parabolic energy bands are simplifications of most real world semiconductor band structures. The parabolic approximation is good for the bottom of the band in cubic and wurtzite semiconductors such as CdSe, but the degeneracy and spin-orbit splitting of the bands in this material mean that Equation 2-7 is useful for qualitative, not quantitative, description of the electronic structure. Quantitatively, the structure can be described in detail using the multiband effective mass approximation.[35]

2.5 Charge Localization and Trapping

To apply the particle-in-a-box solution to charge carriers in nanocrystals, it was assumed above that the carriers were delocalized over the entire nanocrystal, which is a reasonable assumption for a perfect lattice. However, as in the bulk, within a nanocrystal it is possible to have a lattice site defect that disrupts the lattice period, creating localized electrostatic fields. This defect can be due to a lattice vacancy, a different species of atom (i.e. a dopant), or an interstitial atom. The resultant electrostatic field can spatially localize a carrier to the defect site. Defects where the carrier has a high probability of excitation to a delocalized state using thermal energy are called traps, whereas defects where the carrier is likely to recombine with a carrier that has opposite charge before thermal freeing can occur are sometimes called recombination centers.[16] In both cases, the carrier is localized and trapped. The energy levels for traps are unfavorable for charge transport to another nanocrystal or an electrode, so trapping usually lowers measured dark and photocurrent. For simplicity, all localization centers will be referred to as traps, with the understanding that whether recombination or thermal excitation dominates will

depend on the nanocrystal properties and environmental conditions.

Bulk defects are possible within the nanocrystal core, but more numerous are surface defects resulting from the discontinuity of the nanocrystal lattice at the surface. Atoms at the surface of nanocrystals have a lower coordination number and higher valence electron density than those in the interior.[57] The high proportion of surface atoms compared to bulk atoms, and the many dangling bonds at the surface, make surface traps more likely than bulk traps for nanocrystals. A shell on the nanocrystal can passivate some surface traps, but the shell itself will also have surface traps. Chemical ligands passivate surface traps as well, though they act as a barrier to conduction which may not be desirable for devices.

For a given charge trap, its energy level will depend on the specific nature and location of the defect causing the trap. In a semiconductor, a trap with an energy level slightly above the valence band will act as a hole trap, and a trap with an energy level slightly below the conduction band will act as an electron trap. The energy difference between the trap and the nearest regular energy level can be determined by thermally or optically stimulating the trap, by either raising the temperature of the material or applying illumination, and measuring at what energy carriers move from the trap into the conduction band.[16] The steady state trap population will be determined by the thermal and illumination environment of the material, and if the trap population is enhanced or depleted, the rate at which the population will return to equilibrium depends on the kinetics of charge carriers in the material. Past measurements of the photocurrent during and after a brief pulse of illumination revealed a long decay time, because a large number of trapped carriers makes the photocurrent decay time longer than the free carrier lifetime.[58] Trapping can affect the optical spectra, but if non-trap processes dominate, then the peaks due to trapping may be very small compared to those due to the band edge and other transitions. In samples with a large number of traps, the trapping and detrapping of charges has been measured as a 1/f noise at low measurement frequencies.[59] The 1/f character of the noise is due to the distribution of trap energies. The presence of charge traps can change the dark conductivity, photosensitivity, speed of response, and spectral response of a material,[16] which makes traps crucial factors in a

variety of applications.

The manipulation of trap states, on the surface or in the bulk, has been explored in recent years. Surface states are the focus of efforts to develop single nanocrystal-molecule complexes capable of computation, where information processing would occur via the surface interactions.[60] Changing surface interactions by applying potentials or absorbing molecules can perturb electronic structures reversibly, which is promising for the idea of a 'computer on a particle.'[60] Surface and bulk defects which localize charge have been found to affect piezoelectric response.[61] Photoinduced surface trapping can lead to overly high quantum yields, which have erroneously been attributed to carrier multiplication in nanocrystals in solution.[62] Nanocrystals which have been doped by the addition of bulk defects have been observed to magnetize by exposure to light.[63] Charge localization also affects the reliability of nanocrystal memory devices.[64] Since charge-localizing traps, especially surface traps, seem difficult or impossible to remove from nanoscale devices, learning how to control and use trapping behavior seems necessary from an application perspective. From a physics perspective, the ubiquity and significance of charge traps is unique to nanoscale systems, and adds another layer of complexity to the simple particle-in-a-box model.

2.6 Conduction in Nanocrystal Solids

Films comprised of nanocrystals are especially interesting, both for their rich physics and their potential device applications. Nanocrystals can self-assemble into either ordered or glassy arrays, and useful films to study can be multilayer, monolayer, or submonolayer (with a defined layer edge). These so-called artificial solids are tunable both via nanocrystal properties and via inter-nanocrystal coupling, creating a many-body physics system which is straightforward to manipulate.[65] Nanocrystal films have similar optical properties to those of nanocrystals in suspension, although the optical path through a thin film will include far fewer absorbers and emitters than the path through a concentrated solution of nanocrystals. But the electronic properties of nanocrystal films are a level of complexity above those of individual nanocrystals because of both the weak

coupling between nanocrystals and the presence of a tunneling barrier presented by the physical distance between nanocrystals and the insulating organic ligand between the nanocrystals. Rather than the infinite potential well dealt with previously, there is now a finite potential barrier between nanocrystals which can be tunneled through. Weak coupling can pose measurement problems because of the poor conduction through arrays of nanocrystals, but stronger coupling would affect the quantum confinement and thus compromise the interesting optical properties of the nanocrystals. This is one reason why the usage of synthesis protocols with metallic surface ligands, such as hydrazine-stabilized metal chalcogenide complexes, is unlikely to displace the use of long hydrocarbon chain ligands which preserve nanocrystal confinement.[66] Short ligands, such as hydrazine, pyridine, or ethylenediamine, can improve conduction without sacrificing confinement in some cases.[67]

In general, nanocrystal films can be modeled as arrays of conducting islands, where bound charge carriers can move between islands by tunneling through an insulating barrier. Conduction in these films is a percolation process. This model implies that current, *I*, will have a power law dependence on voltage, *V*, given by[68]

$$I \sim W\left(\frac{V_0}{R}\right)\left[\frac{V}{V_T}-1\right]^{\lambda}. \qquad (2\text{-}8)$$

Here W is the array width and R is the tunneling resistance. Below the threshold voltage, V_T, further current is suppressed by the Coulomb energy of adding a charge carrier to the conducting island. V_0 is given by $V_0 = \frac{e}{C_0}$ where C_0 is the self-capacitance of an island.[68] The exponent in the power law depends on the film cross-section and dimensionality. Above V_T, charge carriers begin to be able to traverse the array via percolation paths that connect islands in a one-dimensional chain. As voltage continues to rise, more paths become available. While temperature is not taken into account in the simple model above, finite thermal energy lowers tunneling barriers in the array, effectively reducing V_T. In a study of metal nanocrystals, the dependence of V_T on temperature was found to be approximately[69]

$$V_T(T) = V_T(0)\left(1 - \frac{P(T)}{P(T^*)}\right), \tag{2-9}$$

where $P(T) \sim 2\beta k_B T/\alpha$ is the fraction of nanocrystal-nanocrystal contacts that can be considered Ohmic because the barrier energy is comparable to $k_B T$; here, α is a charging energy which incorporates disorder, and β is a measure of thermal broadening of energy levels. T^* is the temperature at which a complete Ohmic path exists between the electrodes by following the Ohmic contacts.[69]

Although this model takes temperature activation into account, and accurately describes some ensembles of metal nanocrystals, the variability in the nanocrystal-nanocrystal contacts, and thus the variability in the potential barriers encountered by the charge carriers as they attempt to percolate through the material, has been omitted. This factor was first considered in a theory of conduction through a disordered solid by Mott, who realized that both spatial separation between conducting islands and energy separation, i.e. non-overlapping energy levels, will affect the success rate for charge carrier hopping.[70, 71] While simple thermal activation predicts that most carriers hop to their nearest neighbor, when differences in energy levels are taken into account, it becomes preferable for some carriers to tunnel long distances from their initial island if the destination island is energetically very similar to the initial island. This can come into play in nanocrystal solids if some of the nanocrystals are charged by pre-existing unbound carriers, though very long-range hopping is less likely because thermal energy disrupts the wavefunctions. This model, called variable-range hopping, yields an expression for the probability, *P*, for hopping a distance, *D*,

$$\ln(P) \sim -\left(\frac{2D}{L} + \frac{E_a}{k_B T}\right), \tag{2-10}$$

where L is the localization length or conduction island size and E_a is the characteristic activation energy for hopping. The dependence of E_a on hopping distance is chosen based on the system, and conductivity can be derived from the probability expression above to follow

$$\ln(G) \sim T^{-\nu}, \tag{2-11}$$

where ν depends on the dimensionality, 1/3 for two-dimensional systems and 1/4 for three-dimensional systems. Without variable-range hopping, $\nu = 1$, which is also called Arrhenius behavior. This model can be experimentally confirmed by measuring conduction as a function of temperature to extract the exponent.[72]

A final correction to the variable-range hopping model was proposed by Efros and Shklovskii, who discovered that the Coulomb interaction between confined carriers opens a gap in the density of states, which would lead to $\nu = \frac{1}{2}$.[73] For conductance through CdSe nanocrystals, at low temperatures Mott conduction is observed and at high temperatures Efros-Shklovskii variable range hopping is observed.[72] The transition occurs when the thermal energy approaches the width of the Coulomb gap in the density of states, mathematically when

$$k_B T \sim \frac{e^2}{4\pi\varepsilon r}.^{74} \tag{2-12}$$

2.7 Photocurrent in Nanocrystal Solids

The above discussion has focused on conduction in general through nanocrystal solids, regardless of whether the charge carriers are injected from electrodes into the film or photogenerated within the nanocrystals. While charge carriers moving through the nanocrystal film experience the same physics regardless of how they were generated, the main difference between these two cases comes from the carrier generation itself. Carriers injected from the electrodes are propagating through the film with other carriers of the same type, and the case without photoexcitation is called “dark current”. For photocurrent, when the film is illuminated, the carriers are introduced to the system as photogenerated excitons. This means that two carriers of opposite types are initially sharing the same nanocrystal, so geminate recombination is possible because the carriers cannot diffuse away from each other without tunneling to a new nanocrystal. Without an externally applied electric field, very little photocurrent is measured because diffusion dominates the carrier motion and most carriers recombine. Photocurrent carrier dynamics

thus depend on exciton generation rate, exciton separation efficiency, competition between electron and hole mobilities, and the rates of non-radiative and radiative recombination. These specific dependencies will be discussion in more detail in Chapter 6. Very few of these factors affect injected dark current, because of the external electric field and the pre-existing separation of carriers.

The optimization of the photocurrent response of nanocrystal films is a difficult problem that can be approached from several different angles. There are mechanical approaches, such as modifying the interparticle spacing or ordering the nanocrystal solid, and there are electronic approaches, such as doping the nanocrystals, using a metallic ligand, eliminating or deactivating charge traps. Within the same nanocrystal film, two species of nanocrystals with different doping and properties can be activated by different wavelengths of light, creating a photoelectrochemical photocurrent switch.[60]

Photocurrent in nanocrystal solids has been observed to depend non-linearly on the applied electric field. A model of tunneling field-ionized carriers reproduces the non-linearity, although with unrealistic physical parameters.[75]

This thesis is largely concerned with exploring these techniques for modifying transport behavior, such as the manipulation of defects to affect conductance, as well as creating a model of photoconductivity temperature dependence that reliably predicts measurement results. These ideas suggest paths forward for devices, and elucidate the nature of this interesting nanoscale material.

3 Experimental Techniques

Summary

The experimental work described in the following pages relies on several fabrication and measurement techniques. The most commonly used device for this work is a two-electrode gap on a thin silicon nitride membrane. The current-voltage (I-V) response is measured for a device without nanocrystals, also called a bare device, and remeasured after nanocrystal deposition. Finally, the nanocrystals are thermally annealed, after which photocurrent measurements begin. Creating a device for the experiments described herein has several steps: fabrication of the silicon nitride membranes, electrode fabrication using optical and electron beam lithography, deposition of nanocrystals, and thermal annealing. These devices are imaged with TEM before nanocrystal deposition, and then not imaged until again after deposition once all photocurrent measurements are complete, because TEM can modify photocurrent behavior. Detailed descriptions of these experimental techniques follow.

3.1 Membrane Fabrication

Creating devices at the nanoscale is challenging, because of the difficulties inherent in fabrication and lithography and also because of the highly variable nature of many nanoscale experimental devices. The active area of these devices is created using electron beam lithography, where a polymer resist such as poly(methyl methacrylate) is deposited by spinning onto a surface. Exposure to the electron beam crosslinks the polymer, changing its solubility, and this can be used to define a pattern with the electron beam. The sample is then developed so that the regions exposed to the beam are no longer covered by polymer. If devices are patterned on chips where the active area of the device sits over a 40 nm thick silicon nitride membrane, the thin membrane allows for

very high resolution electron beam lithography, because the electron backscattering scales with membrane thickness.[76] The membrane also serves as a substrate for high-resolution structural characterization using TEM. This structural characterization serves multiple purposes: it allows the lithography of the fabricated electrodes on the device to be checked before nanocrystal deposition, helps determine the thickness and homogeneity of the nanocrystal layer, and pinpoints the cause of most device issues that may have arisen during measurement. A schematic of the SiN membrane with electrodes is shown on the left in **Figure 3.1.1**.

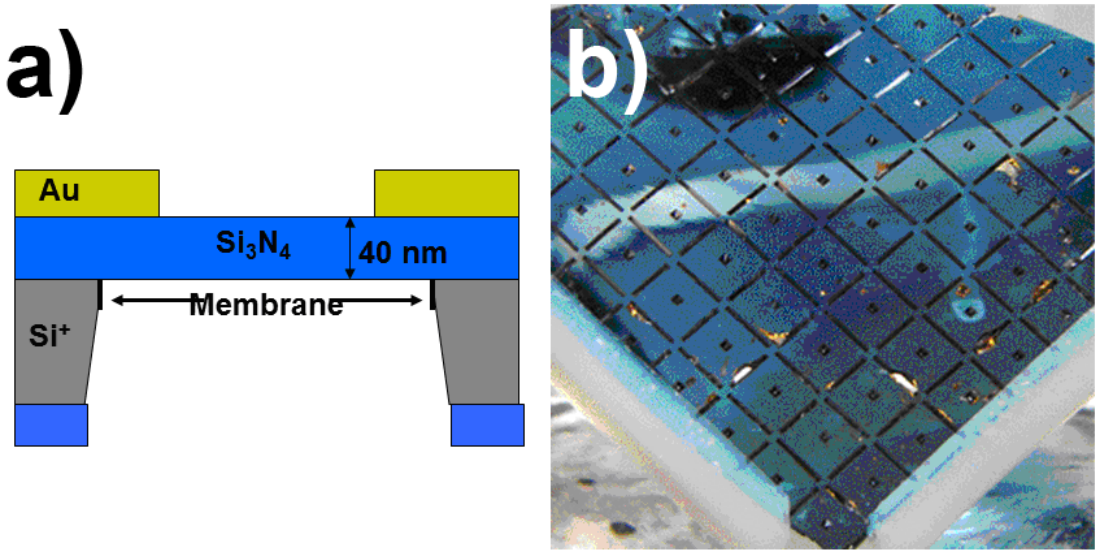

Figure 3.1.1. (a) A schematic of a single SiN membrane and (b) a photograph of a wafer with many etch-defined chips and membranes.

Silicon nitride membranes are fabricated from 500 µm thick <100> p-type silicon (Si^+) wafers that have 100 nm of highly polished, low-stress amorphous silicon nitride (Si_3N_4) on both sides. These wafers were processed to produce many ~5 × 5 mm^2 chips, each with a 50 × 50 μm^2 region in its center where the Si_3N_4 membrane is freely suspended. [76] The membranes are created using optical lithography, which is similar to electron beam lithography in that a polymer resist is used, but in optical lithography the entire chip or wafer can be exposed simultaneously to UV light that modifies the resist, as

opposed to the serial process of exposing resist with an electron beam. Optical lithography also uses a metal mask to define features in parallel, whereas in electron beam lithography the beam follows a pattern input to computer control by the user. The wafers are first coated on one side with a protective resist and on the other side with NR7 photoresist spun on at 3000 RPM for 42 seconds, and then baked at 115ºC for 3 minutes. The masked wafer is exposed to 365 nm light at 5 mW/cm^2 for 34 seconds and baked at 115ºC for 2 minutes. The wafer is placed in RD6 for 16 seconds, a resist developer that dissolves the exposed resist polymer, followed by a rinse with deionized water. To remove the silicon nitride from the patterned side, the wafer is then exposed to a SF_6 plasma etch in a Technics PeII-A Etcher at 50 W with a pressure under pumping of 400 mTorr for 120 seconds. The unexposed resist can be removed using acetone. To etch the underlying silicon, the wafer is exposed to a 1.5 M potassium hydroxide (KOH) wet etch at 130ºC. The KOH etches anisotropically through the silicon, along the <111> face, until the silicon nitride on the protected side of the wafer is exposed, which takes approximately 18 hours. Once the etching is complete, the membrane of 100 nm thick silicon nitride is further thinned to approximately 40 nm using another SF_6 plasma etch step. A wafer with all the etch steps completed, with many individual chips defined each of which has its own thin membrane, is shown in **Figure 3.1.1** on the right.

3.2 Electrode Fabrication

Electrode properties are critical to device properties. The contact resistance to the electrode varies randomly between nanocrystals, due to differences in orientation and packing density. But by choosing the electrode material carefully and ensuring that the lithography is flawless, reliable electrical contacts between the electrode and nanocrystal film can be made.

The selection of gold as the electrode material is based on the work function of the metal relative to the nanocrystal conduction and valence band energy levels.[77] The band gap for a nanocrystal, E_G^{nano}, can be written in terms of the band gap for the same material in bulk, E_G, by adding excitonic and confinement corrections.[78, 79] The nanocrystal bandgap for CdSe compared to several material work functions are shown in

Figure 3.2.1.

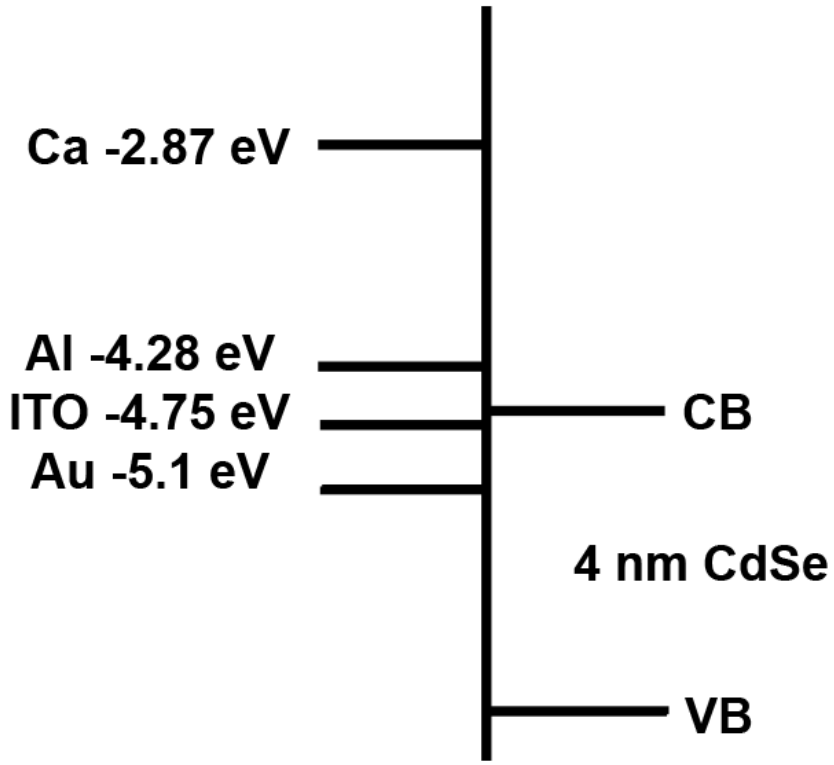

Figure 3.2.1. Energy levels and work functions for 4 nm CdSe and several materials.

Using a low work function material, such as calcium which has a work function of -2.9 eV, would result in carrier injection from the electrodes into the nanocrystals. For devices whose aim is to measure photocurrent, it is preferable to have no electrode injection. The work function of gold, -5.1 eV, is more suitable.

Nanoelectrodes were patterned onto the membrane by electron beam lithography on an Elionix 7500-ELS. Afterward 3 nm of nickel and 30 nm of gold were evaporated onto the devices. Nickel was chosen as an adhesive layer for the small features because it leaves almost no debris in nanoscale gaps. Connecting wires and contact pads were added using optical lithography, with a glass and metal wafer mask in a Karl Suss MA4 Mask Aligner. After the pattern is written, thermal evaporation of 3 nm of Cr and 100 nm of Au defines the wires and contact pads.

Chips were allowed to outgas overnight after lithography steps to avoid TEM contamination. Inspection with high-resolution TEM ensured no visible metal debris was present in the gap vicinity that could short the electrodes, which is especially important for narrow gaps (~ 30 nm). Gap sizes of 20-230 nm were used, as measured with a JEOL 2010F field-emission TEM. Standard chip lithography includes twelve nanogaps patterned per chip. **Figure 3.2.2** shows a schematic diagram of the SiN/Si chip with a pair of Au electrodes on the SiN window[76] and CdSe/ZnS nanocrystals dispersed on the surface.

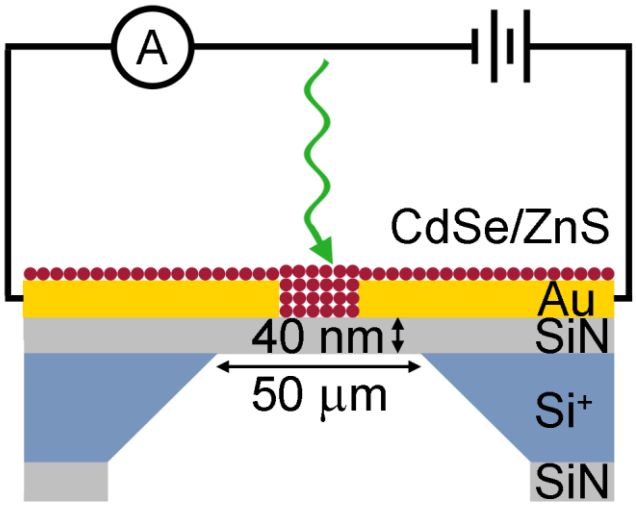

Figure 3.2.2. Diagram of a Si/SiN chip with electrodes and nanocrystals on a SiN membrane.

3.3 Nanocrystal Size Measurement

Nanocrystal size was determined to be 5.2 ± 0.6 nm, as the average of 50 nanocrystals in different drop-cast locations from high-resolution TEM images (**Figure 3.3.1**). Each nanocrystal was measured twice, with the measurements of the same nanocrystal roughly perpendicular to each other. These 100 measurements were averaged, giving a mean value of 5.2 nm with a standard deviation of 0.6 nm. This relatively large

variation is typical for commercial samples, and if necessary, a size-selection method can be used. For device purposes this size distribution was narrow enough. There may be a slight underestimation due to the increased difficulty in discerning the ZnS shell against the carbon grid background.

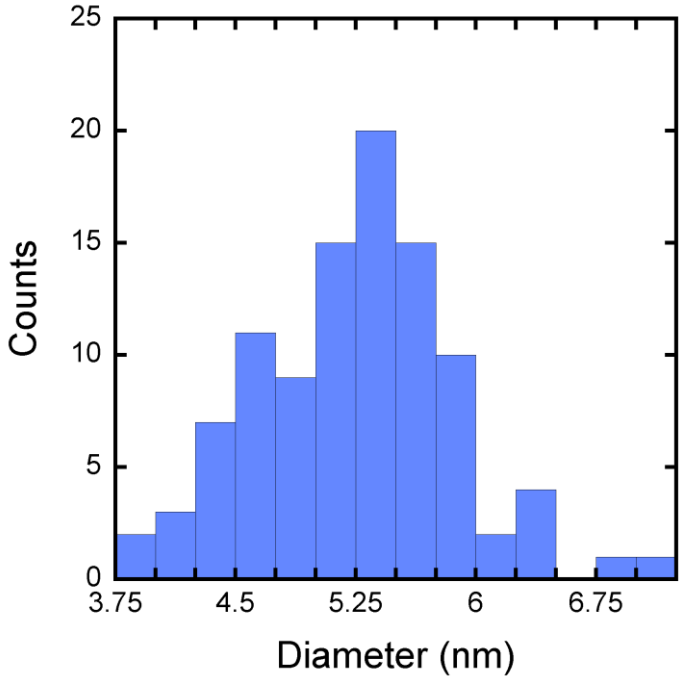

Figure 3.3.1. Size histogram of 50 nanoparticles, each measured twice from TEM images.

Based on observed size, the estimated redshift is ~5 nm, so that the absorption peak for these CdSe cores should be at a wavelength 605 nm. Conversely, the measured absorption peak can be used to calculate that the core diameter of the CdSe nanocrystals used is ~4.81 nm. It should be noted that without taking into account the redshift caused by the shell, the core size would be overestimated by ~0.25 nm. Knowing that the core diameter is 4.8 nm and the actual nanocrystal diameter, determined by TEM, is 5.2 nm, the shell must be ~0.2 nm, which is approximately one monolayer.

3.4 Device Integration

Integrating chemically synthesized nanocrystals into electrode structures can be done with a variety of methods, the most common of which are listed below:

1. Drop-casting: A precise amount of nanocrystal suspension can be ejected from a syringe onto a chip and allowed to dry in air. For a few microliter drop, drying takes less than five minutes. This process is very simple, but for substrates that do not pin the droplet at the edges the film thickness can be uneven. [80-82]
2. Spincasting: The chip can be installed on a spinner, which is operated at low speed during drop-casting. This process works best if the substrate surface is chemically functionalized to encourage the nanocrystals to adhere to the surface. Deposited layers of nanocrystals are very homogeneous but also very thin, and significant amounts of nanocrystal solution are wasted. [6, 83]
3. Spray coating: A commercial paint sprayer can be supplied with nanocrystal suspension and nitrogen to spray a thin and homogeneous coat of nanocrystals onto a substrate with minimal waste.[84]
4. Two-solvent deposition: Two solvents that are insoluble with each other can be used to create a solvent interface where nanocrystals will self-assemble into a monolayer. For nanocrystals dispersed in hexane or toluene, a droplet of acetonitrile can be placed in a Teflon container. When a drop of nanocrystal suspension is placed on the side of the droplet, the nanocrystal solution will sweep laterally across the droplet surface causing a monolayer of nanocrystals to assemble at the interface. The monolayer can then be stamped or scooped onto a substrate.[85]

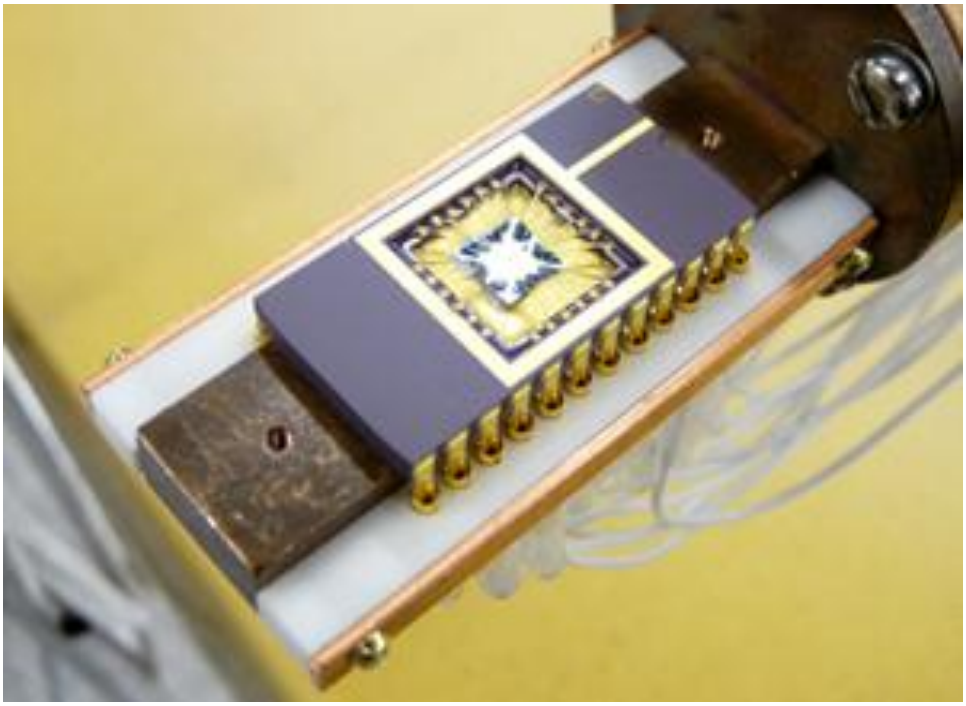

Figure 3.4.1. Droplet drying after drop-casting on a device.

Most commonly, drop-casting was used to deposit nanocrystals on these devices. This is due to both the simplicity of the procedure, and its compatibility with a device that is wired and mounted on a cryostat coldfinger. Drop-casting onto a pre-wired device minimizes the time that the nanocrystals will be exposed to air, because once the droplet is dry the cryostat can be closed and pumped down. In general, nanocrystals are added to devices after electrode fabrication because the reverse procedure, to deposit nanocrystals and then evaporate electrodes, would expose the nanocrystals to hot metal atoms that may interpenetrate the nanocrystal film and dope the nanocrystals. Drop-casting was not ideal for absorption samples, where the substrate was larger and non-uniformity was an issue. For thin-film absorption samples, the other three techniques were used, of which two-solvent deposition was the most reliable.

3.5 Two-electrode Measurements

Electrical measurements were performed in either a modified Janis VPF-700 or

ST-100H cryostat operated at ~5×10^{-7} Torr, at a temperature range of 6-575K. Photocurrent is generated by focusing laser light at a wavelength range of 472-980 nm through the optical windows onto the sample. One of the cryostats used is shown in **Figure 3.5.1**.

Figure 3.5.1. Cryostat in operation, with BNC breakout boxes and illumination window.

Each nanogap on the chip was wire bonded to a ceramic chip carrier. The chip

carrier pins are fitted into a Macor socket, pressing the chip carrier flush against a copper cold finger and heating stage to achieve thermal coupling. The socket pins are electrically addressed by silver-soldered wires compatible with high temperature operation which couple the source and drain pins to two independent BNC breakout boxes. Voltages were applied with a Yokogawa 7651 programmable DC source; current signals were amplified and filtered by a Keithley 428 current amplifier and measured with an Agilent 34401A digital multimeter. Custom LabView software was used to automate and control the experiment. This is schematically shown in **Figure 3.5.2**.

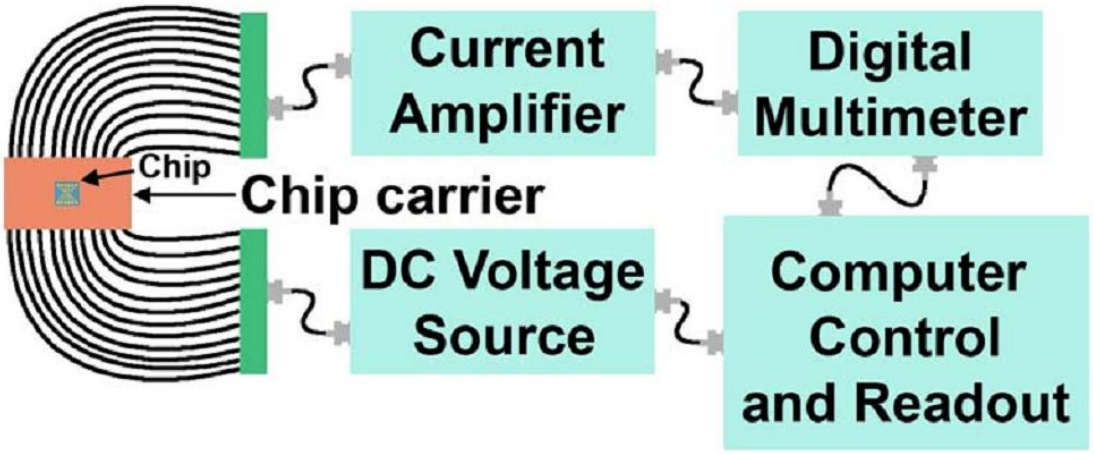

Figure 3.5.2. Diagram of electronics setup for current-voltage measurements.

I-V characteristics for each device were measured by sweeping the voltage across the nanogap from 0V to 2V to -2V and back to 0V, with a typical cycle taking 200 seconds. After TEM inspection the devices were first cleaned with O_2 plasma and then underwent measurements of their conductance and photoresponse. These serve as background measurements of the device without the presence of nanocrystals. These background measurements allow us to select devices with negligible leakage current before drop-casting nanocrystals.

Transmission electron micrographs of annealed multilayer nanocrystal films in two electrode devices with gap widths of ~ 27 nm (**Figure 3.5.3**a) and ~ 230 nm (**Figure**

3.5.3b) reveal the overall nanocrystal coverage, and show that nanocrystals self-assemble into disordered close-packed arrays.

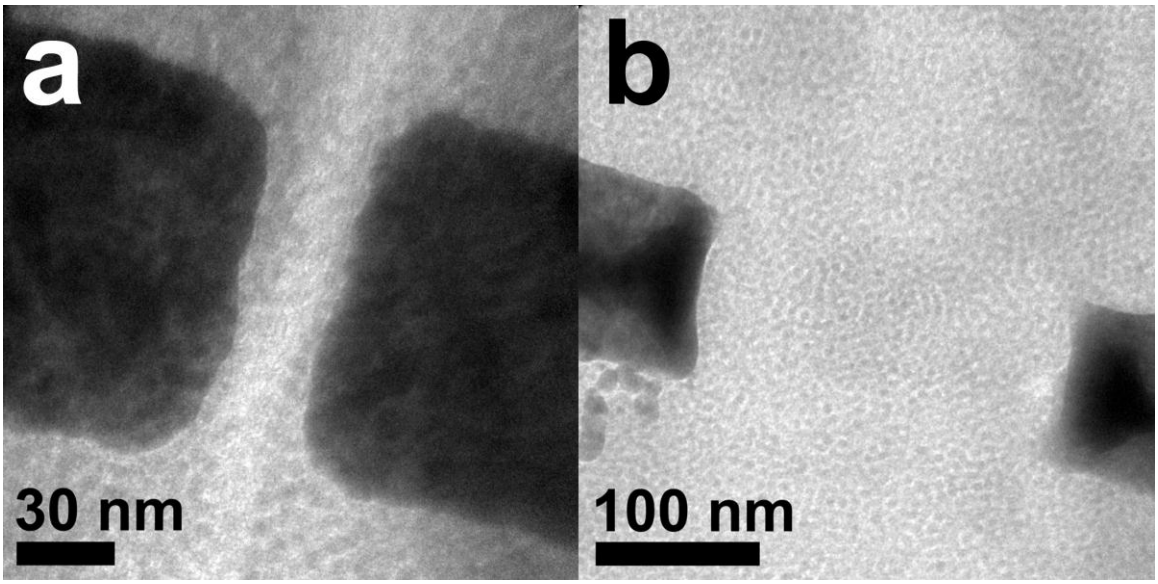

Figure 3.5.3. Transmission electron micrographs of electrode pairs containing multilayer nanocrystal films.

TEM imaging was performed after the dc current-voltage (I-V) transport measurements, and was used to check that gaps had not visibly degraded or blown up during the electrical measurements. No correlation was observed between the electrical characteristics and minor variations in nanocrystal ordering.

3.6 Dark Current Measurements

In order to understand the results from photocurrent measurements, the devices must first be studied for dark current, which is the conductivity without illumination. If a device has no dark current but does exhibit current under illumination, then the measured photocurrent must be entirely due to exciton generation from the absorbed light, and the photocurrent is said to be "primary". If the device does have dark current, and a larger quantity of current is measured under illumination, then some of the photocurrent is due to exciton generation and some is due to charge injection from the electrodes, and the

photocurrent is said to be "secondary".[86] With primary photocurrent, the nanocrystal remains electrically neutral, as equal and opposite charges are generated and swept away by electric fields. Secondary photocurrent effectively charges the nanocrystals, as the electrodes donate carriers. Devices that have no dark current but do exhibit photocurrent are called primary photodetectors. But, for devices where dark current may exist below the detection threshold, there is no intrinsic difference between primary and secondary photodetectors. Whether a photodetector is labeled "primary" or "secondary" is determined by the noise floor of the measurement setup.

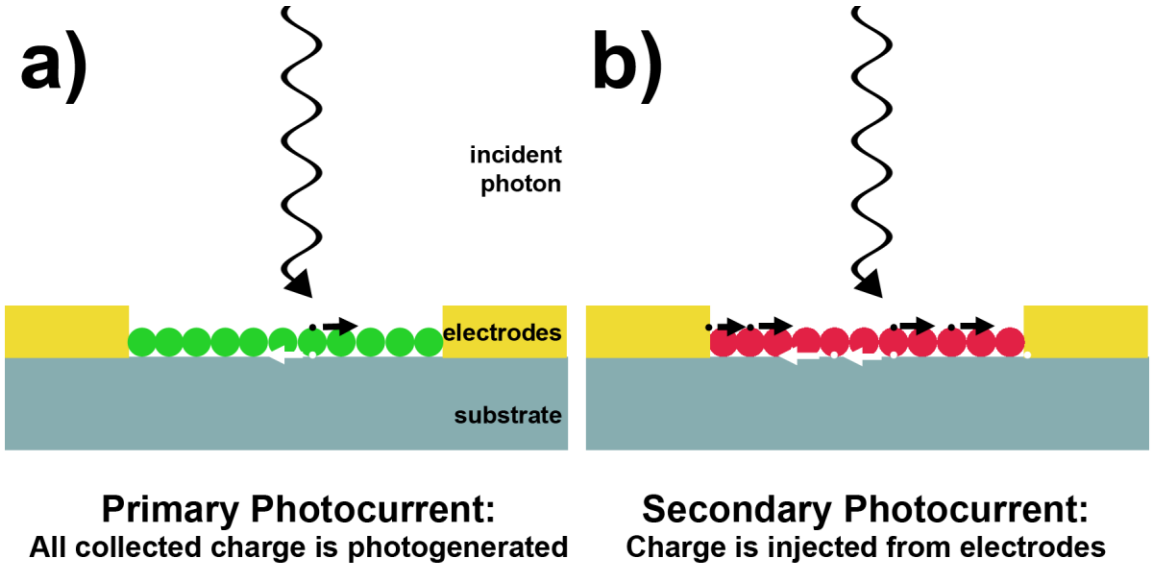

Figure 3.6.1. A diagram of (a) primary and (b) secondary photocurrent.

Dark current was measured on all nanogaps prior to any nanocrystal deposition, prior to any photocurrent measurements, and over the course of several months as devices were thermally cycled many times. Dark current was below the noise floor of the setup for 80% of devices measured. **Figure 3.6.2** shows examples of I-V characteristics for a bare nanogap measured at room temperature and for nanogaps with nanocrystals that have been annealed at 573K and measured at 78K and 295K.

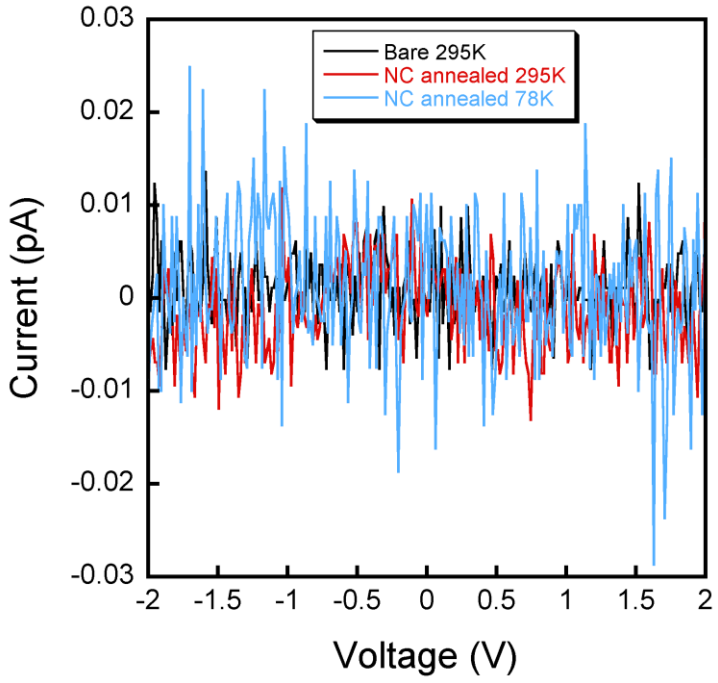

Figure 3.6.2. Representative I-V dark current curves for a bare device, and a device with annealed nanocrystals.

Less than ~20% of nanocrystal devices showed a very small dark current (~0.16 pA at 2V), 2-3 orders of magnitude smaller than the corresponding photocurrent. The devices with dark current were annealed at 573K, but not all devices annealed at 573K had dark current. Dark current most likely existed in these devices due to especially good electronic contacts between the nanocrystals and the electrodes. Dark current increases exponentially with voltage and can be empirically fitted to the exponential form

$$I_{dark} = \frac{V_o}{R_o} e^{\frac{V}{V_o}}. \qquad (3\text{-}1)$$

Here $R_o \sim 2 \times 10^{14}\ \Omega$ and $V_o = 0.7$ V are the characteristic resistance and voltage extracted from the plot in **Figure 3.6.3**, which represent the activation scale. This is in agreement with previously reported dark current measurements on micron-scale nanocrystal arrays.[12]

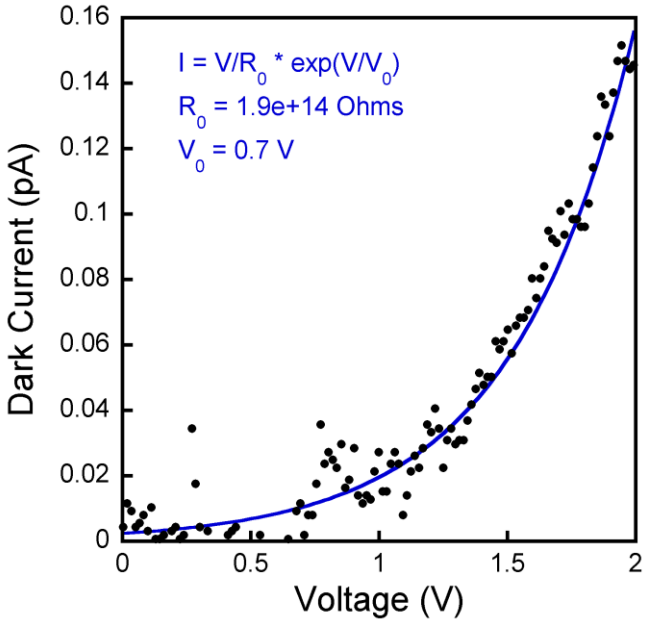

Figure 3.6.3. I-V curve for one of the few devices with measurable dark current.

Figure 3.6.4 shows the temperature dependence of the dark current, plotted as the zero-bias conductance *G* vs. *1/T*. The linear behavior shown is also called Arrhenius behavior, and an activation energy can be extracted from a line fit. This plot is representative for the few devices that exhibited measurable dark current.

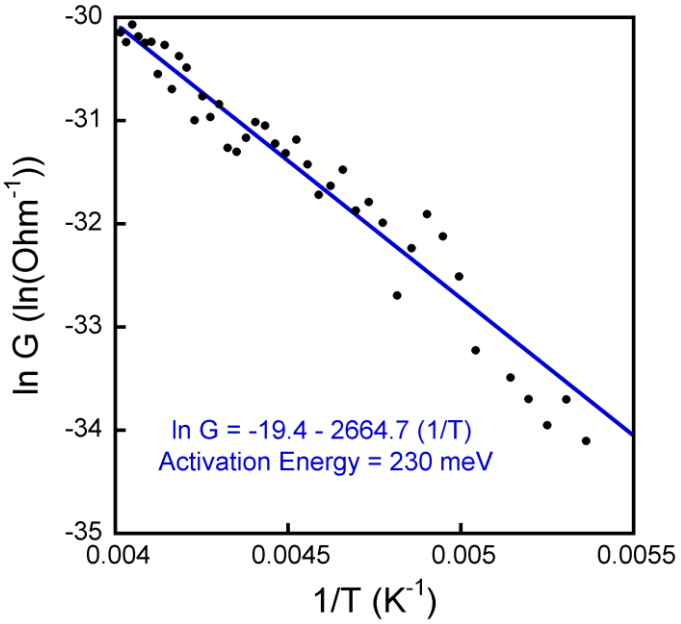

Figure 3.6.4. Plot of dark conductivity versus inverse temperature.

The dark current is thermally activated, with conductance scaling as

$$G \sim e^{-\frac{E_A}{k_B T}} \tag{3-2}$$

for an activation energy E_A. A range of activation energies has been measured from ~70-230 meV, consistent with previously published results.[1]

3.7 Vacuum and Temperature Considerations

Oxidation can destroy the optoelectronic behavior of many nanocrystals, including the cadmium-based nanocrystals used in this work. The photochemical instability of these nanocrystals arises because of photocatalytic oxidation of the ligands and photooxidation of the nanocrystal material.[87] As oxygen adsorbs to the nanocrystal surface and ligands, charge traps are created. As these traps build up, more carriers combine via trap-assisted nonradiative recombination. Photo-assisted oxygen diffusion into the core reduces the confinement radius of the exciton wavefunction inside the CdSe nanocrystal, which also affects properties such as the photoluminescence peak

wavelength.[88] In order to maintain the unoxidized state and high photocurrent over a long series of measurements, the nanocrystals are exposed to air only for a few minutes immediately after deposition, then the nanocrystal device is placed in a cryostat and all subsequent measurements and treatments are performed under a vacuum of approximately 5×10^{-7} Torr. It is widely accepted in the literature that a few minutes exposure to air is equivalent to performing the entire deposition procedure in a glovebox, and what oxidation occurs is not enough to modify photoconductivity. [14, 82] The device is only removed from vacuum at the end of all measurements.

TEM imaging can also damage the nanocrystals, because the high energy electron beam creates defects and charge traps. For this reason, TEM is carried out only before nanocrystal deposition, to inspect the electrodes, and after all electronic measurements are complete, to inspect the nanocrystal film. Electronic measurements themselves have not been observed to change the film structure except in extreme cases where the electrodes themselves explode due to heating and incidentally break up or fuse the film. Such devices are not included in the following results.

3.8 Annealing and Improving Conduction

Most of the nanocrystal deposition methods listed in Section 3.4 create glassy, disordered films. In addition, the nanocrystal ligands, which prevent aggregation of the nanocrystals in solution, create charge transfer barriers when the nanocrystals are deposited on a surface. Many methods to improve the conductivity of nanocrystal films have been explored, including ligand exchange where the synthesis ligand is exchanged with a smaller ligand, and chemical treatment of films with hydrazine.[67, 89] In both cases, bringing the nanocrystals closer together seems to improve the film conductivity, although the chemical treatments used can dope the nanocrystals or provide their own conducting network which may compromise the usability of the nanocrystals for optoelectronic applications. Another approach to improving film conductivity is thermal annealing, where the nanocrystal film is heated to a temperature well below the melting point of the nanocrystal material.[12, 90] Annealing has been shown to increase photocurrent in nanocrystal solids[12-14, 80] as the ligands desorb and the film contracts, which reduces

interparticle separation and lowers tunneling barriers. This is shown schematically for spacing and energy levels in **Figure 3.8.1**.

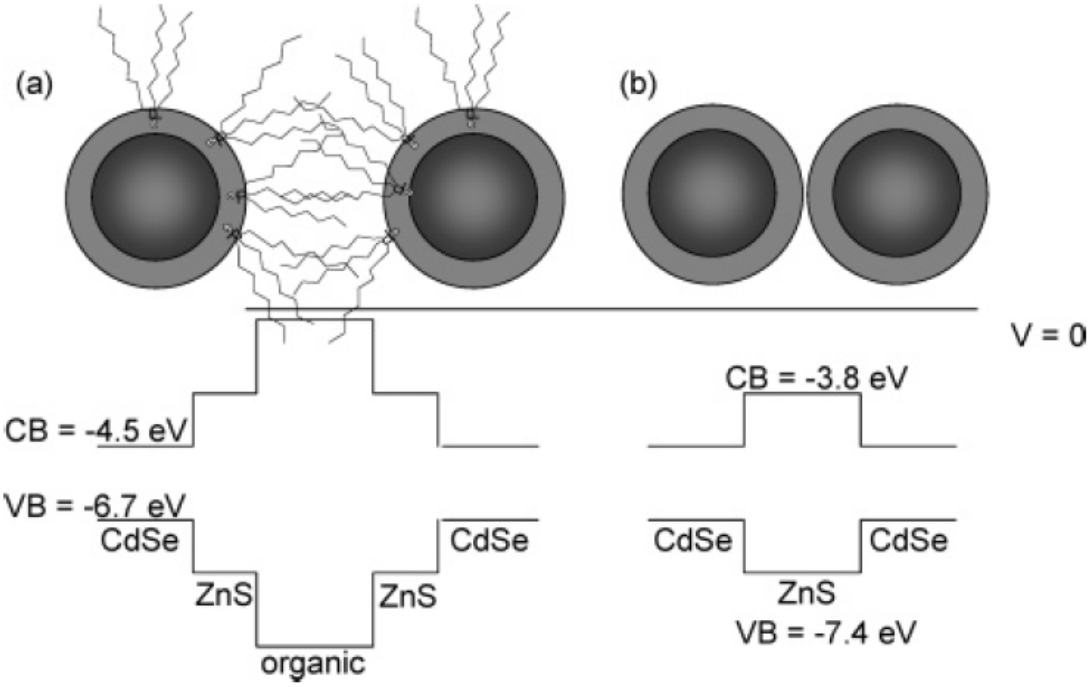

Figure 3.8.1. Nanocrystal spacing and energy levels (a) before and (b) after annealing, adapted from Ref. [14].

For successive annealing experiments on a total of twenty CdSe/ZnS nanocrystal devices, measurable photocurrent increased with annealing temperature T_a. Annealing was performed at a pressure of 10^{-6} torr, using a Lakeshore temperature controller to increase the temperature of the heating stage in a Janis cryostat. The annealing temperature was held constant for several hours and then allowed to slowly go down to room temperature after the heating stage was turned off. For T_a = 423K the percentage of devices exhibiting photocurrent was 44%, for T_a = 498K the percentage was 66%, and for T_a = 573K all devices showed photocurrent response. In devices that had photocurrent above the noise floor (0.03 pA at 295K and 0.15 pA at 78K), increasing the annealing temperature from 423K to 498K increased the observed photocurrent by 20 times on average. Above 498K, there was no measurable change in photocurrent magnitude or

response characteristics. All devices subsequently discussed were annealed at either 498K or 573K.

4 Force Microscopy Studies

Summary

Atomic and electrostatic force microscopy are valuable techniques for both mechanical and electrical device characterization. Atomic force microscopy can be used to give the number and orientation of fluorescing high aspect ratio nanocrystals (also called nanorods) in clusters, to probe the relationship between fluorescence intermittency and nanorod cluster size. Electrostatic force microscopy, which allows two-dimensional imaging of potential and charge flow in a thin sample, gives both quantitative and qualitative insight into the behavior of semiconducting and metallic nanocrystals.

4.1 Atomic Force Microscopy

Many different flavors of force microscopy have been developed to measure the force interactions between a macroscopically smooth sample and a cantilever probe. The cantilever has a resonant frequency of oscillation, and the quality factor of the oscillation is so high that interaction with electrostatic, atomic or other kinds of force from the sample surface affects the oscillation frequency. Because force microscopy relies on a mechanical interaction, it can be used to image samples on a scale far smaller than the optical diffraction limit. The use of different microscope probes and configured electronics enables measurement of many different forms of force.

The basic mode of force microscopy, atomic force microscopy (AFM), measures either the mechanical hardness of the surface or the van der Waals force, depending on whether contact or non-contact mode is used. The microscopy tip which probes the sample is a cantilever with a triangular tip that converges to only a few hundred atoms. The entire cantilever is driven to oscillate near the surface at a frequency close to the characteristic frequency of the tip. As the cantilever oscillates, its oscillation amplitude

can be affected by impact with the surface or, on a smaller scale, van der Waals or other forces due to the surface. The change in amplitude is highest when the tip is close to the resonant frequency. The oscillation of the tip is measured by a laser which reflects off the top side of the cantilever, and the changing amplitude is used to generate a topological map of the sample surface.

AFM is a scanning probe microscopy, similar to scanning tunneling microscopy or near field scanning optical microscopy, and like these other forms of microscopy it is serial. The pixels in an AFM image are read out in series, rather than in parallel as in an optical micrograph. For this reason, although it is possible to modify surfaces and pattern some kinds of samples using AFM,[91-93] it is difficult for scanning probe force-based lithography to commercially compete with parallel processes such as optical lithography.

The AFM used in the following experiments is a Veeco Enviroscope, which has capabilities that include an enclosed AFM chamber that can be put under a vacuum of 10^{-2} torr or filled with N_2 gas, an electronic feedthrough so that voltages can be applied to sample electrodes, and a heating stage for *in situ* thermal annealing. The tips used were Veeco TESP AFM Force Measurement tips and SCM-PIT Conductive AFM probe tips.

4.2 Blinking and AFM/TEM Correlations

AFM is an excellent experimental tool for many purposes, such as film thickness and surface uniformity measurements. It can also be used to measure the volume of nanorods in conjunction with TEM to learn how cluster size relates to blinking statistics for nanorods that have assembled into clusters.

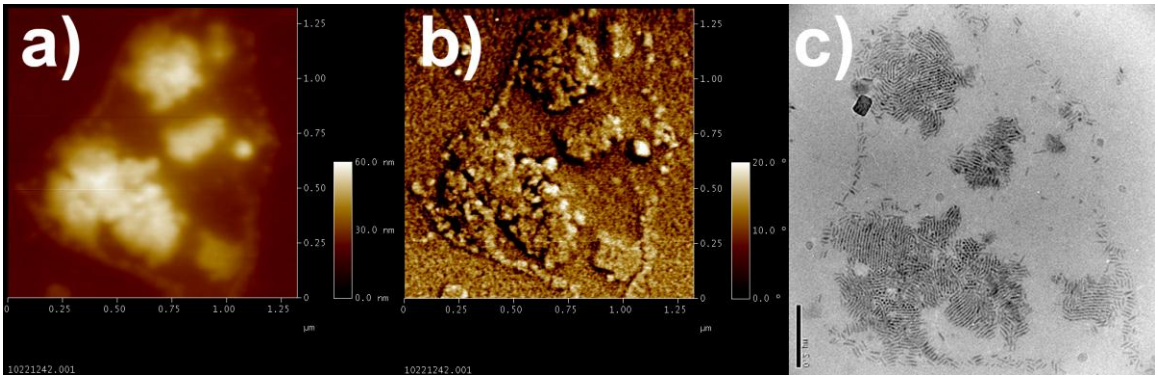

Figure 4.2.1. (a) AFM topography, (b) AFM phase, and (c) TEM of the same nanorod cluster.

CdSe/ZnSe/ZnS core-double shell nanorods, with a radius of 2.9 ± 0.2 nm and a length of 34 ± 0.3 nm, were drop-cast at a concentration such that the nanorods were arranged in submicron and micron-sized clusters that were either closely packed or well isolated with average intercluster spacing of tens of nanometers. **Figure 4.2.1** shows a sample cluster in AFM and TEM. Using AFM to measure cluster height and TEM to measure number of nanorods in the cluster base, the number of nanorods in each cluster can be determined. Structural details such as cluster area, orientation and distribution of nanorods within clusters can then be correlated to emission properties. The physics of blinking in semiconducting nanocrystals is complex, and not the focus of this thesis; thus the remainder of this section will give a brief overview of the blinking behaviors observed and correlated to cluster size. For a more detailed investigation the reader is encouraged to consult Siying Wang's dissertation.[94]

Fluorescence dynamics of semiconductor nanorod ensembles from the single particle regime to ~10,000 particles were observed. Fluorescence data are shown for a nanorod cluster in **Figure 4.2.2**, with the corresponding AFM and TEM. In the TEM image, the scale bar is 200 nm, and the arrow indicates laser polarization during excitation. For the integrated fluorescence intensity versus time graph, the red line is the region indicated in the inset, and the black line is a nearby background region with the same size.

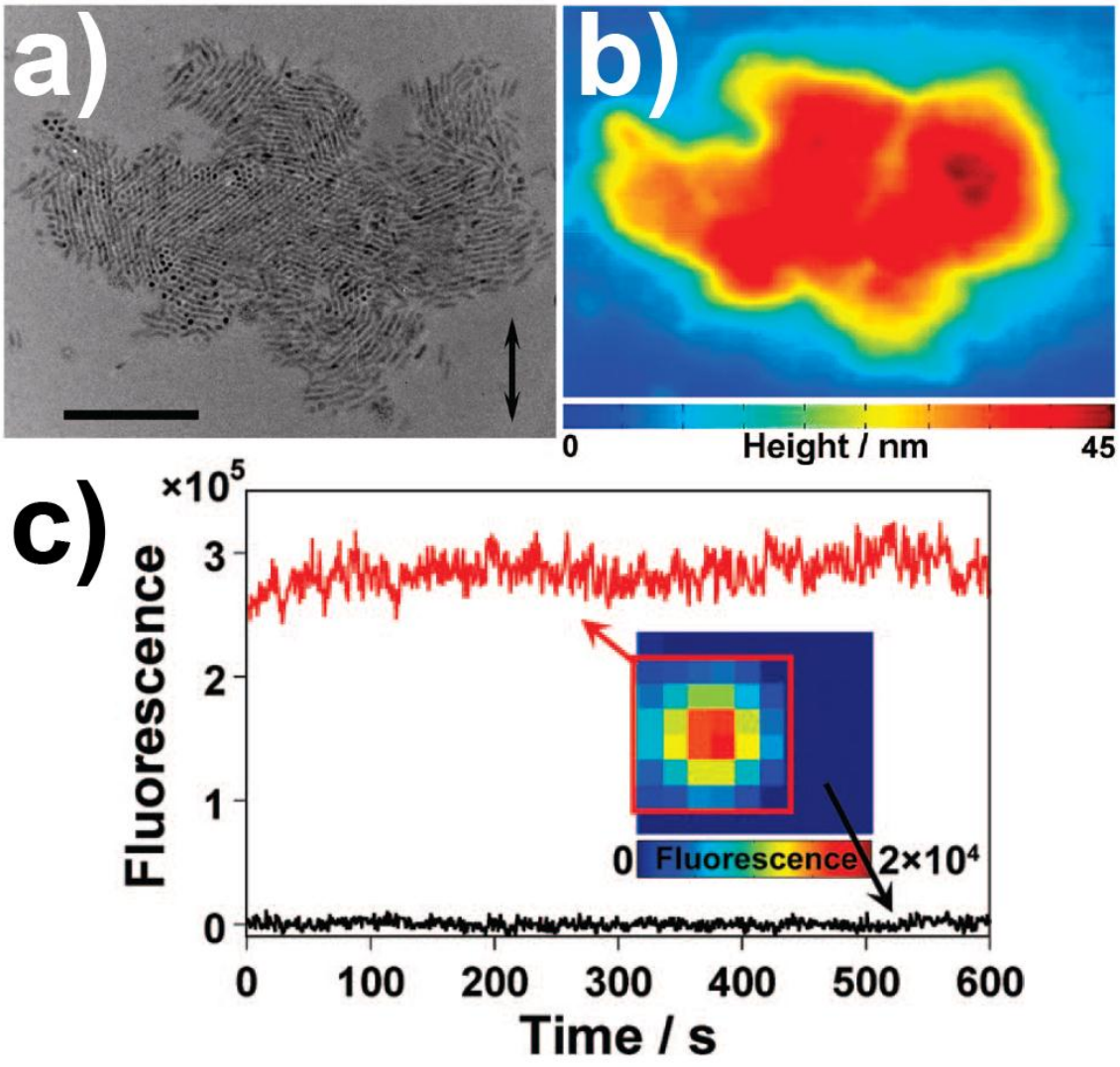

Figure 4.2.2. TEM, AFM, and integrated fluorescence for a nanorod cluster.

Different blinking regimes were observed depending on cluster size, all measured over tens of minutes. In small ensembles containing less than 100 nanorods, a nonzero residual fluorescence during "dark" periods was observed, superimposed by clear single-particle blinking events.[47] The fluorescence intensity from larger groups of more than ~100 nanorods, and closepacked clusters with several hundreds or thousands of nanorods, shows pronounced fluctuations, but with a mean intensity that is relatively constant in time.[47] The observed fluctuations can be as much as 40% higher than the mean fluorescence, even in clusters containing several thousands of particles. The contribution

from standing nanorods, whose orientation is perpendicular to the laser polarization, is less than the contribution from nanorods parallel to the substrate.[47] Overall, the emission intensity scales with increasing cluster size, additionally exhibiting memory effects and a dependence on irradiation intensity.[47]

4.3 Electrostatic Force Microscopy

Electrostatic force microscopy (EFM) is a technique based on AFM which can measure electrostatic force between a conductive scanning tip and the surface. Each line in an EFM image is constructed as follows: on the first pass, a regular AFM scan is performed to extract the surface topography. On the second pass, the tip is held at a fixed distance above the surface, based on the topography scan, and a voltage is applied to either the tip, a surface feature, or both. This procedure is shown in **Figure 4.3.1**, with the height scan on the bottom and the EFM scan on top.

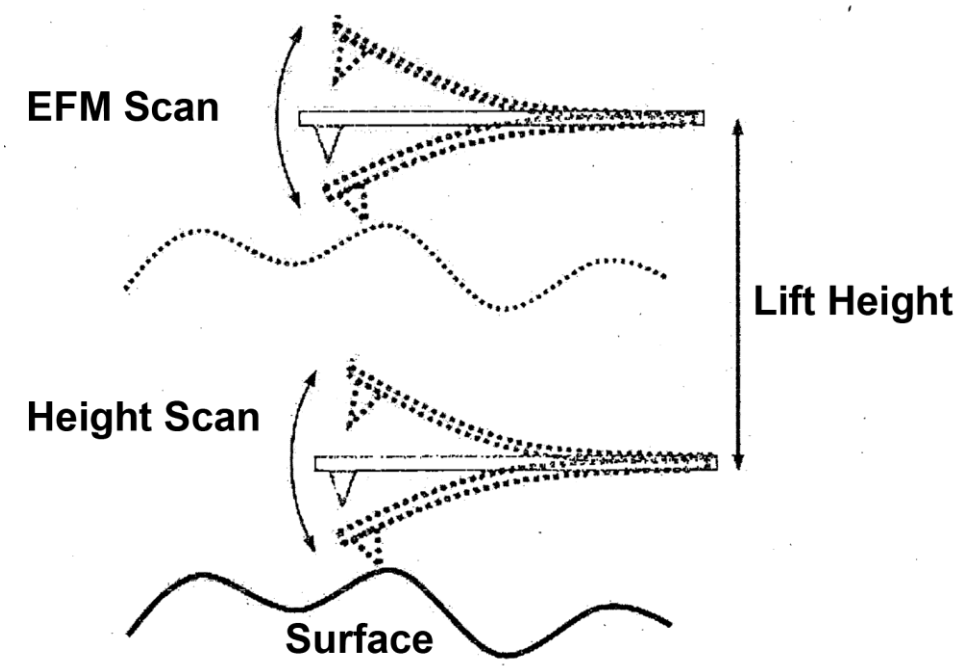

Figure 4.3.1. A diagram depicting the topography scan and the electrostatic force scan.

The electrostatic force interacts with the cantilever, and the change in oscillation

frequency depends on the magnitude of the force. This is how the EFM image is generated. This force is given by

$$F(z) = \frac{Q_s^2}{4\pi\varepsilon z^2} + \frac{Q_s(CV)}{4\pi\varepsilon z^2} + \left(\frac{dC}{dz}\right)\frac{V^2}{2}. \quad (4\text{-}1)$$

The first term is the Coulomb interaction between the static charge on the surface, Q_s, and an image charge induced in the tip, also Q_s, where the tip height above the surface is z.[95] The second term represents the interaction between Q_s and the capacitive charge of the tip at a bias voltage V. The third term is due to the capacitive interaction between the tip and the surface, which depends on the voltage difference between the tip and the surface.[96] Because of the thin SiN membrane, no substrate or gate term is present. The voltage applied can be either AC or DC.

In the studies of semiconducting nanocrystals, the nanocrystals were dried in a film between two metal electrodes pre-patterned on the surface. Small voltages of less than 5 V were applied to one electrode, with the tip held at 0 V. In the studies of metallic nanocrystals, there were no electrodes, so voltage was applied to the tip only and the image charge in the nanocrystals was observed.

4.4 EFM of Semiconducting Nanocrystals

EFM gives a two-dimensional map of where current flows in a nanocrystal solid. It can also show how strongly, or weakly, charge percolates through nanocrystals.[97, 98] EFM has been used to show that current paths in a nanocrystal solid are dependent on the locally varying thickness and continuity of an array.[98] Here, PbS nanocrystals in Au nanoelectrode gaps on a SiN membrane were studied using EFM. The PbS nanocrystals used had a diameter of 18 ± 2 nm and were capped with oleic acid and suspended in toluene. These nanocrystals were purchased from Evident Technologies, and the TEM in **Figure 4.4.1** shows the size distribution of nanocrystals in a representative cluster.

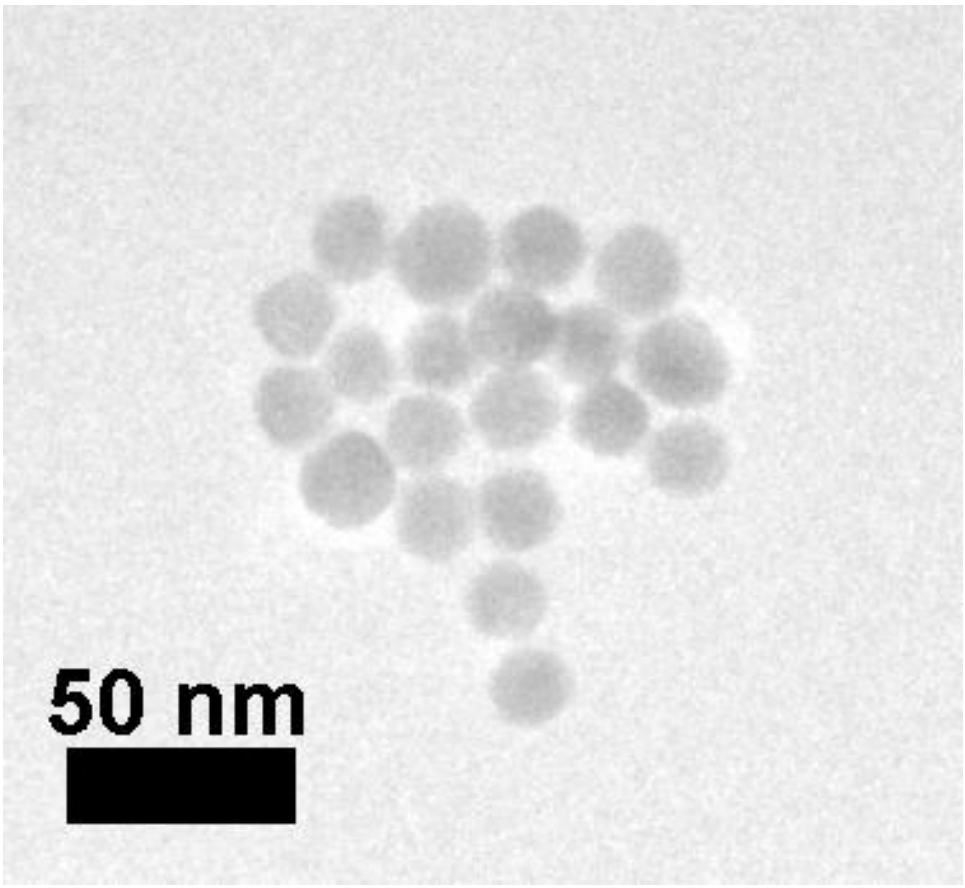

Figure 4.4.1. TEM of PbS nanocrystals.

EFM measurements were taken for bare electrodes with a small voltage (0-5 V) applied, which showed that the electric field is strongest over the electrode and spreads minimally on the bare substrate. This is shown in **Figure 4.4.2**: the upper electrodes are at -6 V, making them appear dark, and the tip and lower electrodes are both grounded, so the lower electrodes are not visible.

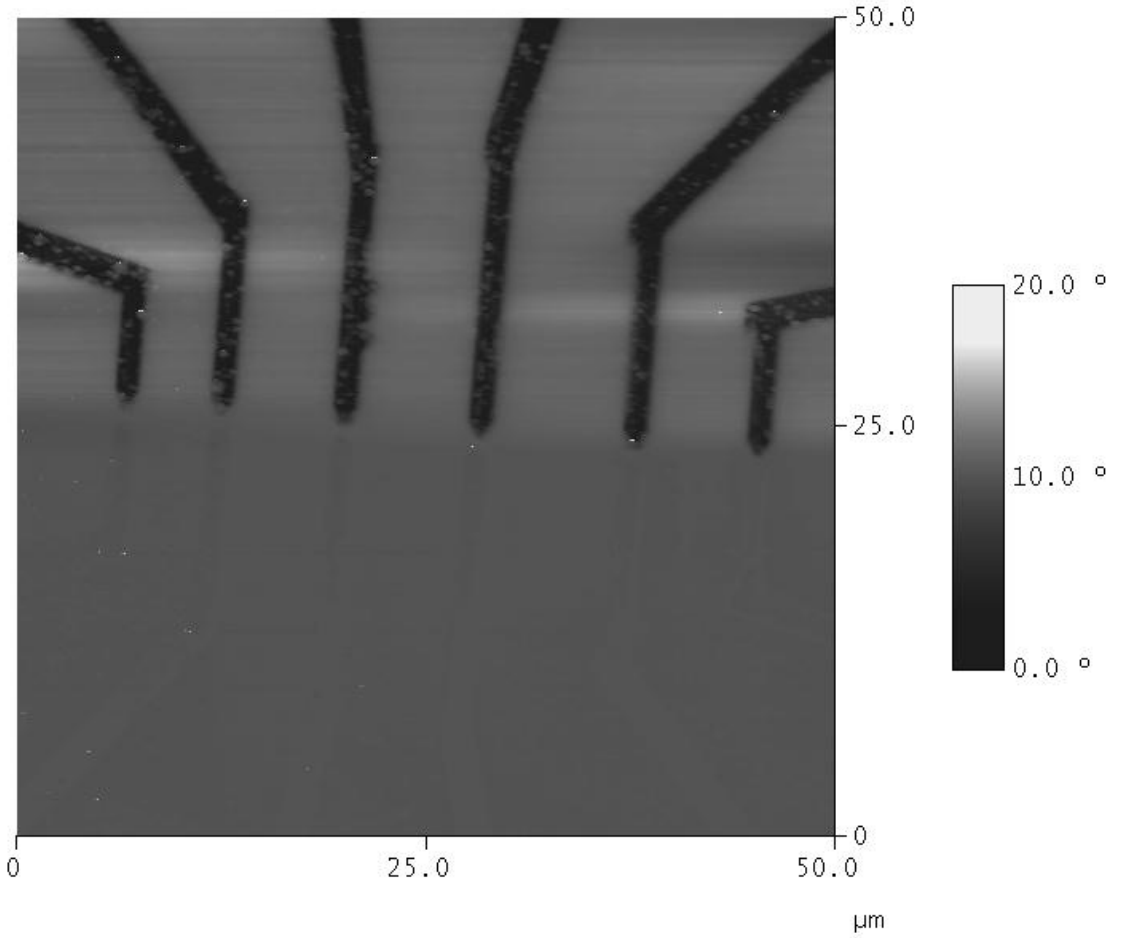

Figure 4.4.2. EFM of bare electrodes, with the top electrodes at -6 V.

Then a dilute solution of PbS nanocrystals was drop-cast onto the substrate, and AFM and EFM were performed. **Figure 4.4.3** shows that a thick film of PbS, shown on the upper electrode, does not allow charge to propagate and is thus very insulating. In this image, the electrode voltage is 5 V. This sample has not been thermally annealed, hence, the ligands still present a formidable tunneling barrier to conduction.

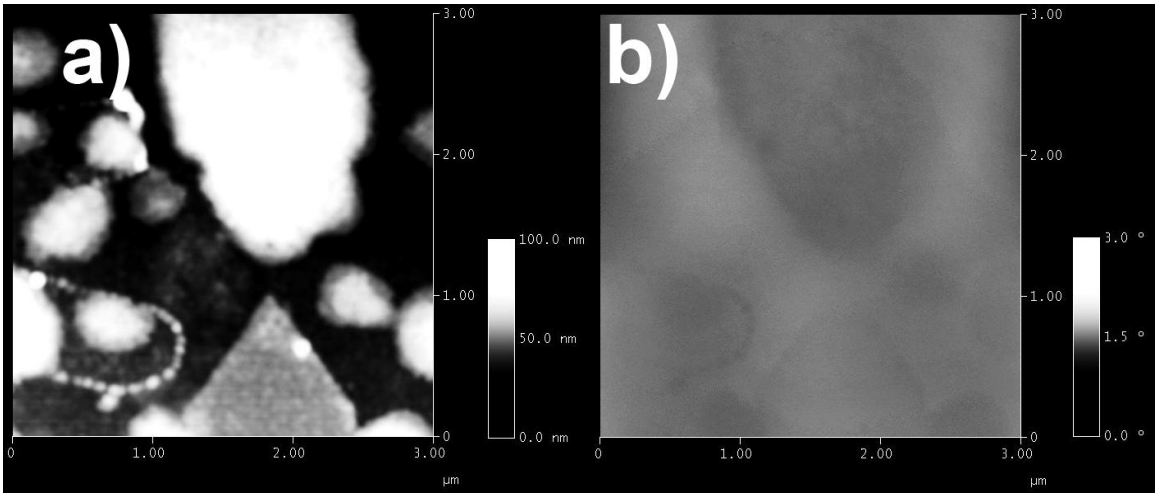

Figure 4.4.3. (a) AFM and (b) EFM for a two electrode device with PbS nanocrystals.

Given a voltage on the electrode, there should be a voltage drop with each nanocrystal in between the electrode and the EFM tip due to dielectric screening, which would cause the electrostatic force felt by the tip to be inversely related to the nanocrystal film thickness. The film thickness on the electrode can be estimated by subtracting the mean electrode height, as measured by AFM on the bare device before nanocrystal deposition, from the height measured by AFM for the electrode with the film on it. This film thickness can be used to correlate the dielectric screening with the nanocrystal volume, which gives an estimate of the dielectric constant of the nanocrystal film. The constant extracted will only be a rough estimate, because there will be some charge spread into the nanocrystal film. **Figure 4.4.4** shows a plot of EFM signal, which is a phase shift measured in degrees, versus film thickness, where the electrode thickness of 23.5 ± 1.5 nm has been subtracted from the topography of the electrode with the nanocrystal film.

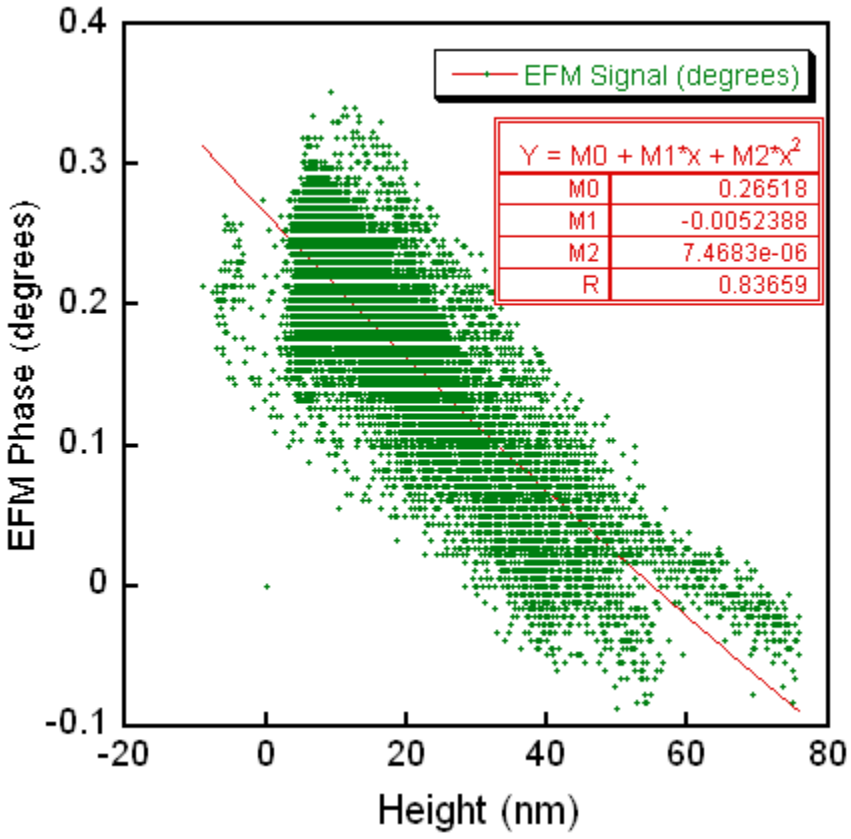

Figure 4.4.4. EFM phase data plotted versus film height.

While a trend is visible, the data shown in **Figure 4.4.4** are very scattered. One possible explanation is that the electrode height is not perfectly uniform, so using the mean electrode height will propagate electrode fluctuations into the film thickness. But when the data were processed by aligning and subtracting the bare electrode topography instead of the mean, the noise was considerably worse, so the electrode non-uniformity cannot be responsible.

With DC EFM measurements, in order to extract a dielectric constant from the line fit in **Figure 4.4.4**, several simplifying assumptions to Equation 4-1 are needed. In an AC measurement, it is possible to quantify the tip image charge using the voltage frequency response of the cantilever.[99] However, for this DC measurement since the tip image charge cannot be measured, it is ignored, which will make the expression less accurate but still qualitatively useful by causing the terms with Q_s to drop out. For the

capacitive term between the tip and the surface, the system can be treated as two infinite parallel plate capacitors in series, one of which has the nanocrystal film as a dielectric medium, the other of which has no dielectric medium. The total capacitance between the surface electrode and the tip, C, will then be given by

$$\frac{1}{C} = \frac{z}{\varepsilon_0 A} + \frac{h}{\varepsilon A} = \frac{1}{\varepsilon_0 A}\left(z + \frac{h}{\varepsilon_r}\right), \tag{4-2}$$

for a tip that is a distance z from a dielectric film with thickness h and dielectric constant ε. Here ε_r is a constant related to the dielectric constant of the material ε by $\varepsilon = \varepsilon_r \varepsilon_0$. This gives the following equation for electrostatic force measured by the EFM probe, given a voltage on the electrode of V:

$$F = \frac{1}{2\varepsilon_0 A} V^2 \frac{1}{\left(z + \frac{h}{\varepsilon_r}\right)^2}. \tag{4-3}$$

To get F from the raw EFM data, which is measured as the phase shift $|\Delta\nu|$, the relation

$$|\Delta\nu| = \frac{\nu}{2k}\frac{dF}{dz} \tag{4-4}$$

is used, where ν is the EFM cantilever resonant frequency and k is the cantilever spring constant. Using the experimental parameters, the dielectric constant of the nanocrystal film can be extracted from the EFM phase shift as a function of film height. For the cantilever used, $k = 42\ N/m$ and $\nu \sim 300\ kHz$. The voltage applied to the electrode was 4 V and the probe was scanned a distance of 100 nm above the sample surface. Applying these parameters to a numerical fit to the data in **Figure 4.4.4** gives $\varepsilon = 1.2 \times 10^{-3}$ for this PbS nanocrystal film, considerably less than the bulk dielectric constant of $\varepsilon = 170$.[100] This measured value for ε of the PbS nanocrystal film is too small to be physically accurate, and this is most likely due to the film and tip charging effects which were ignored. Clearly, AC EFM measurements are required in order to get a physically realistic number for the nanocrystal dielectric constant.[99] A larger value for ε in nanocrystal films compared to the bulk is expected, because of the difficulty carriers have passing through monolayers of nanocrystals, even after even thermal annealing.[98]

4.5 EFM of Metal Nanocrystals

Metal nanocrystals have a different response to applied voltages than semiconducting nanocrystals do, in part due to the higher carrier concentration of metal nanocrystals which causes them to polarize in an electric field.[95] Au nanocrystals 20 nm in diameter purchased from Sigma Aldrich were used, as shown in a transmission electron micrograph in **Figure 4.5.1**. These nanocrystals were suspended in water and capped with sodium citrate.

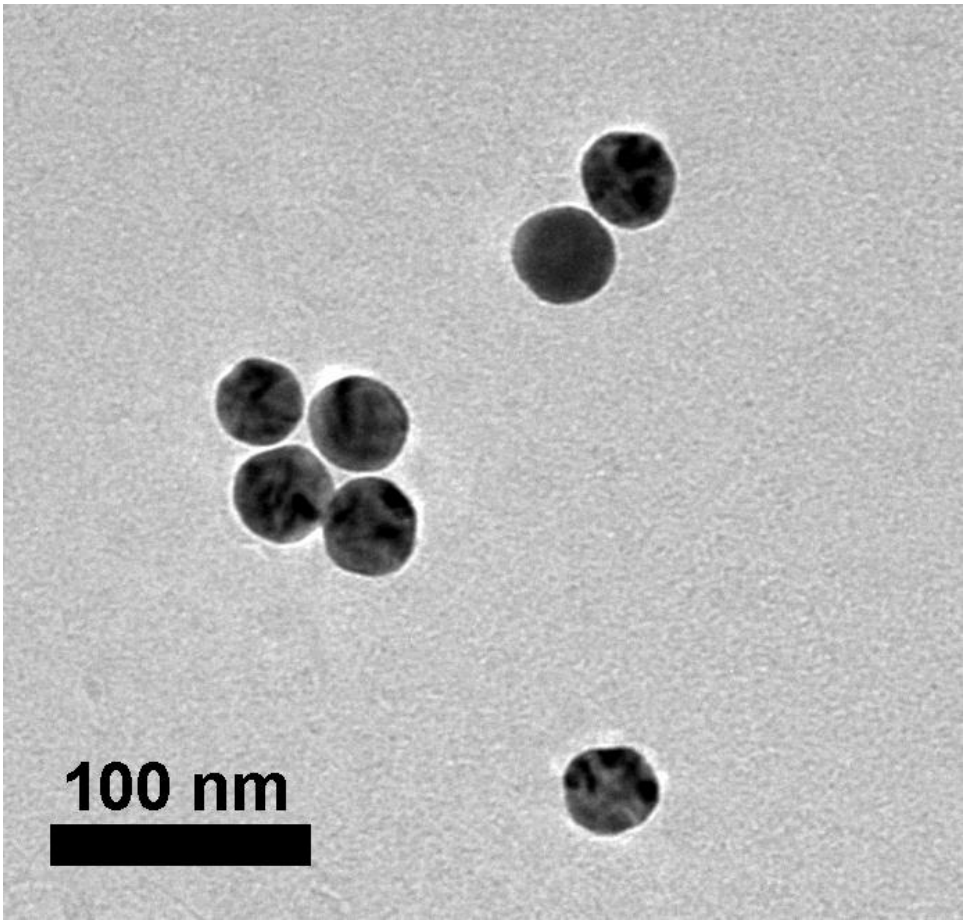

Figure 4.5.1. TEM of Au nanocrystals.

Samples were made by drop-casting Au nanocrystals onto a SiN substrate for AFM and EFM analysis. The Au nanocrystals did not assemble into a uniform layer as

was expected, but rather formed a thick, branched structure, as seen in the AFM topography scan in **Figure 4.5.2**a. EFM was performed with a voltage was applied to the tip of 2 V in **Figure 4.5.2**b and 4 V in **Figure 4.5.2**c.

The distinctive structures in **Figure 4.5.2** are called Brownian trees, a result of diffusion-limited aggregation during evaporation of the solvent.[101] In these samples, while the droplet of nanocrystal solution is drying, the nanocrystals diffuse on the substrate until they stick to any existing aggregation, without further diffusion. This dendritic cluster growth is governed by a fractional power law, making these structures an example of a two-dimensional fractal.[101]

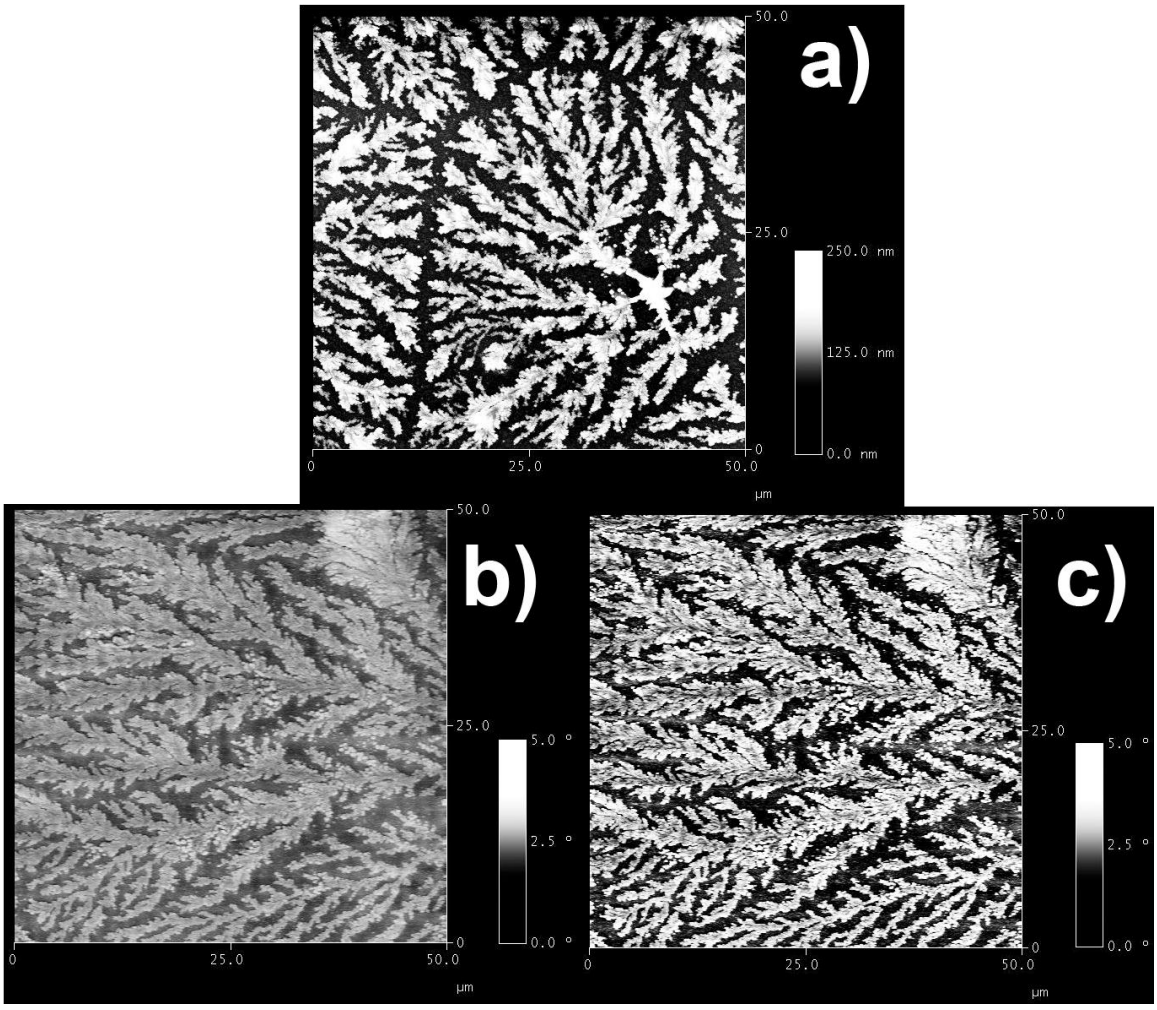

Figure 4.5.2. (a) AFM, and EFM with (b) 2 V and (c) 4 V on the tip, for a drop-cast assembly of Au nanocrystals on SiN.

The EFM signal from the gold structures increases as the tip voltage is increased, due to the polarization of the charge carriers in the gold. If the ligands in this system were removed by annealing, the Brownian trees would form a dendritic gold wire network. But the presence of the ligands before annealing ensures that the conduction mode within the nanocrystal branches will be driven by tunneling processes. From a conduction perspective, hypothetically the charge carriers should experience the Brownian trees as one-dimensional paths with occasional forks, implying that the conduction will be more dependent on temperature changes and cycling than it would be in a two-dimensional array.[102]

If semiconducting nanocrystals were drop-cast so that they filled the voids between the dendritic metal clusters, any electric field applied to the metal would result in highly inhomogeneous fields in the voids, which in some places would be strongly enhanced by the fractal metal shape. Previous studies using mixtures of semiconducting and metal nanocrystals show that photoconductivity in semiconducting nanocrystals is affected by even a very small number of metal nanocrystals.[68, 103] The electric field modifications that metal nanostructures and their resonances cause will be discussed in more detail in the following chapter.

5 Plasmonic Field Enhancement

Summary

Nanoscale metals exhibit resonant coupling to incident light which arises because of their size and high carrier concentration. In this section, the localized surface plasmon polaritons and plasmon modes in nanoscale metal pillars are discussed. Coupling between surface plasmons and nanocrystals has been previously shown,[104] and has potential applications for photodetectors[105] and fluorescence enhancement.[106] Devices were created to determine whether an array of such pillars can be used to enhance the electric field on semiconducting nanocrystals in a photosensitive device. This has the potential to improve device performance by increasing charge separation efficiency.

5.1 Plasmon Resonance in Nanoscale Metals

In semiconducting devices, metal electrodes are used to apply a voltage difference that creates a uniform electric field across the semiconductor. The electric field biases current flow and separates photogenerated excitons for collection. Conductors with nanoscale spacing, such as electrodes in a nanogap, can generate strong electric field enhancements, where the confined fields exhibit the characteristics of a transverse electromagnetic waveguide mode.[107] Additional resonances of the charge carriers can be excited in a nanoscale metal. The electron gas in a metal can experience collective charge density oscillations, and a plasmon is the quantized quasiparticle of these oscillations. Under illumination, incident photons can drive the plasmon oscillations if the photons are at a resonant wavelength. This driven oscillation due to coupling between the photon, the plasmon resonance, and the polarization of the medium is called a surface plasmon polariton. A surface plasmon polariton at a metal interface is shown schematically in **Figure 5.1.1**a.

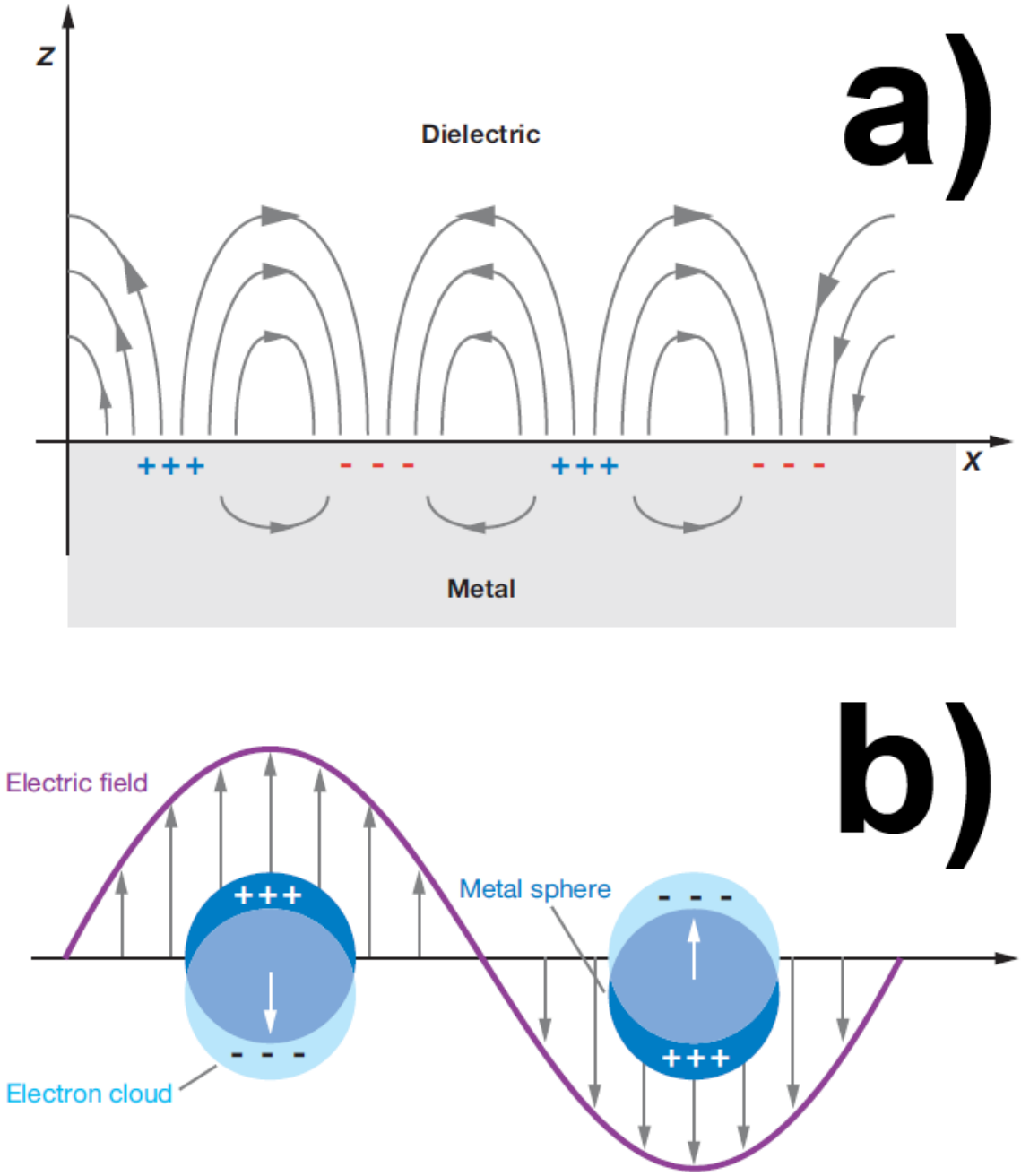

Figure 5.1.1. (a) Surface plasmon polaritons and (b) localized surface plasmon polaritons.[108]

On a rough metal surface, where surface features are below the wavelength of incident light, plasmonic modes will be excited in the metal. Any interactions with surface molecules, enhanced by the plasmonic coupling, affects refractive index and

absorption. This effect can be used as a probe of surface interactions, and is the basis of surface plasmon resonance spectroscopy as well as surface-enhanced Raman spectroscopy.[109, 110] Plasmonic structures can also be used to couple and guide optical signals at a resolution below the diffraction limit, by using surface plasmon polaritons in metal structures smaller than the wavelength of incident light.[111]

While any nanoscale feature on a metal surface can plasmonically couple to light, if the metal object is nanoscale in all three dimensions, the charge oscillations are localized by the object size, creating localized surface plasmon polaritons. Whether resonant excitation occurs or not depends on the wavelength of the light and the size of the object, in addition to the carrier density. This is pictured in **Figure 5.1.1**b for two metal nanocrystals and a photon.

5.2 Theory of Plasmonic Response

A very simple equation for the resonance of a spherical metal nanocrystal with incident light can be derived using the Drude model for a free electron metal, which assumes that the electrons are acting in phase.[112] For objects whose size, ℓ, is much smaller than the wavelength of incident light, λ, the resonant frequency ω_r is given by

$$\omega_r = \sqrt{\frac{Ne^2}{m_e \alpha_{cl}}}. \qquad (5\text{-}1)$$

Here N denotes the total number of conduction electrons in the sphere, e is the charge of an electron, m_e is the mass of an electron, and α_{cl} is the polarizability of a metal sphere of radius r

$$\alpha_{cl} = 4\pi\varepsilon_0 r^3.^{112} \qquad (5\text{-}2)$$

This model gives the correct size dependence for the plasmon resonance of an isolated metal sphere, despite the unphysical assumption of electrons acting in phase. The most general mathematical approach to a sphere interacting with an electromagnetic field was presented by Gustav Mie.[113] In order to express the internal electromagnetic field in terms of spherical wavefunctions, one can use Maxwell's equations, and express both the incident plane wave and the scattering field from the particle using multipole expansions.

By applying the spherical surface boundary conditions, analytical solutions are obtained which depend on spherical Legendre functions, cylindrical functions, and a size parameter. This derivation is not presented here for brevity's sake, but it can be found in the textbook by Bohren and Huffman in addition to Mie's original paper.[113, 114] The solutions, though derived from classical physics, contain a phenomenological quantum term in the form of the dielectric function $\varepsilon(\omega, r)$ which depends on the incident photon frequency and the nanocrystal radius.[114] The dielectric function for bulk metals is generally governed by transitions within the conduction band. However, in nanoscale metals, the r –dependence arises when the size of the particles is smaller than the mean free path of an electron.[114] Collisions with the edge of the nanocrystal then dominate the mean free path, changing the dielectric function.

In the case where $\lambda >> \ell$, Mie's formalism can be simplified further by treating the electromagnetic field as approximately constant over the object. This constant applied field will polarize the metal, and in fact a metal sphere can be replaced in the formalism with an ideal dipole. [114] This is because the time required for a signal to propagate across the sphere is much smaller than the characteristic time of the incident field, which is the inverse of the frequency.[114] Thus the excitations will take the form of electric multipoles, as shown in **Figure 5.2.1**.

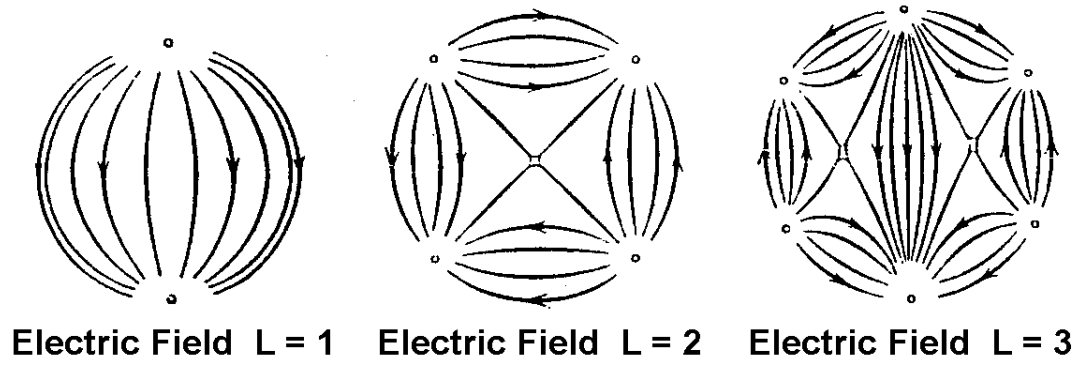

Figure 5.2.1. Electric multipoles observed at a distance due to surface plasmon polaritons on a nanocrystal.[112]

While more commonly observed in metals, localized surface plasmons have also been observed in doped semiconducting nanocrystals with a similarly high carrier

density.[115] Undoped semiconducting nanocrystals can be affected by nearby plasmonic structures via interactions with the plasmonic electric field. With nanostructured metals, the complex non-uniform electrostatic environments modify the dielectric, or Förster, coupling of excitons in two neighboring nanocrystals.[116] A logical question for device design is, is it possible to include objects with a plasmonic resonance in a photodetector, to enhance the device sensitivity by applying a locally higher electric field without risking destruction of the electrodes by applying a higher voltage? Electric field enhancement has been observed in metal nanoparticles connected by a molecule,[117] and by mixing metal and semiconducting nanocrystals.[68] In the following experiment, an array of plasmonically resonant pillars is lithographically defined with the goal of enhancing the electric field, and thus carrier separation, for a semiconducting nanocrystal film.

5.3 Design of Plasmonic Metal Pillars

To see plasmonic enhancement of electric field, devices were made where the gap area contained an area of gold pillars. The nanogap was 1 μm to give adequate space for the pillar array. Electron beam lithography was used to pattern both the nanoelectrodes and the pillars. The pillars had the same metal composition as the electrodes, 30 nm of Au on top of 3 nm of Ni. An electrode gap containing a metal pillar array is shown in TEM before nanocrystal deposition **Figure 5.3.1**a, and the pillars are shown up close in TEM after nanocrystal deposition in **Figure 5.3.1**b.

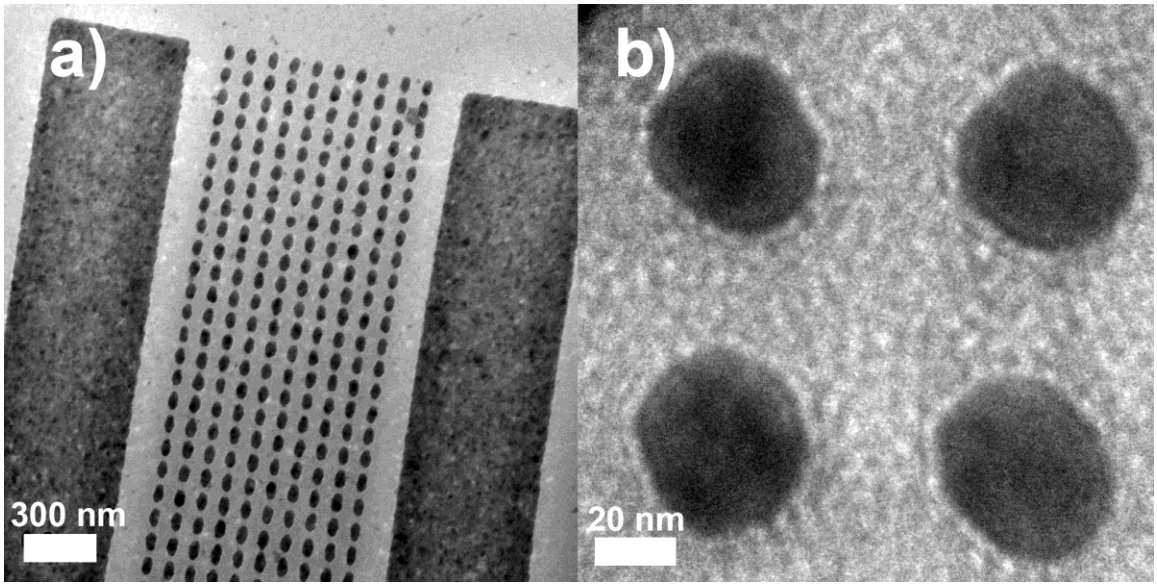

Figure 5.3.1. Metal pillar arrays, (a) before and (b) after nanocrystal deposition.

The pillar size and spacing determine the plasmonic response: the pillar size affects what wavelength of illumination causes localized surface plasmon resonance, and as the pillars move closer together they interact such that closer pillar spacing redshifts the response wavelength.[118] This wavelength dependence is shown below in **Figure 5.3.2**.

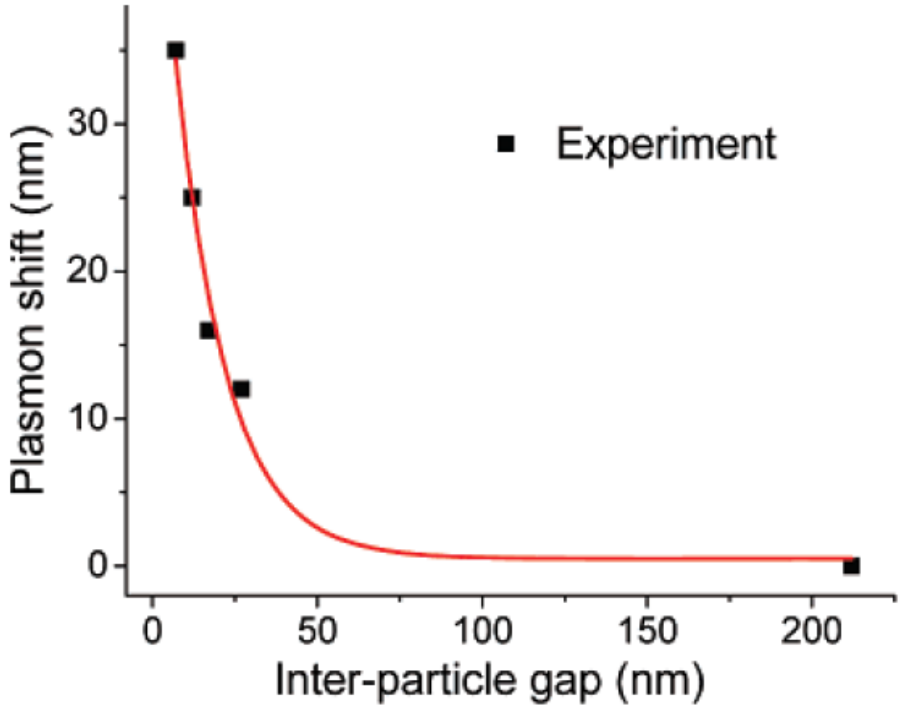

Figure 5.3.2. Plasmon resonance shift versus interparticle gap, adapted from Ref. [118].

Using 40 nm diameter pillars, with a spacing of 30 nm, gives non-interacting pillars with a plasmon resonance of 530 nm. A square lattice of pillars was chosen to minimize liftoff difficulties. CdSe/ZnS nanocrystals were then drop-cast to create devices; these nanocrystals had a diameter of 5.2 ± 0.6 nm and an absorption peak of 610 nm.

5.4 Photocurrent of Nanocrystals in Plasmonic Devices

Once the devices were installed in a cryostat, they were confirmed to have no dark current with or without nanocrystals. Then photocurrent was measured at various wavelengths to observe whether the plasmonic resonance of the metal pillars affected the photoresponse. The light source used was a white lamp whose output was wavelength selected by a series of spectrometers and then passed through a fiber and focused onto the

device active area. Wavelengths from 400-900 nm were used, with a light bandwidth of 25 nm. The intensity of the focused light varied depending on wavelength from 10-100 µW.

These devices had a high capacitance due to the large interelectrode spacing. Traditional I-V measurements, even at a low sweep rate, had a large amount of hysteresis which made measuring current values challenging. An alternate measurement procedure was developed due to this capacitance, pictured in **Figure 5.4.1**.

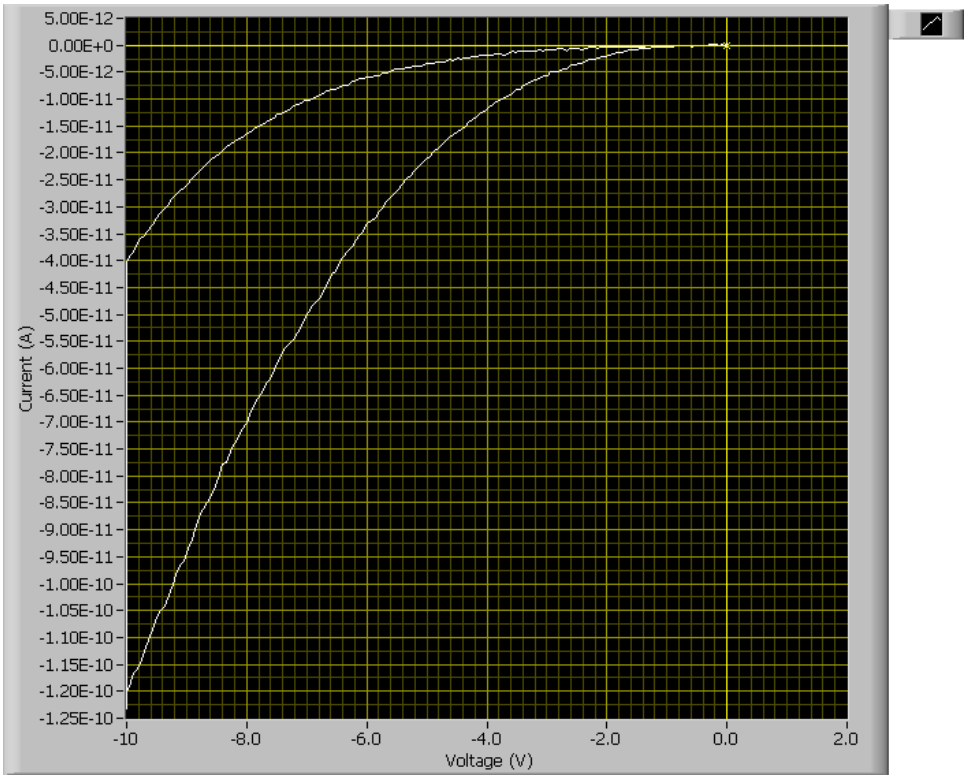

Figure 5.4.1. I-V measurement with delay to account for hysteresis.

To measure photocurrent at a particular wavelength, the voltage was swept to -10 V, held at -10 V for ten minutes, and then swept to 0 V. The current readings at 0 V before and after the applied voltage provided values with which to calculate the current offset. This offset has already been subtracted from the data in **Figure 5.4.1**. The long period of time at -10 V allowed current to stabilize, and only the final 30 seconds of data were used

to calculate the average photocurrent. This procedure was performed at several different wavelengths, with the final photocurrent values normalized for differences in illumination intensity.

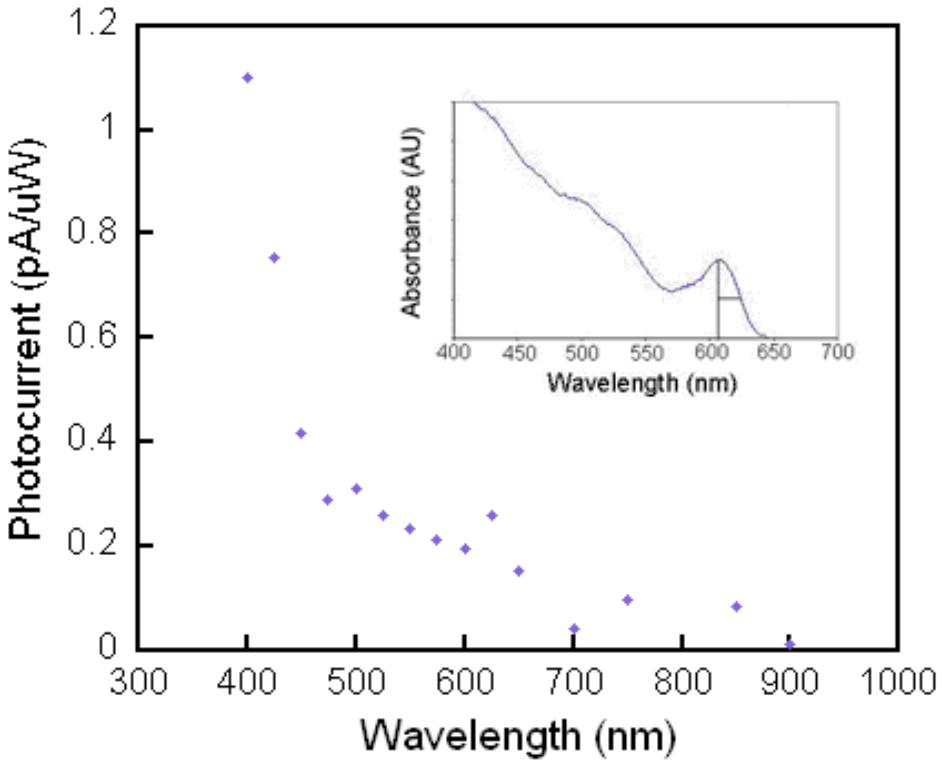

Figure 5.4.2. Normalized photocurrent plotted versus wavelength. Inset: Nanocrystal absorption.

Results are graphed in **Figure 5.4.2**, with the absorption curve for the nanocrystals as the inset. The primary absorption peak of the nanocrystals at 610 nm is clearly visible on both graphs, as expected. A small enhancement of the photocurrent signal is observable at the plasmonic resonance of 530 nm. This wavelength is the location of the second absorption peak, but the photocurrent response is larger than would be expected simply from the peak, by approximately 10%. The wavelength at which plasmonic effects are observed depends on the pillar spacing and composition. Identical devices with silver instead of gold electrodes were made, but silver is much more difficult to work with and degraded when exposed to the necessary measurement treatments that

remove barriers to nanocrystal conduction. These plasmonically enhanced devices exhibited the same memory effects observed in other semiconducting nanocrystal nanogap devices, indicating that the plasmonic coupling to the pillars does not affect device memory. Plasmonic enhancement of photodetector performance by up to 160% has also been observed for a device with an array of holes rather than pillars, using InAs nanocrystals.[105] These measurements support evidence from other groups that nanostructured plasmonic materials are a promising avenue to improve photosensitive device performance.[119]

6 Memory and Traps in Nanocrystal Films

Summary

Semiconductor nanocrystal arrays are artificial solids with many potential optoelectronic applications. [3, 6, 10] Many nanocrystal photoproperties have been studied, such as quantum yield in suspension, [9, 120] photoconductivity in films, [14, 82, 121] and carrier recombination rates. [122-124] Photoconductivity in CdSe/ZnS nanocrystal arrays has been found to follow a simple two-site resonant-tunneling model which describes the probability of electron-hole pair separation as a function of applied electric field. [82] The resonant-tunneling model can qualitatively reproduce the field dependence of the photocurrent, which also depends on interparticle spacing, nanocrystal size, and surface passivation.[82] Nanocrystal-based photodetectors have been realized, [3, 14, 82, 121, 125] but their stability over time may be compromised by charge traps that can cause variations in conductivity. In particular, the dark current, photocurrent, and photoconductivity temperature dependence of nanocrystal arrays all exhibit memory effects. [1, 80, 125]

In this chapter, a robust and reproducible procedure for controlling the trap population in nanocrystal nanogap devices is demonstrated, showing that qualitatively different photocurrent behaviors can be produced depending on how traps are initialized prior to a measurement. Electric field induced population and optically induced depopulation of traps can reverse the temperature dependence of the photoconductivity in two-terminal electrode devices containing CdSe/ZnS nanocrystal arrays. A model is presented that explains the role of traps and the importance of measurement sequence. This method for dynamically controlling trap populations achieves optimized photodetector sensitivity at low or high temperatures for light sources, photovoltaics, electronics, and other applications. Moreover, a range of temperature-dependent behaviors previously attributed to material differences are reproducible in a single device and provide a possible explanation for contradictory reports of the temperature

dependence of photoconductivity in the literature.[1, 12, 14, 80, 82, 121] Photocurrent in nanocrystal films had been found to increase with temperature[82] or decrease with temperature,[14] and it was proposed that adding a shell to the nanocrystal caused the different behavior.[14] In contrast, it is shown here that the illumination and electric field history of the film can affect the photocurrent temperature behavior by changing charge trap populations, which provides a reasonable framework for previously published results as well as explaining these seemingly contradictory results.

Photocurrent temperature dependence can be altered by cycling voltage either under illumination or in the dark prior to measurement, and the change in photocurrent saturates after a few hours. The energy required to excite carriers from trap states into the conduction band is less than the band gap energy, implying that sub-band gap illumination of nanocrystals can affect the overall charge state of the sample by exciting carriers out of the traps. This in turn, changes the photocurrent measured later. Therefore, sub-band gap illumination of devices affects the photoconductivity, even though sub-band gap excitation is not energetic enough to result in measurable photocurrent. Interestingly, sample exposure to sub-band gap illumination prior to photocurrent measurements is more effective at modifying the photoconductivity than the band gap illumination, even though sub-band gap illumination does not induce a measurable photocurrent. These effects can be explained by the emptying and filling of charge trap levels located within the band gap. Sub-band gap excitation may be closer in energy to the trap levels and is more effective at depopulating traps than light whose energy is larger than the nanocrystal band gap.

These results advance the understanding of charge-transport-based semiconductor nanocrystal devices, such as photodetectors and solar cells, and suggest methods to adjust performance in situ by emptying or filling charge traps using light and electric fields.

6.1 Initial Measurements of Photocurrent Memory

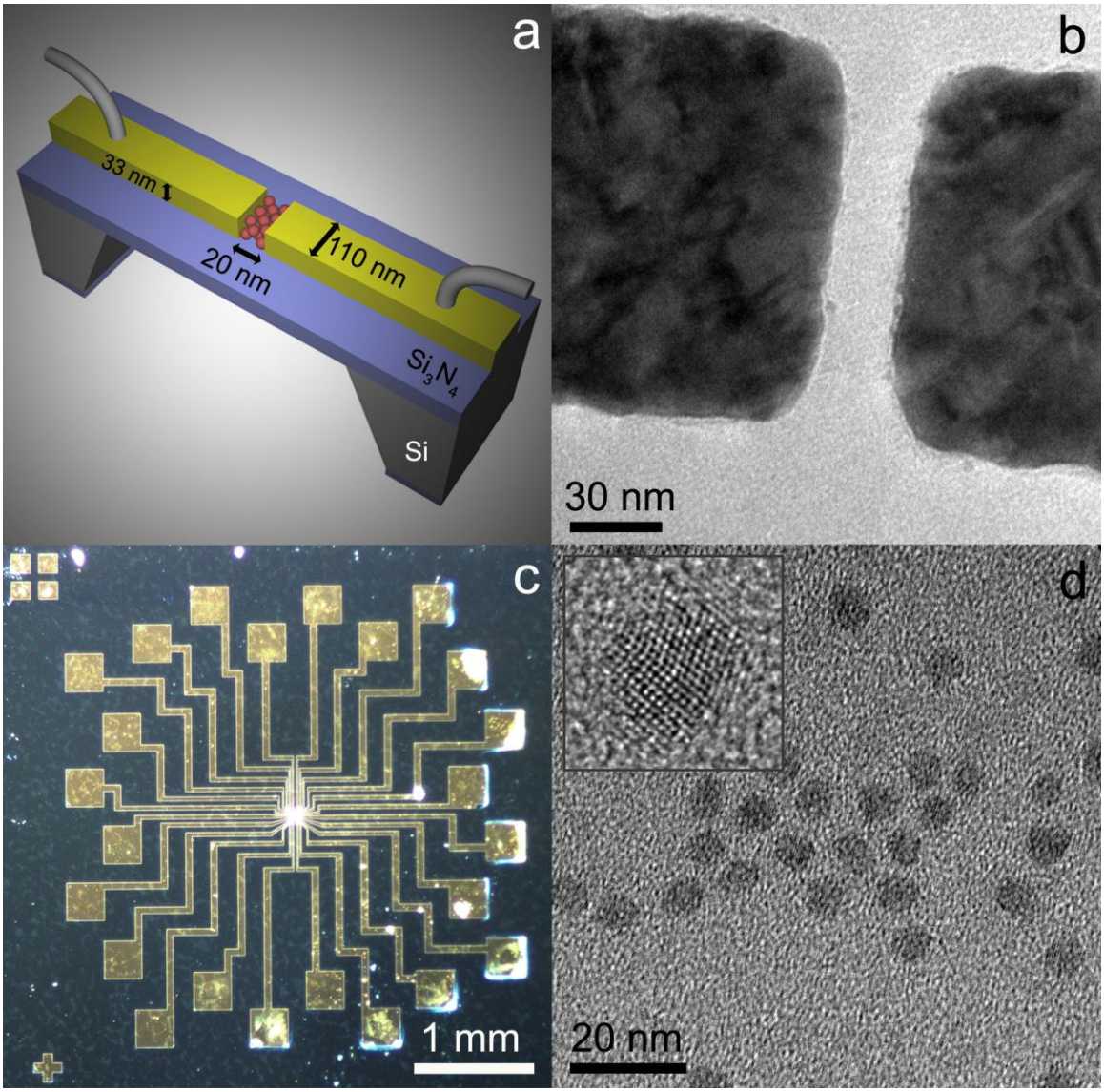

Figure 6.1.1. (a) Schematic of the photodetector nanogap device. (b) TEM image of the electrodes prior to nanocrystal deposition. (c) Optical image of the device with 12 electrode pairs. (d) TEM images of several nanocrystals and a single nanocrystal.

Figure 6.1.1a shows the schematic representation of the photodetector device measured, based on nanocrystals in a nanogap electrode geometry.[125] Electrodes made of 3 nm of nickel and 30 nm of gold, separated by only 20-30 nm, ~4 nanocrystal diameters, are patterned using electron beam lithography on a 40 nm thick silicon nitride (Si_3N_4) membrane that is supported by a Si wafer.[76] Nanocrystals are eventually deposited on the electrodes and substrate, forming a few-layer film in the active gap area. The membrane is compatible with high-resolution structural characterization using TEM, which allows us to confirm that the nanogaps did not have any metallic debris, as shown in **Figure 6.1.1**b. An optical image of lithographic features on a typical device is shown in **Figure 6.1.1**c. For more details on device fabrication, please see Chapter 3. One advantage of nanoscale gaps is that the application of relatively small voltages yields high electric fields in the gap area. For a 20 nm gap with a bias voltage of 2V, the field strength experienced in the 2000 nm^2 of active area is 10^8 V/m. This gives a maximum voltage drop per nanocrystal of 0.5 V. The active area of these photodetectors in comparison to previous literature[12-14] is decreased by six orders of magnitude in area and decreased in gap size by two orders of magnitude.

CdSe/ZnS core-shell nanocrystals were used, as shown in **Figure 6.1.1**d, with a mean diameter of 5.2 ± 0.6 nm and mean ZnS shell thickness of 0.2 nm. The primary absorption peak in solution was at 610 nm and the emission peak was at 640 nm. Five microliters of nanocrystal solution were drop-cast onto the 5 by 5 mm SiN/Si chip, forming a ~20-nm-thick multilayer nanocrystal film on the surface. Film thickness was determined by using AFM on a similarly prepared sample. The nanocrystal film was thermally annealed in vacuum by heating to 573K for 2 hours, which improved film conductivity by decreasing the inter-nanocrystal separation and increasing the coupling.[12-14, 80] Annealing at this temperature improves the conductivity by about two orders of magnitude.[12] For more characterization of the nanocrystals used, see Section 2.1.

Figure 6.1.2 shows an optical image of an entire chip after nanocrystal deposition, annealing, and photocurrent measurements. **Figure 6.1.3** shows two TEM images of different nanogaps on the same chip after nanocrystal deposition, annealing,

and photocurrent measurements. The nanocrystal film in the gap area appears blurred due to the thickness of the film.

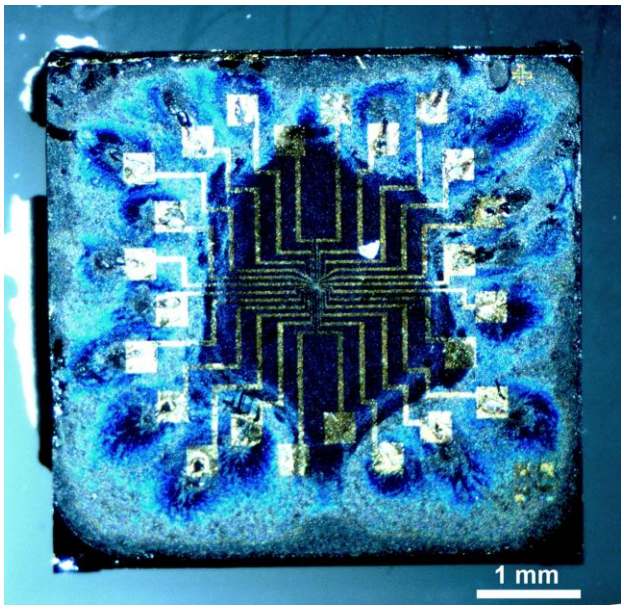

Figure 6.1.2. Optical image of a device with annealed nanocrystals after measurement.

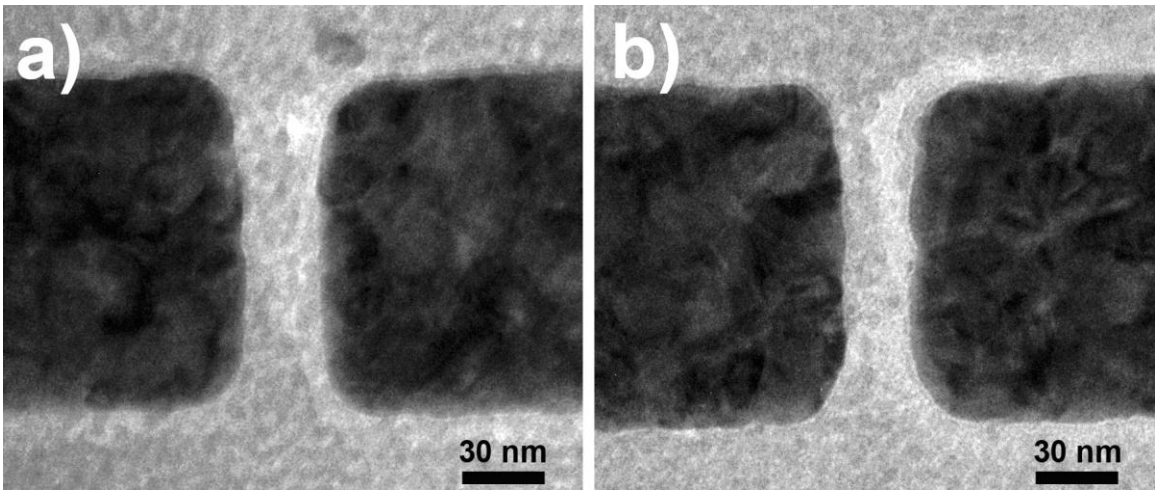

Figure 6.1.3. TEM of two nanogaps after measurement with nanocrystals annealed at 498K.

The dark current of devices was measured by performing an I-V sweep with the nanogap in the dark, and photocurrent was measured by performing an I-V sweep while the nanogap was illuminated by a continuous wave 532 nm diode laser. In each measurement set, the dark current of all devices on a chip was measured at room temperature, and then the photocurrent of the same devices was measured. The device was then cooled with either liquid nitrogen or liquid helium, and both dark current and photocurrent were measured again at low temperature. Changing measurement order, e.g. performing low-temperature measurements first and room-temperature measurements second, did not affect current characteristics.

The samples were thermally annealed *in situ*. For more details about the effect of annealing on photocurrent and dark current measurements, see section Annealing and Improving Conduction. Photocurrent was detected in 17 out of 24 nanogaps, and no dark current signal above the maximum noise floor of ~0.03 pA at 295K and ~0.15 pA at 78K in 70% of devices after annealing up to 573K. TEM imaging confirmed that nanogaps did not have any metallic debris that could contribute to the dark current, and this was consistent with subsequent I-V characterization of the nanogaps. More importantly, all of the measured photocurrent is primary, as it is a result of direct exciton generation in the nanocrystals and there is no measurable charge injection from the metal electrodes into the nanocrystal film, which would be measured as dark current.[121]

Background I-V measurements, between -2V and +2V at 0.04 V/s, ensured that the bare device had no dark or photocurrent. The maximum electric field magnitude in the active gap area was between ~ 9×10^6 and ~ 7×10^7 V/m, depending on gap size. The dark current after nanocrystals were annealed was negligible, indicating that measured photocurrent was due to carrier photogeneration in the nanocrystals and not injected carriers from the electrodes. For photocurrent measurements, the laser beam was centered on the SiN/Si chip, and all gaps were illuminated equally. An illuminated device is shown in the photograph in **Figure 6.1.4**.

Figure 6.1.4. Device under illumination from a green laser.

The stability of the photocurrent was then investigated. Between photocurrent measurements, the voltage was swept continuously, and the device was either left in the dark or illuminated. **Figure 6.1.5** shows I-V curves in the dark and under 532 nm illumination for a single device. Because of the small gap size, photocurrents were on the order of pA which is lower than in larger devices,[12-14] but well above the dark current and the RMS noise floor of ~5 fA. The black and purple curves are I-V curves for dark current and photocurrent of the bare device at 295 K prior to nanocrystal deposition. The blue curve shows dark current for a device after nanocrystal deposition. The other I-V curves in this figure (green, orange, light blue, and red) are photocurrent I-V curves at 78K after nanocrystal deposition.

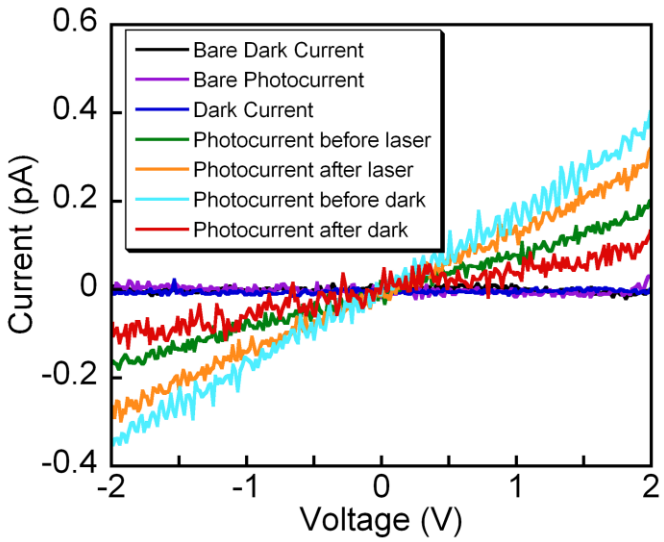

Figure 6.1.5. I-V curves in the dark and under 532 nm illumination, for a device before and after nanocrystal deposition and laser or dark voltage treatments.

The difference in these curves is a result of the different sample histories prior to the I-V measurements. In particular, after cycling the voltage while illuminating the sample with a laser overnight, the photocurrent at 78K increases, shown by the green and orange curves in **Figure 6.1.5**. Conversely, after cycling the voltage in the dark overnight, the photocurrent at 78K decreases, shown by the light blue and red curves in **Figure 6.1.5**. This process was reversible and reproducible for all devices.

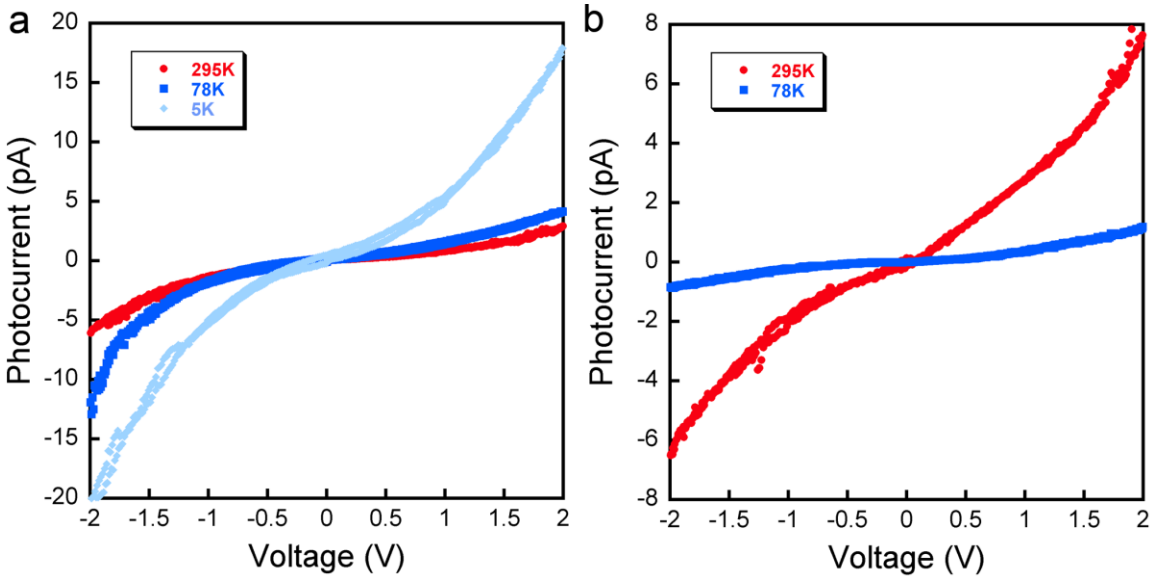

Figure 6.1.6. Photocurrent vs. voltage curves at various temperatures.

Figure 6.1.6 shows the I-V response under 532 nm illumination at different temperatures for CdSe/ZnS nanocrystals in two different nanogaps. Photocurrent at 5K (light blue), 78K (dark blue), and 295K (red) for CdSe/ZnS nanocrystals show that the low temperature photocurrent can be either higher, as in **Figure 6.1.6**a, or lower, as in **Figure 6.1.6**b, than the room temperature photocurrent. The photocurrent is well described by a second-order polynomial in voltage. Measurements at other wavelengths show similar behavior once temperature-dependent absorption shifts are accounted for; see **Figure 6.5.1** for I-V characteristics obtained using different illumination wavelengths. Over all measured devices, the initial room temperature photocurrent was in the range of 0.1 to 50 pA, with a mean value of ~5 pA, and the initial low temperature photocurrent was in the range of 0.1 to 240 pA, with a mean value of ~30 pA. A histogram of photocurrent values is shown in **Figure 6.1.7** for all measured data using a 532 nm laser. The large variation in measured photocurrent is probably due to the small number of nanocrystals in the nanogap; thus the variations in each individual nanocrystal are not averaged out. Additionally, film thickness within the nanogap and the energy barrier at the contacts between the nanocrystals and the electrodes may vary. Transport

through the nanocrystals inside the gap dominates the photocurrent, while nanocrystals outside the gap region have a negligible contribution.[2] Although more than just the gap area is illuminated, outside the gap, the high barrier to interparticle transport and the low field prevent significant contribution to photocurrent. See Section 3.4 for optical and TEM images of measured nanogaps.

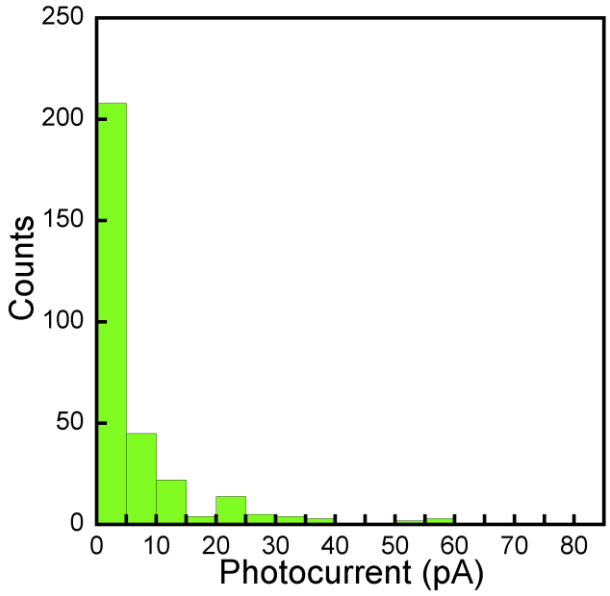

Figure 6.1.7. Photocurrent magnitudes for nanogap devices illuminated with 532 nm light.

The magnitude of the measured photocurrent depends on the recent illumination history of the device. Even more strikingly, some nanogaps showed photocurrent that was higher at 295K than at lower temperatures, while other nanogaps on the same chip and under equivalent conditions showed the opposite. Moreover, if the nanocrystals were illuminated overnight and voltage was applied (hereafter referred to as a *laser voltage treatment*), the low-temperature photocurrent was enhanced, whereas if the nanocrystals were left in darkness overnight and voltage was applied (hereafter referred to as a *dark voltage treatment*), the low-temperature photocurrent was suppressed. If voltage was not applied while the sample was left in darkness overnight, the photocurrent magnitude returned to its initial value. This trend was repeatable over a measurement period of

several months. The photocurrent at 295K followed the same trend as the low-temperature photocurrent in ~75% of devices, but the effect was smaller (~10-30% of the photocurrent change at 78K).

6.2 Relative Photocurrent Ratio

To best quantify the photocurrent increase or decrease with temperature, T, it is convenient to define the relative photocurrent ratio $R = I_{78K}/I_{295K}$, of the low-temperature photocurrent, I_{78K}, and the room-temperature photocurrent, I_{295K}. This is analogous to the relative resistance ratio between the low- and room-temperature resistance in metals, commonly used as a criterion of metal purity; if the photoconduction in nanogaps were Ohmic, resistance would be well defined, and then R would be the same as that defined for metals. Each ratio R was calculated for one cool-down cycle of measurements taken in a single day. The relative photocurrent ratio has two distinguishable regimes: if $R < 1$, this means that the photocurrent increased with T, and if $R > 1$, the photocurrent decreased with T. In the discussion below, I_{78K} and I_{295K} were calculated as averages of photocurrent magnitudes for the maximum electric field applied across the nanogaps, corresponding to voltages -2V and 2V. The following conclusions hold qualitatively for other voltages, and also apply independently of annealing temperature. Examples of nanogaps with $R = I_{78K}/I_{295K}$ smaller or greater than 1 are shown in **Figure 6.1.6**a (R = 2.2) and **Figure 6.1.6**b (R = 0.1). Out of the seventeen nanogaps, fifteen initially showed $R > 1$ and two showed $R < 1$. A histogram of R values for 532 nm illumination and a comparison of R values for both 532 and 650 nm illumination are given in **Figure 6.2.2** and **Figure 6.2.3**. As measurements progressed, illumination history was observed to affect this ratio, so that R could be switched from less than 1 to greater than 1 or vice versa in a single nanogap. A sample table of the change in relative photocurrent ratios after laser and dark voltage treatments is given in Table 1.

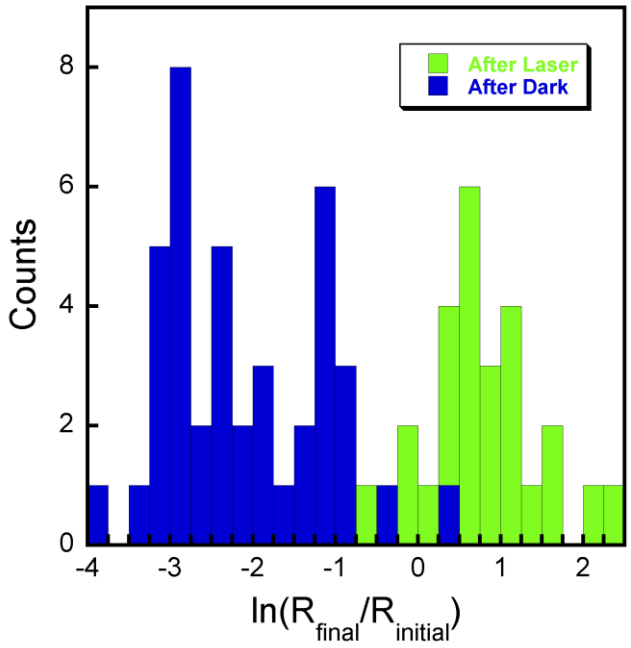

Figure 6.2.1. Histogram of $R_{final}/R_{initial}$ on a logarithmic scale, including laser voltage treatments (green) and dark voltage treatments (blue).

Figure 6.2.1 shows a histogram of the *change* in *R* from $R_{initial}$ to R_{final} from 70 measurements over all devices after laser and dark voltage treatments. A logarithm transformation is used to write the change in *R* on the x-axis as $\ln\left(\frac{R_{final}}{R_{initial}}\right)$. This manner of representing the change in *R* is informative because $\ln\left(\frac{R_{final}}{R_{initial}}\right) = -\ln\left(\frac{R_{initial}}{R_{final}}\right)$, meaning that an increase or decrease of *R* by the same factor is represented on this logarithmic scale symmetrically around zero; $\ln\left(\frac{R_{final}}{R_{initial}}\right) = 0$ means that *R* does not change. There are two distinct distributions in this histogram, showing that device behavior after a laser and dark voltage treatment is clearly separated. The laser voltage treatment increases the ratio by an average factor of 2.2, meaning that $R_{final} > R_{initial}$. The dark voltage treatment decreases the ratio by a factor of 10, meaning that $R_{final} < R_{initial}$.

This effect has also been observed in a large gap with an active area of ~109 μm^2 (~43.6 x 2.5 μm), implying that this effect is independent of device size.

This demonstrated change in ratio *R* with laser or dark voltage treatments shows that the temperature dependence of conductivity is controlled by the measurement protocol. Consequently, all such measurements on nanocrystal arrays must be framed in the context of the sample measurement history in order to be properly interpreted. This consideration may explain apparent discrepancies in the reported temperature dependence of observed photocurrent. [1, 12, 14, 80, 82, 121] Localized charge carriers in the nanogap can measurably affect the temperature dependence of photoconductivity. The manipulation of trap states by optically stimulated emptying or voltage induced populating can then be used to control device performance. [125]

For the initial I-V measurements of the devices taken using a 532 nm laser after several days without measurements, the measured photocurrent ratio *R* was in the approximate range of 1 to 10. **Figure 6.2.2** shows a histogram of *R* values measured for all treatments in nanogap devices illuminated with 532 nm light.

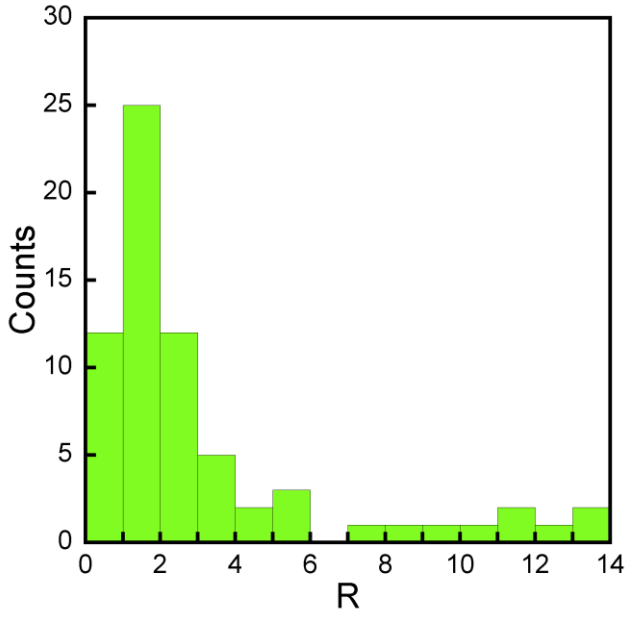

Figure 6.2.2. Distribution of R values for nanogap devices.

Illumination with a 650 nm laser produced photocurrent at room temperature (0.01-2.9 pA, with a mean of 0.36 pA) but lower photocurrent at low temperature (0.01-0.7 pA, with a mean of ~0.17 pA), yielding overall smaller ratios *R* in the range of 0.1 to 2. These two ratio populations are shown in a histogram in **Figure 6.2.3**. The smaller ratio *R* values for 650 nm versus 532 nm excitation can be understood by recalling the change in the absorption peak of these nanocrystals with temperature. At room temperature, the peak is thermally broadened which allows an overlap between the laser excitation and the absorption peak. The peak at 610 nm is thermally narrowed and blueshifted at low temperature because of the temperature dependence of the Stokes shift,[126, 127] which reduces the overlap of the laser excitation and the peak, causing photocurrent to be lower. Higher illumination energy (532 nm) results in larger R, with an average R of 2.8. The average R for the 650 nm excitation is 0.7. The photocurrent from illumination at 980 nm was also measured, but was found to be negligible as expected due to the energy mismatch between the nanocrystal bandgap and the energy of the incident photons.

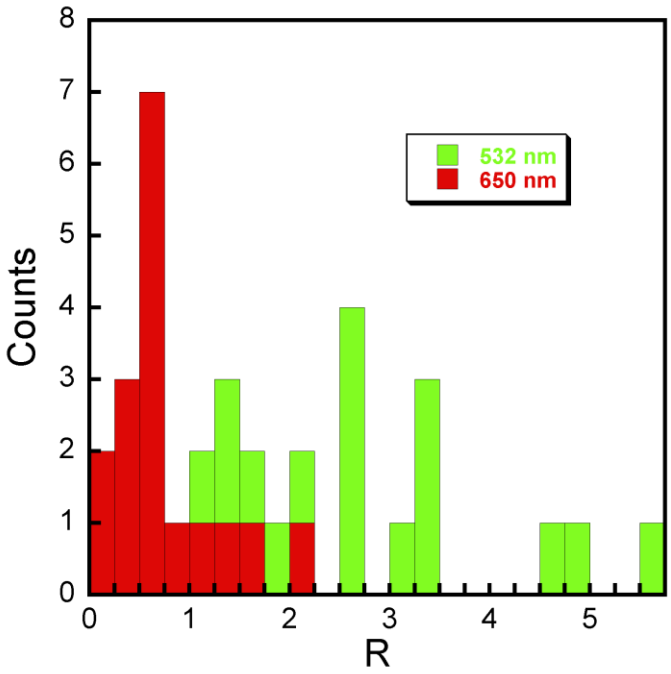

Figure 6.2.3. Histogram of the ratio $R = I_{78K}/I_{295K}$ for two excitation wavelengths.

Gap	*R* after no measurements	*R* after laser voltage treatment	*R* after dark voltage treatment	*R* after laser voltage treatment
5-1	0.38	1.81	0.72	0.94
5-2	2.67	4.44	1.20	1.43
5-3	0.36	1.00	0.33	0.48
5-4	1.63	2.85	0.53	0.75
5-7	1	0.88	0.31	0.59
5-8	0.75	1.56	0.43	0.72
5-9	0.69	1.88	0.23	0.75
5-10	0.85	3.29	0.51	1.27
5-11	0.095	1.06	0.04	0.20

Table 6.1. Relative photocurrent ratios for several nanogap devices illuminated with 650 nm light, increasing or decreasing with different treatments.

Using the laser voltage treatment to increase the relative photocurrent ratio $R = I_{78K}/I_{295K}$, or using the dark voltage treatment to decrease *R*, is a robust and repeatable process. Nanogap devices can be cycled to high and low *R* values many times without the effect losing potency. These devices were measured for several months and continued to demonstrate the same reversible behavior. Table 1 shows the relative photocurrent ratio *R* of several nanogaps, and its changing value after laser or dark voltage treatments. These data were taken with a 650 nm laser.

The temperature dependence of the photocurrent can be repeatedly reversed in *a single nanogap* device to yield a temperature-decreasing or temperature-increasing photocurrent. This is illustrated by a single nanogap in **Figure 6.2.4**, which shows the ratio $R = I_{78K}/I_{295K}$ switching from (a) $R > 1$ when I_{78K} (blue) > I_{295K} (red) to (b) $R < 1$ when I_{78K} (blue) < I_{295K} (red) for all laser intensities used.

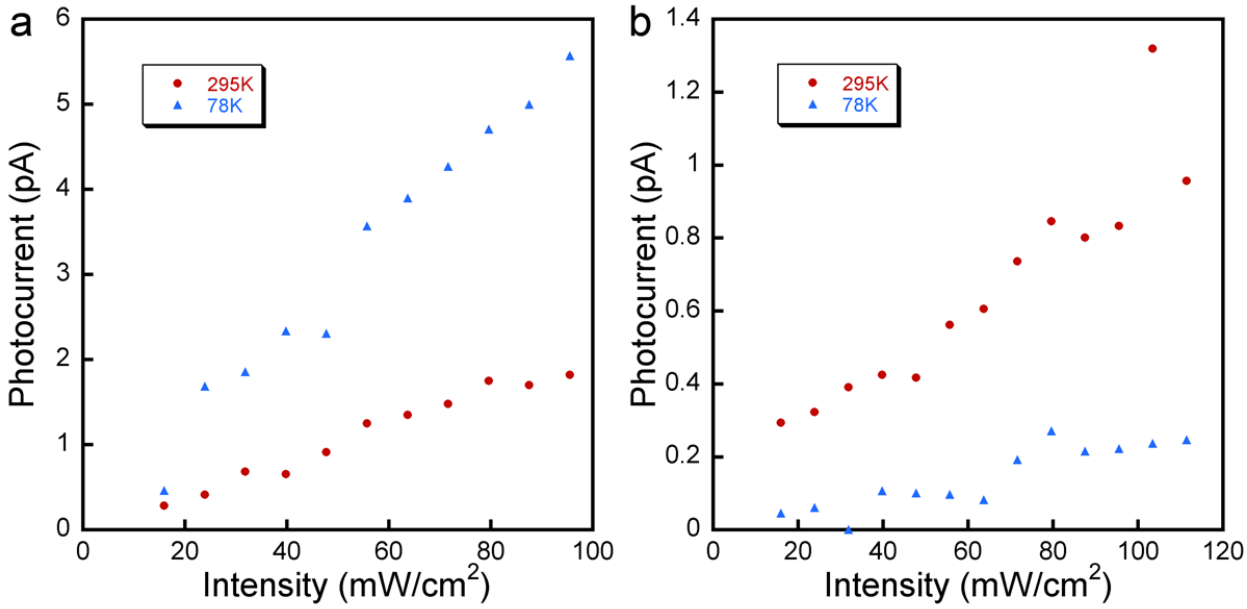

Figure 6.2.4. Photocurrent versus laser intensity (a) before and (b) after a dark voltage treatment.

6.3 Exciton Dynamics: Trap Manipulation

To understand the underlying mechanism, one must first look at the energy levels through which the charge carriers travel. **Figure 6.3.1**a shows energy levels for the electrodes with a single nanocrystal between them; the shortest charge carrier path in these devices includes four nanocrystals. The carrier tunneling between nanocrystals can be lost by recombining with other oppositely charged carriers through radiative or nonradiative recombination, which usually corresponds to free recombination or recombining with trapped carriers at recombination centers, respectively. Radiative recombination is a kind of bimolecular carrier dynamics, because of the two free carrier types involved, whereas non-radiative recombination at a charge trap is called monomolecular. The primary photocurrent in a semiconductor is given by

$$I(E,T) = eFG\,, \tag{6-1}$$

where e is the charge of an electron, F is the exciton generation rate, and G is the number

of free charge carriers created that pass between the electrodes for each photon absorbed, which is also called the photoconductive gain.[13, 14, 16] F is defined by

$$F = \Phi a \eta(E,T),^{14} \tag{6-2}$$

where Φ is the excitation flux, a is the film absorption, and $\eta(E,T)$ is the field-dependent exciton separation efficiency. $\eta(E,T)$ is defined in terms of the relevant rates that affect exciton recombination and transport:

$$\eta(E,T) = \frac{k_E(E,T)}{k_E(E,T) + k_R(T) + k_N(T)}, \tag{6-3}$$

where $k_E(E,T)$ is the field-dependent rate of charge carriers escaping to neighboring nanocrystals or electrodes, $k_R(T)$ is the rate of charge carriers radiatively recombining, and $k_N(T)$ is the rate of charge carriers nonradiatively recombining.[16]

The tunable temperature dependence of the observed photocurrent can be explained by the relative magnitudes of the rates $k_R(T)$, $k_N(T)$, and $k_E(E,T)$ involved, shown in **Figure 6.3.1**a, and their temperature dependences. The contribution from both radiative recombination and the number of traps is constant over these measurements and fixed for a given sample, but the contribution from trap states depends on trap population, which can be adjusted by laser and dark voltage treatments.

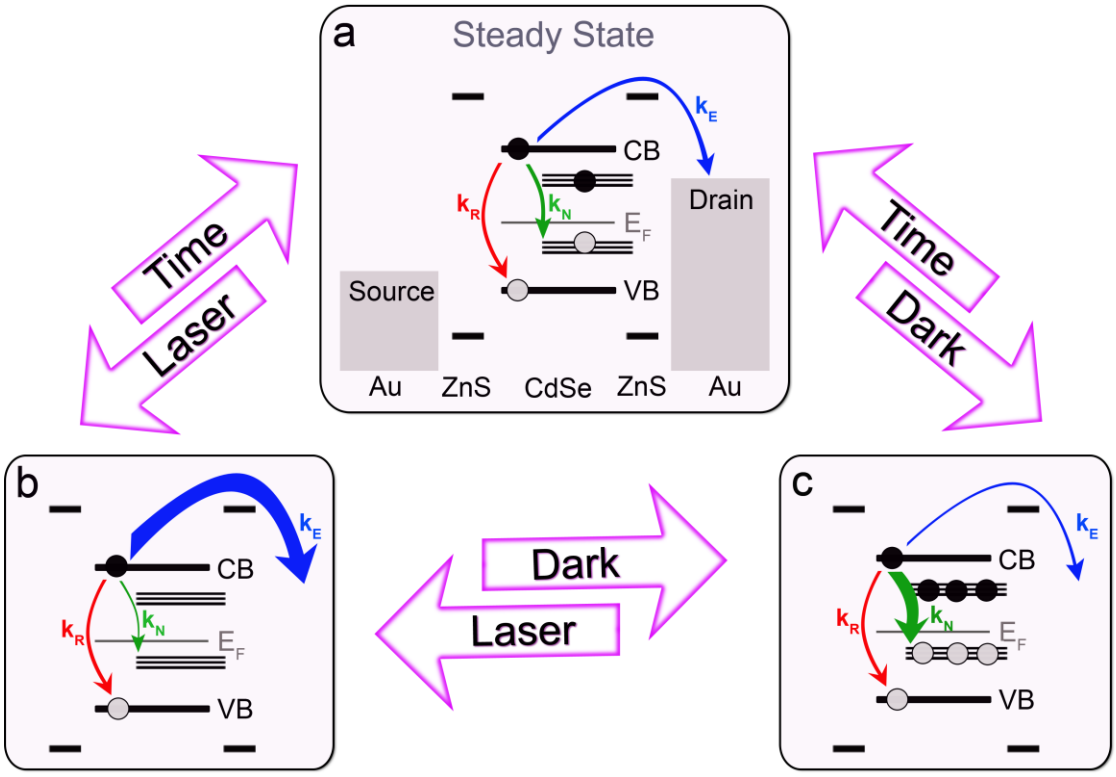

Figure 6.3.1. Recombination and transport processes for charge carriers in a nanocrystal circuit. These processes are affected by the laser and dark voltage treatments.

The energy level diagram for a steady state CdSe/ZnS core-shell nanocrystal between two gold electrodes are shown in **Figure 6.3.1**. Trap states above the Fermi energy, E_F, act as electron traps, whereas trap states below E_F act as hole traps. An exciton is created by illumination of the sample, and it can either recombine radiatively with rate k_R, recombine nonradiatively via the trap states with rate k_N, or tunnel away from the nanocrystal at a rate k_E related to the applied field E. Before any treatment, the system has a number of occupied trap states that is defined as the steady state, as in **Figure 6.3.1**a.

The laser voltage treatment excited trapped carriers to the conduction band where they tunnel out of the nanocrystal, causing traps that are occupied in steady state to be emptied, as in **Figure 6.3.1**b; this effect of optically stimulated trap emptying in nanogaps is similar to an analogous phenomenon well documented in the semiconductor

literature.[16] The laser voltage treatment eliminates many charge carriers, even in energetically favorable traps, and fewer charge carriers recombine with trapped charges. The low charge trap population enhances k_E processes and suppresses k_N processes. Photocurrent increases temporarily, but over a few days of waiting time, the trap occupancy returns to its steady state value, as energetically favorable traps are repopulated, causing photocurrent to return to a steady state value as well.

Conversely, the dark voltage treatment repeatedly sweeps the voltage, trapping carriers without providing the optically harvested energy to escape, as in **Figure 6.3.1**c. Thus, after dark voltage treatment even energetically unfavorable traps are populated; the populated traps capture more carriers and cause them to recombine, temporarily decreasing photocurrent. The high charge trap population suppresses k_E processes and enhances k_N processes. Over a few days of waiting time the trap occupancy returns to its steady state value, as charge carriers in some traps escape using thermal energy. This returns k_E and k_N processes to their steady state values, causing photocurrent to return to a steady state value as well.

To summarize, by applying the laser and dark voltage treatments, the trap population is modified, which allows tuning of the photocurrent response; this has a greater effect at low temperature because traps can be emptied using the larger thermal energy at room temperature. Relevant processes for photogenerated electrons in the conduction band are shown in detail in **Figure 6.3.1**. Hole processes are affected by the treatments in the same way, but are not shown. The photocurrent temperature dependence can be tuned using these effects, and the resultant adjustability is robust even when other variables are changed.

The emptying and filling of traps via light and electric fields can explain the controlled variation in photoconductivity temperature dependence that have been measured thus far. But whether this is an accurate model of physical reality can also be probed by examining the intensity, wavelength, and time behavior of photoconductivity as it responds to laser and dark voltage treatments. Those measurements are described in the following sections.

6.4 Illumination Intensity Measurements

Measuring photocurrent dependence on laser intensity at a fixed wavelength supports the trap-based model in explaining the adjustable photocurrent dependence on temperature. While initial photoconductivity measurements were taken with a fixed illumination intensity of ~65 mW/cm^2, intensity was later varied between 1.6 to 120 mW/cm2 at both 78K and 295K. As illumination intensity was varied, the current was measured at a constant voltage of 1V, which corresponds to $3 \cdot 10^5$ V/cm. The laser and dark voltage treatments had little effect on the intensity dependence at 295K, but had a greater effect at 78K. The treatments can result in an inversion of the temperature dependence of the photocurrent for a wide range of intensities, see **Figure 6.2.4**.

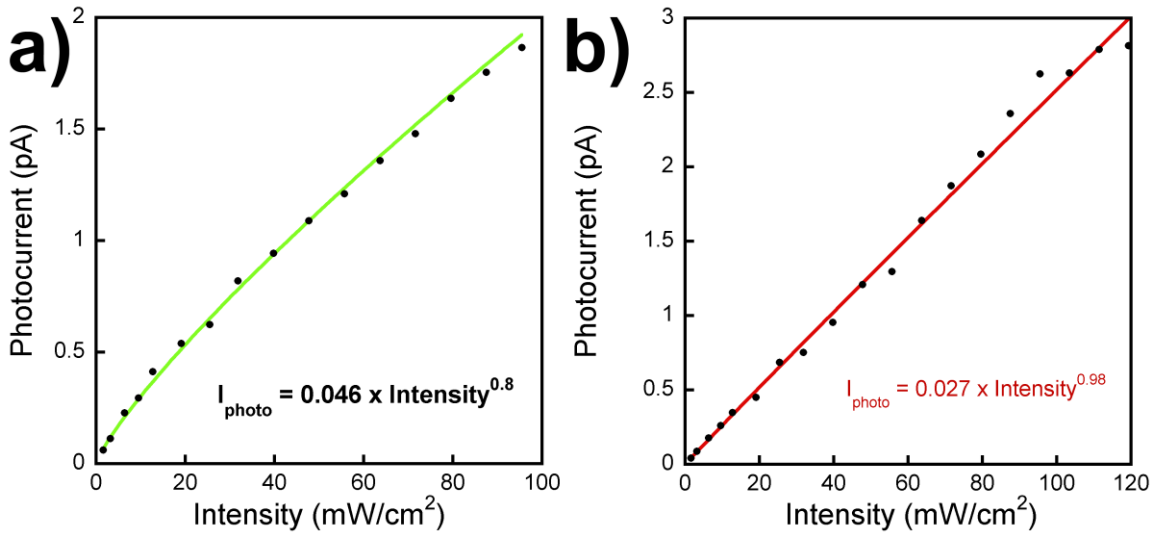

Figure 6.4.1. Photocurrent versus illumination intensity at (a) 295K and (b) 77K.

Empirically, the intensity dependence of the photocurrent always follows a power law,

$$I_{photo} \propto Intensity^{\alpha}. \qquad (6\text{-}4)$$

For 532 nm laser excitation measured at an electric field strength of $3 \cdot 10^7$ V/m and a temperature of 295K, $\alpha = 0.82 \pm 0.02$, as shown in **Figure 6.4.1**a. This is consistent with

previous room temperature measurements on large arrays of core-shell nanocrystals yielding the same α value.[14] Intensity dependence of the photocurrent at 78K gives α = 0.96 ± 0.02 as shown in **Figure 6.4.1**b. This value is in agreement with the linear response at low temperature reported in the literature.[82] The specific value of α helps reveal the type of carrier dynamics present. If $\alpha = 1$ then the carrier dynamics are monomolecular, because the high number of trapped carriers increases the importance of nonradiative recombination. Nonlinear values of α correspond with larger numbers of free carriers, and thus bimolecular carrier dynamics.

In order to understand the power law fit, it is instructive to examine the rate equation for *n*, the density of free electrons,

$$\frac{dn}{dt} = F - C(n + n_{trap})n \,.^{13,\,16} \tag{6-5}$$

Here, *C* is the probability of an electron to be captured, *n* is the density of free electrons, and n_{trap} is the density of trapped electrons. $n + n_{trap}$ represents the density of holes in the system which can recombine with free electrons, assuming a neutral nanocrystal. For a steady state system, $\frac{dn}{dt} = 0$ and *F* can be rewritten:

$$F \propto (n_{trap} + n)n \,. \tag{6-6}$$

Substituting equation (6-2) into equation (6-5) yields

$$\Phi \propto \frac{(n_{trap} + n)n}{a\eta} \,. \tag{6-7}$$

There are two interesting cases of this equation that can be examined: the case where there are more trapped carriers than free carriers, $n_{trap} >> n$, and the case where there are more free carriers than trapped carriers, $n_{trap} << n$. Solving for excitation flux as a function of free carriers yields

$$\Phi \propto \begin{Bmatrix} n^2 & n_{trap} << n \\ n & n_{trap} >> n \end{Bmatrix} . \tag{6-8}$$

Since $n \propto I_{photo}$, this relation can be restated as a photocurrent dependency on excitation flux:

$$I_{photo} \propto \begin{cases} \Phi^{0.5} & n_{trap} << n \\ \Phi & n_{trap} >> n \end{cases} \quad (6\text{-}9)$$

This is a more specific theoretically justified case of the general power law dependence given in equation (6-4). $\alpha = 1$ implies monomolecular (first-order) carrier dynamics, whereas $\alpha = 0.5$ implies bimolecular (second-order) carrier dynamics.[16] First-order kinetics contribute more when the material has many recombination centers, such as deep hole traps, and when the material has a lower free electron concentration than in the bulk, as is the case in nanocrystals where the presence of surface traps is likely.[82] Contributions of surface and deep traps, which are only partially passivated by the shell and ligands, can cause a deviation of the photocurrent dependence on intensity from the expected dependence in a bulk solid, where bimolecular recombination would dominate giving $\alpha = 0.5$. The measured exponent $\alpha = 0.8$ at room temperature implies that a combination of first and second order recombination dynamics is observed. However, at low temperature, the exponent $\alpha = 1$ implies that first-order recombination dynamics dominate. The variation in the fitting exponent sheds light on the difference of recombination center density at each temperature, which supports the low-temperature trap emptying model shown in **Figure 6.3.1** and encompasses reported intensity dependence.[14, 16, 82]

6.5 Excitation and Treatment Wavelength Measurements

Varying the wavelength of light used in photocurrent measurements is a useful tool, because using light at different energies allows us to probe different energy levels and different exciton states of the nanocrystal. If the wavelength of light used in the actual photocurrent measurement is changed, the nanocrystal bandgap should affect which wavelengths yield the largest photocurrents. If the wavelength of light used in laser voltage treatments is changed, varying results should be observed as trapped carriers are excited to different conduction band states.

Examples of I-V sweeps at illumination wavelengths of 473 nm (blue), 532 nm (green), and 650 nm (red) and the positions of these laser excitation wavelengths on the absorption vs. wavelength curve are shown in **Figure 6.5.1**. The difference in measured

photocurrent values is due to the variation in absorptivity of nanocrystals with wavelength, as shown in the inset where absorption and emission intensities are plotted versus wavelength for CdSe/ZnS nanocrystals in solution. The blue, green, and red circles indicate the positions of the excitation wavelengths with respect to the absorption curve. The variation in absorptivity is itself a result of the quantized energy levels of the nanocrystals. The first absorption peak corresponds to the transition between the highest occupied molecular orbital and the lowest unoccupied molecular orbital, the HOMO-LUMO or band gap transition, which corresponds to the energy difference between the $1S_{3/2}$ and $1S_e$ states.[41] As the energy of the incident photons increases above this transition energy, the measured photocurrent increases, whereas photocurrent is minimal for photons whose energy is below the nanocrystal band gap. The 650 nm I-V curve below is very close to the nanocrystal band gap energy, thus the measured photocurrent is small compared to that measured with higher energy (lower wavelength) photons.

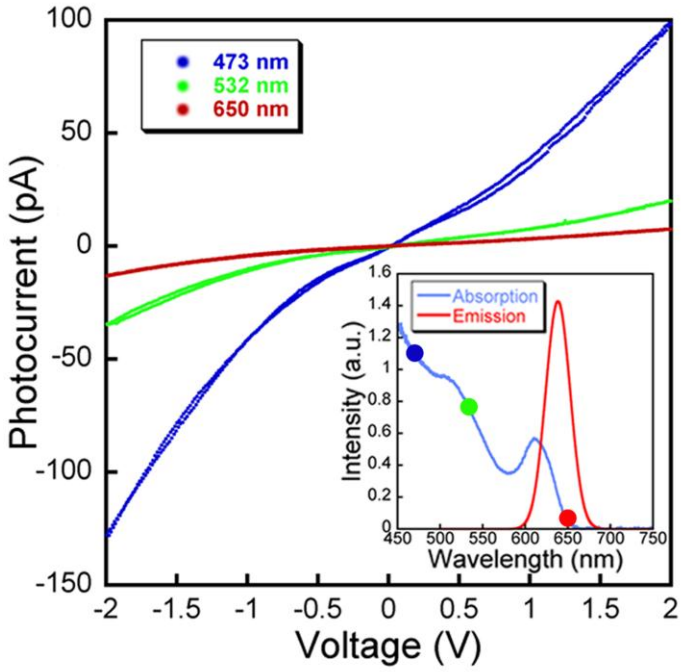

Figure 6.5.1. Photocurrent vs. voltage curves for 650 nm, 532 nm, and 473 nm laser excitations.

Figure 6.5.2 shows the energy level diagram for a nanocrystal under illumination

at different wavelengths. *All* photocurrent measurements were performed using 532 nm few-mW green laser excitation. To investigate the effects of sample history on photoconductivity samples were additionally exposed to three different excitations (532 nm, 650 nm and 980 nm) *prior* to photocurrent measurements, as part of the laser voltage treatment. This places the treatment illumination wavelength below or above the nanocrystal band gap, which probes the levels of charge traps inside the band gap.

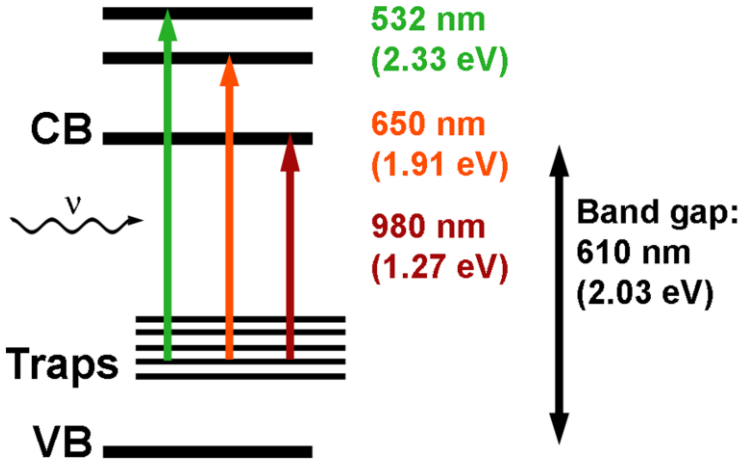

Figure 6.5.2. Diagram showing photoexcitation of charge carriers from trap levels at various wavelengths of light.

The data in **Figure 6.1.5** were obtained using the same excitation wavelength prior to the measurement and for the actual I-V measurement, a 532 nm laser whose energy (2.33 eV) is higher than the band gap energy of the nanocrystals (2.03 eV). In addition, light with energy smaller than the band gap, 650 nm (1.91 eV) and 980 nm (1.27 eV), was used to illuminate devices *prior* to I-V measurements with 532 nm light. Devices were illuminated for 16 hours for a laser voltage treatment, and this measurement was repeated 3-5 times for each wavelength. From the data taken on three electrode gaps, larger average $R_{final}/R_{initial}$ was observed when sub-band gap illumination was used: 4.9±1.0 and 3.0±1.0 for 980 and 650 nm excitations respectively, compared to 1.6±1.0 for 532 nm excitation.[128] Although the absorption coefficient for nanocrystals

decreases with decreasing illumination energy,[129], these measurements suggest that lower energy photons are more efficient at exciting carriers out of charge traps.

The effect of different excitation energies used prior to measuring photocurrents with 532 nm excitation can be understood from the diagram in **Figure 6.5.2**. The conduction band (CB), valence band (VB), and trap levels are marked. Photocurrent is measured only with 532 nm and the other wavelengths are used to illuminate samples before the I-V measurement with 532 nm. The energy required to excite carriers from trap states into the conduction band is less than the band gap energy, implying that sub-band gap illumination of nanocrystals can affect the overall charge state of the sample by exciting carriers out of the traps. This in turn, changes the photocurrent measured *later* with 532 nm excitation. Therefore, sub-band gap illumination of devices affects the photoconductivity, even though sub-band gap excitation is not energetic enough to result in measurable photocurrent. Photocurrent lifetime wavelength dependence has also been studied using current noise spectroscopy, for energies below and above the band gap.[59, 130, 131] Varying the illumination wavelength alters the level of noise from generation-recombination and trapping-detrapping. [131] Wavelength dependence was found to be strong in the low frequency range of the photocurrent noise power spectra.[59, 131] This behavior was attributed to long trapping-detrapping times similar to those observed here.

These results also indicate that sub-band gap excitation is more efficient for charge detrapping than excitations above the band gap. Different wavelengths of light excite trapped carriers into different band gap edge states, as depicted in **Figure 6.5.2**. Charge carriers in higher states have a larger number of relaxation pathways available than those in the lowest conduction state. For example, they can relax into lower states, into trap states, or travel out of the nanocrystal via field-driven transport. It is possible that access to higher states could reduce the trap emptying efficiency, decreasing the memory effect. High energy excitation has also been shown to create a charge-separated complex that is slow to decay. [83] This conceptually supports the result that sub-band gap energy photons are preferable for trap manipulation in nanocrystal semiconducting films.[128]

6.6 *Photocurrent Behavior versus Treatment Time*

The effect of sample history on the photocurrent can be characterized further by studying how the photocurrent temperature dependence is affected by the time elapsed between two consecutive measurements of R during which the sample was exposed to electric fields and light. These measurements probe the timescales over which traps can be populated and depopulated, and their overall effect on photoconductivity. The different measurement histories can modify photocurrent by changing the population of charge traps in the nanocrystals, which may affect the rate of non-radiative recombination.[125] Laser voltage treatment reduces the trap population, temporarily lowering non-radiative recombination, which raises low-temperature photocurrent. Dark voltage treatment increases the trap population, temporarily raising non-radiative recombination, which lowers low-temperature photocurrent. Thus, when trap population is affected by the illumination and electric field history, the value of $R_{final}/R_{initial}$ indicates how photocurrent temperature dependence has changed.

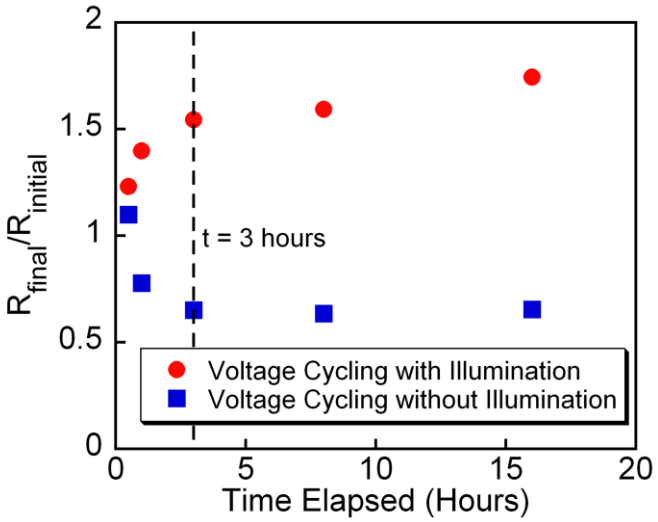

Figure 6.6.1. $R_{final}/R_{initial}$ as a function of time for laser and dark voltage treatments.

Figure 6.6.1 shows $R_{final}/R_{initial}$ vs. time elapsed when voltage was cycled between the I-V measurements of $R_{initial}$ and R_{final}. When the device was in the dark (blue squares), $R_{final}/R_{initial}$ decreased with time, and when it was under illumination (green circles),

$R_{final}/R_{initial}$ increased with time; for both cases, $R_{final}/R_{initial}$ changes rapidly in the first few minutes and hours after exposing devices to electric fields and light, or electric fields alone. But over time the rate of change decreases, and after three hours the subsequent change is less than 5%. These results indicate that the change in trap population slows asymptotically, initially proceeding quickly but slowing with time as the most energetically accessible trapped carriers are excited and transported out of the nanocrystal. The majority of the effect on photoconductivity takes place in the first three hours (dashed line). Voltage cycling beyond the initial few hours does not appear to change $R_{final}/R_{initial}$ significantly, meaning that it does not change the photocurrent or the trap state population significantly. The data in **Figure 6.6.1** are for one 230 nm gap. Other gaps measured behaved similarly. Each point is averaged over 5-15 measurement cycles and has an error of ±0.3. The *R* values for these data were in the range 0.25 to 15, with ~60% lying between 1 and 3.

This result implies that traps can be populated and depopulated over approximately three hours and that more time does not seem to significantly affect the number of trapped carriers.[128] Previously, carrier processes in nanocrystals that happen over long time scales have been observed, such as hour-scale changes in photoluminescence lifetime of nanocrystals in solution,[132] and defect emission from nanocrystals for over an hour after initial illumination.[133] Photocurrent lifetime wavelength dependence has also been studied using current noise spectroscopy in CdS/CdSe/PbSe polycrystals, for energies below and above the band gap. Varying the illumination wavelength alters the level of noise from generation-recombination and trapping-detrapping. Wavelength dependence was found to be strong in the low frequency range of the photocurrent noise power spectra. [134] This behavior was attributed to long trapping-detrapping times similar to those observed here.

These examples of slow recombination processes support the observation that emptying or filling traps in an insulating sample can take up to three hours for devices at this scale.[128]

6.7 Trap Population Manipulation Affects Photoconductivity

Studies on nanogap devices with annealed CdSe/ZnS core-shell nanocrystals in the gap region have shown that the photoconductivity temperature dependence of CdSe/ZnS nanocrystal arrays depends on device exposure to light and electric fields, i.e. the illumination history of the device. Recent laser illumination causes optically induced trap emptying and higher low-temperature photocurrent, while recent voltage cycling in the dark causes electric field induced trap population and lower low-temperature photocurrent. The effects of laser and dark voltage treatments exhibit saturation after a few hours. Interestingly, while sub-band gap illumination does not yield measurable photocurrents, it affects the photoconductivity upon subsequent band gap illumination. This can be understood by the presence of charge traps that are emptied or filled by applying electric fields and light, where traps are most easily emptied with sub-band gap illumination. These results resolve existing discrepancies in the literature, demonstrating the difficulty in defining temperature dependence of photoconductivity for semiconducting nanocrystal systems. The controllable photocurrent temperature dependence is robust over multiple wavelengths and intensities of laser excitation and suggest a route towards achieving maximal photodetector response at a specific temperature. This approach of tuning the photocurrent response via trap population can be useful for nanocrystal device applications, such as sensors, solar cells, and light emitters, as well as aiding in the study of carrier dynamics and energy levels in nanoscale materials. Tuning trap populations is also potentially crucial for nanocrystals that have strong nonradiative processes or a significant number of interband states, such as doped semiconducting nanocrystals.[135, 136] These factors are essential for the optimal and robust operation of optoelectronic devices based on semiconductor nanocrystals. The result is a unification of previous and current measurements of photoconductivity under a relatively simple theory, resolving contradictions in the literature and pointing the way toward useable applications.

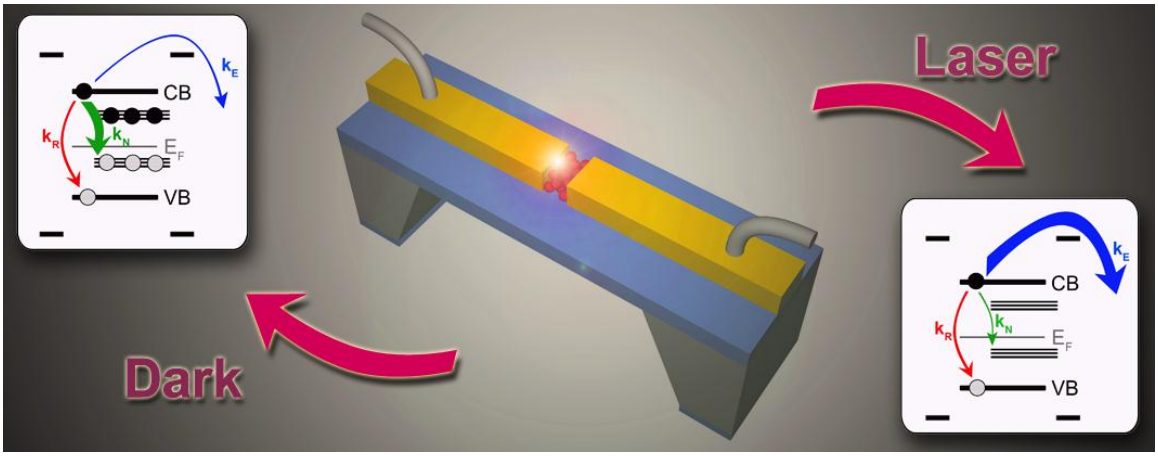

Figure 6.7.1. Device illustration and exciton dynamics for observed photocurrent behavior.

7 Coupling Nanocrystals to Graphene

Summary

Although the optical properties of semiconducting nanocrystals are impressive, the poor charge conduction of nanocrystal arrays has led many researchers to look for device design tricks that will preserve the desirable optical properties while improving charge separation and transfer. Alternating monolayers of CdSe and CdTe nanocrystals has been shown to improve exciton splitting in photodevices.[137] Thin layers of PbS nanocrystals have also been fully depleted in a TiO_2 heterojunction, improving transport of charges out of the PbS layer.[138] Sintering can also improve charge collection efficiency, but sintered devices end up with a much larger grain size than was present in the initial colloidal nanocrystals.[139]

Another approach is to couple nanocrystals in a two-electrode structure to a better electrical conductor. Graphene, a two-dimensional crystal of hexagonally bonded carbon, is an interesting choice as a nanocrystal substrate. While the mechanical properties of graphene have been widely studied, such as its high tensile strength and impermeability, [140] it is the electrical properties of graphene, such as its high conductivity and the dangling bonds perpendicular to the plane of the graphene, which make graphene a viable candidate for strong electronic coupling.[141] Graphene is also currently under investigation for optoelectronic applications such as solar cells, lasers, and photodetectors.[142-146]

An ideal graphene/nanocrystal device would possess electrical coupling strong enough that carriers can easily transfer to the graphene and be collected at metal electrodes. However, if quantum confinement of charge carriers in the nanocrystal is compromised, or if both species of carriers are transferred to graphene causing recombination to occur there, measured current may be greatly diminished. Experiments in creating optoelectronic devices where semiconducting nanocrystals are supported by a graphene substrate are described in the following sections.

7.1 Fluorescence Quenching

Before undertaking any lengthy device fabrication, it is desirable to probe whether drop-cast nanocrystal films can electronically couple to graphene. The fluorescent behavior of nanocrystals on a substrate can provide such a probe. On an inert substrate, such as optically smooth mica, a film of drop-cast nanocrystals will fluoresce under illumination from a bright enough light source with a wavelength corresponding to a hoton energy above the nanocrystal band gap. The fluorescence is due to carriers which are excited by the incident photons, decay to the band gap edge states, and then radiatively recombine, emitting a photon whose energy is equal to the band gap energy. If the nanocrystals are placed on a substrate to which carriers can be transferred, the fluorescence is lowered compared to the fluorescence on a neutral substrate. This phenomenon is called quenching, and it is also observed in solution for nanocrystals which have coupled to materials.

To experimentally test the electronic coupling between semiconducting nanocrystals and graphene, we prepared two substrates: bare mica, and mica covered by a few-layer graphene sample. The graphene was grown by chemical vapor deposition, using methane flow in a tube furnace on a heated copper foil.[147, 148] Both the mica substrates and the mica/graphene substrates were tested for fluorescence, then CdSe/ZnS nanocrystals from NN Labs with emission at 620 nm were drop-cast and the fluorescence measured again. The mica/graphene/nanocrystal sample was then annealed in a glovebox at 300ºC for several hours, and its fluorescence was measured a final time.

Fluorescence measurements were performed in air at room temperature, with the sample imaged in a Nikon Eclipse 80i fluorescence microscope. The sample was illuminated using a 488 nm laser at 3 mW, and the emission was sent through a 620 ± 25 nm filter before being collected. Fluorescence was measured at 7-10 spots with similar nanocrystal coverage, and the results were then averaged to give a fluorescence magnitude for each sample. A sample fluorescence image is shown in **Figure 7.1.1**, and averaged data for several samples is shown in **Table 7.1**. The nonuniformity in the fluorescence image is most likely due to nonuniformity in the nanocrystal film, which is why averaging over the beam area was used.

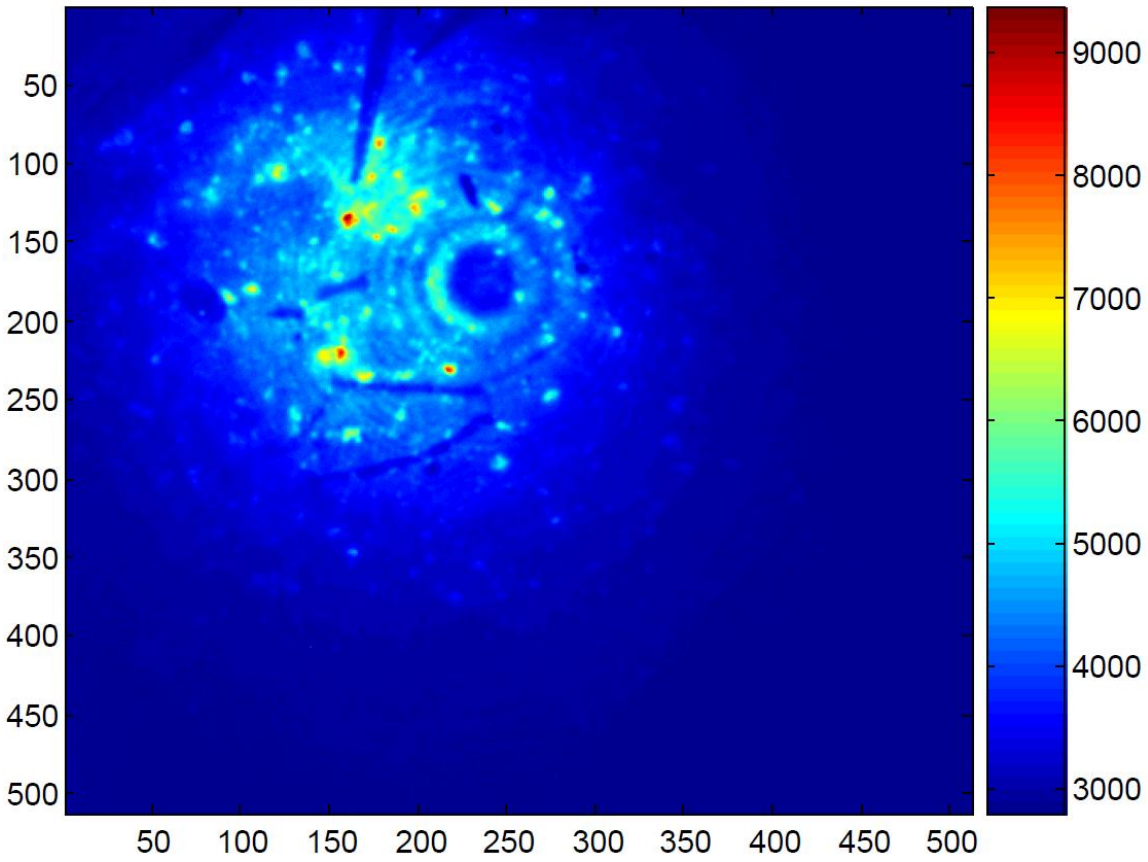

Figure 7.1.1. Sample fluorescence image of nanocrystal film on graphene.

Substrate/Sample Material	Mean fluorescence (A.U.)
Mica	0
Mica/graphene	0
Mica/nanocrystals	1.18×10^{4}
Mica/graphene/nanocrystals	2.9×10^{3}
Annealed Mica/graphene/nanocrystals	2.3×10^{2}

Table 7.1. Mean fluorescence for mica/graphene/nanocrystal samples.

These data indicate that the nanocrystals do couple electronically to the graphene,

quenching fluorescence emission compared to the same nanocrystals on mica. The graphene/nanocrystal sample's fluorescence is quenched by a factor of four compared to the nanocrystals on mica, and annealing the graphene/nanocrystal sample causes another factor of ten quenching. Thus the annealed graphene/nanocrystal sample has forty times less fluorescence than the unannealed nanocrystals on mica. Thermal annealing enhances the effect, as would be expected due to the removal of the ligand.

These rough results also correspond with several reported results in the literature, measuring fluorescence quenching for isolated CdSe nanocrystals on graphene due to Förster energy transfer,[149] ZnO nanoparticles on a graphene oxide substrate,[150] and CdTe nanocrystals on graphene oxide in solution.[151]

7.2 Absorption and Quantum Confinement

Although the fluorescence data shown above indicate that radiative recombination has decreased, the nature of the electrical coupling is still unclear. If the barrier between the nanocrystal interior and the graphene is low enough, the quantum confinement of the nanocrystals may be destroyed, which would modify their optical properties such as absorption spectra.

The optical absorption for a single layer of graphene has been calculated in previous work to be 2.3% across the visible spectrum.[152, 153] For few-layer graphene, the absorption is expected to scale linearly with the number of layers. Adding nanocrystals to graphene should superimpose their absorption spectra, as discussed in section 2.3, onto that of graphene, assuming no loss in quantum confinement of the nanocrystals.

The light source for the absorption setup is an Ocean Optics LS-1 tungsten halogen lamp. The absorption signal from the sample is filtered through one of several filters followed by a Trivista triple spectrometer to provide wavelength selection. The resulting signals for each filter are then stitched together to create a final spectrum across the visible wavelengths. In **Figure 7.2.1**, absorption spectra are shown for a film of nanocrystals drop-cast on a glass microscope slide, and for a film of nanocrystals drop-cast on graphene on a glass microscope slide which has been thermally annealed at 300˚C.

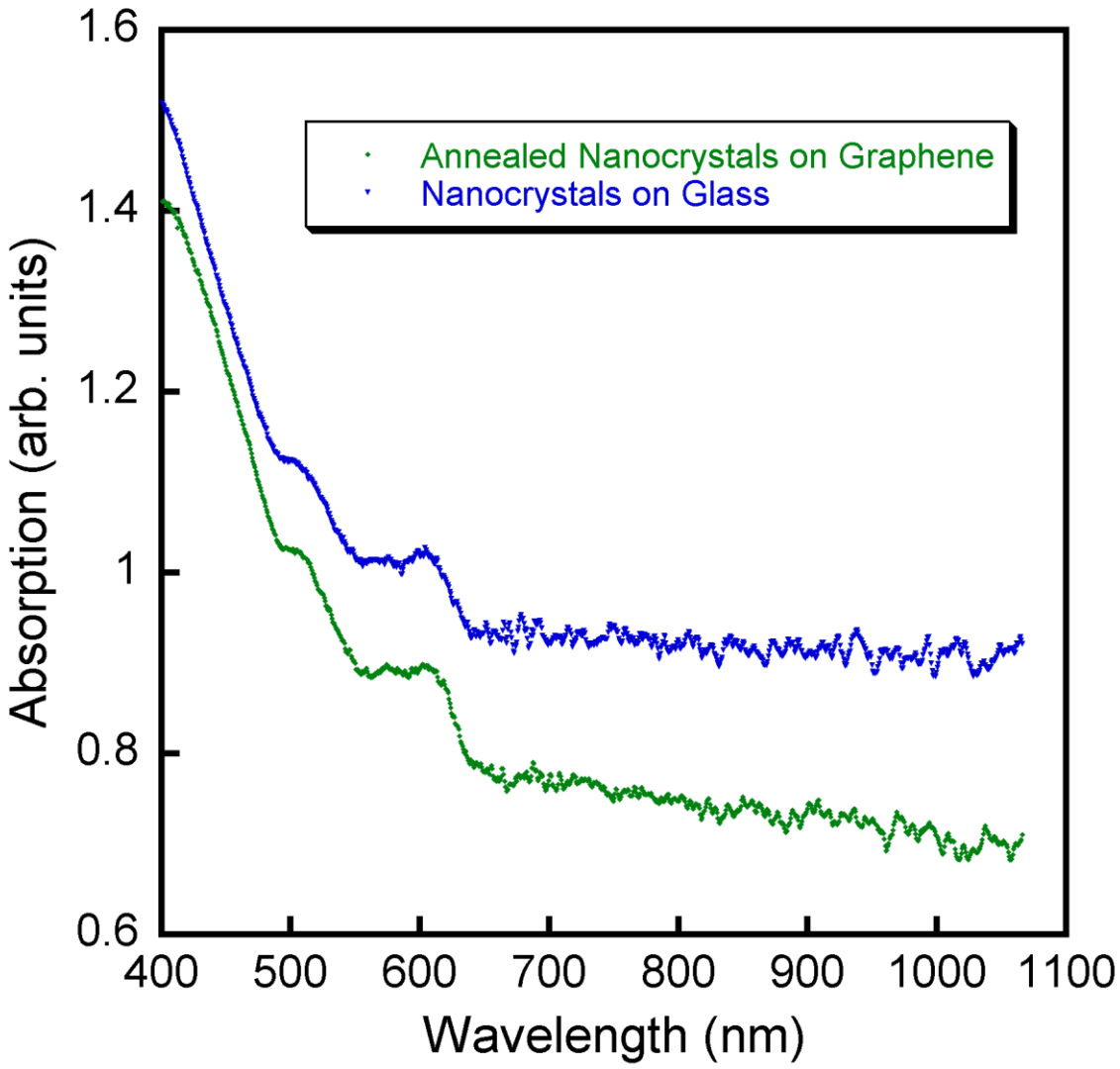

Figure 7.2.1. Absorption of nanocrystals on glass, and annealed nanocrystals on graphene.

Characteristic nanocrystal absorption peaks are visible in the annealed nanocrystal/graphene spectra above. The peaks are somewhat broadened and flattened compared to the peaks for nanocrystals on glass. Broadening and flattening of peaks has also been observed for nanocrystals which have been annealed,[12] so the same process in the samples with graphene is likely a result of small improvements to the electrical coupling between nanocrystals. The presence of the peaks implies that quantum

confinement has not been significantly compromised, because the peaks correspond to energy level transitions determined by the size.

7.3 Graphene Nanoribbon Device

The next step, after the fluorescence measurements showing that nanocrystals can electrically couple to graphene and the absorption measurements showing that quantum confinement of carriers in nanocrystals on graphene is not compromised, is to create a device with an active area of nanocrystals on a graphene substrate. These experiments follow in the footsteps of several recent developments in the literature. Hybrids of graphene oxide and silver nanoparticles have been proposed as effective substrates for Raman spectroscopy.[154] A solar cell has been demonstrated in the literature by combining CdSe nanocrystals and graphene oxide in solution, then integrating the composite into an electrolyte cell with a sandwich geometry.[155]

Graphene grown by chemical vapor deposition was transferred to a SiN substrate, where spin on glass (hydrogen silsesquioxane) was used as a lithographic resist. Two gold electrodes were defined using electron beam lithography and thermally evaporated on top of the graphene, giving very good electrical contact between the electrodes and the graphene. A nanoribbon of graphene is also lithographically defined, 100 nm wide and 500 nm long, which connects the two electrodes. The remaining spin on glass is removed using a dilution of hydrofluoric acid. A schematic of the electrodes and nanoribbon is shown in **Figure 7.3.1**.

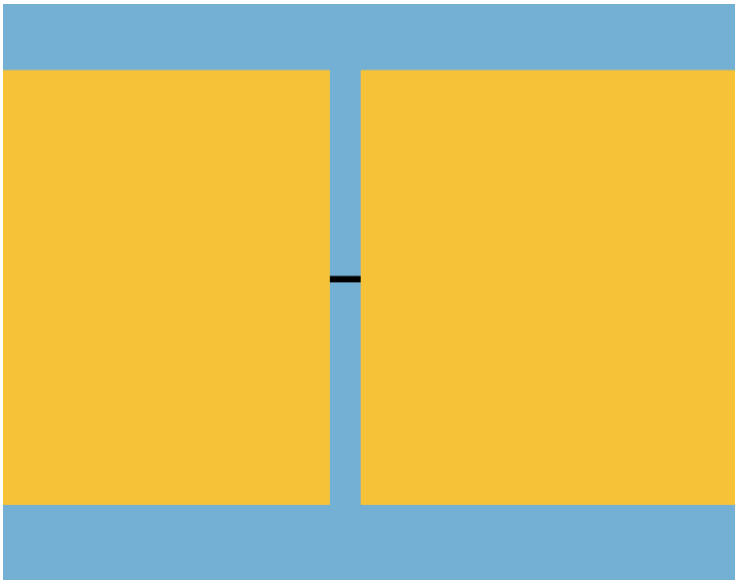

Figure 7.3.1. Schematic of gold electrodes and graphene nanoribbon.

I-V response of the graphene devices is measured before nanocrystal deposition, showing that the nanoribbons act as effective resistors. A representative I-V curve is displayed in **Figure 7.3.2**.

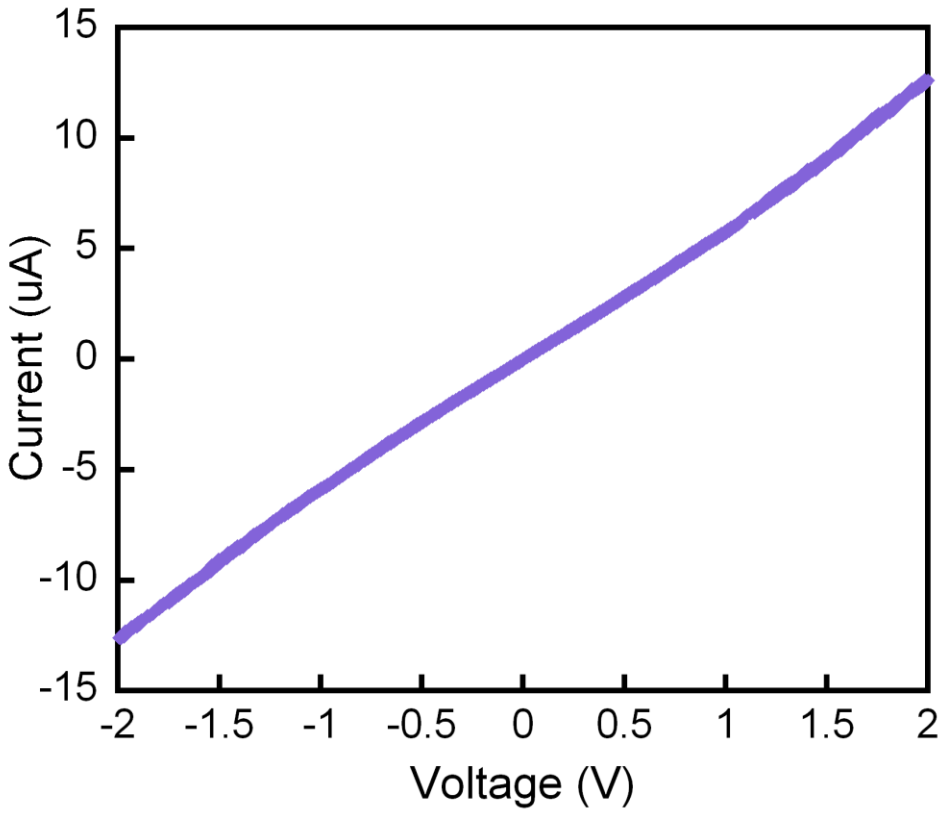

Figure 7.3.2. I-V curve for bare graphene nanoribbon.

The next step for this work is to drop-cast CdSe/ZnS nanocrystals from NN Labs with emission at 620 nm onto the devices and measure photocurrent, which is expected to be a slight enhancement of signal. The fluorescence and absorption measurements described suggest that this will be a promising route forward for coupled nanocrystal devices.

8 Conclusions

Having examined many aspects of devices made from semiconducting nanocrystal films—dielectric conduction, charge defects, device memory, coupling to metal structures and graphene—one can ask where to go from here. In order to take advantage of the optical properties of nanocrystals, it is necessary to find a way to cope with their idiosyncratic electronic properties. The electronic behavior of nanocrystals, though sometimes inconvenient for straightforward incorporation into devices, proves endlessly fascinating. While some qualitative ideas from bulk semiconductors apply, the quantum nature of nanocrystals whose size is below the Bohr exciton limit requires a new approach. Designing devices that utilize size-dependent optical absorption, plasmon resonances of nanoscale metals, two-dimensional carbon sheets, manipulation of electronic traps, and hopping conduction between semiconducting nanocrystals, and then trying to understand the physics of these systems and combine them into a useful structure, requires mental flexibility. This is not "thinking outside the box"; if anything is clear, it is that there is no box.

Looking forward, it seems likely that the processing methods and device geometries which move charge through a monolayer or a few layers of nanocrystals will be the most useful commercially. Defect states, long minimized through fabrication processes in bulk semiconductors, are a fact of life in nanocrystals due to the large fraction of surface atoms. Therefore, control of defects, rather than the elimination thereof, must be the strategy to optimize device performance. The optical properties of nanocrystals are unprecedented and therefore of great interest; but, to use the electrical properties of nanocrystals, it is clear that the circuits and devices which have been shaped by our enthusiastic embrace of silicon may not be the same devices in which nanocrystals shine. Nanocrystal electronics must take advantage of the optoelectronic coupling and the unique conduction mode of nanocrystals, and the most successful nanocrystal circuits

likely require radical redesign from their silicon incarnations.

And what sort of device will use nanocrystals to finally demonstrate an optimal application of their properties? While many optoelectronic devices may seem to be frontrunners, there is an idea worth keeping in mind, stated most eloquently by Herbert Kroemer in his Nobel lecture:

> "The principal applications of any sufficiently new and innovative technology always have been—and will continue to be—applications created by that technology."[156]

The most useful application for nanocrystals may not be an application that exists at all currently. As their underlying physics is revealed, and as more is learned about how they act in ensembles and electronic devices, the scientific community moves closer to that exciting moment of discovery.

Bibliography

1. D. S. Ginger and N. C. Greenham, *Charge injection and transport in films of CdSe nanocrystals.* Journal of Applied Physics, 2000. 87(3): p. 1361-1368.

2. M. Hegg and L. Y. Lin, *Near-field photodetection with high spatial resolution by nanocrystal quantum dots.* Optics Express, 2007. 15(25): p. 17163-17170.

3. G. Konstantatos, I. Howard, A. Fischer, S. Hoogland, J. Clifford, E. Klem, L. Levina and E. H. Sargent, *Ultrasensitive solution-cast quantum dot photodetectors.* Nature, 2006. 442(7099): p. 180-183.

4. T. Osedach, S. Geyer, J. Ho, A. Arango, M. G. Bawendi and V. Bulovic, *Lateral heterojunction photodetector consisting of molecular organic and colloidal quantum dot thin films.* Applied Physics Letters, 2009. 94(4): p. 043307.

5. E. A. Weiss, R. C. Chiechi, S. M. Geyer, V. J. Porter, D. C. Bell, M. G. Bawendi and G. M. Whitesides, *Size-dependent charge collection in junctions containing single-size and multi-size arrays of colloidal CdSe quantum dots.* Journal of the American Chemical Society, 2008. 130(1): p. 74-82.

6. I. Gur, N. A. Fromer, M. L. Geier and A. P. Alivisatos, *Air-Stable All-Inorganic Nanocrystal Solar Cells Processed from Solution.* Science, 2005. 310(5747): p. 462-465.

7. P. T. Snee, Y. Chan, D. G. Nocera and M. G. Bawendi, *Whispering-Gallery-Mode Lasing from a Semiconductor Nanocrystal/Microsphere Resonator Composite.* Advanced Materials, 2005. 17(9): p. 1131-1136.

8. B. O. Dabbousi, J. Rodriguez-Viejo, F. V. Mikulec, J. R. Heine, H. Mattoussi, R. Ober, K. F. Jensen and M. G. Bawendi, *(CdSe)ZnS Core-Shell Quantum Dots: Synthesis and Characterization of a Size Series of Highly Luminescent Nanocrystallites.* The Journal of Physical Chemistry B, 1997. 101(46): p. 9463-9475.

9. M. A. Hines and P. Guyot-Sionnest, *Synthesis and Characterization of Strongly Luminescing ZnS-Capped CdSe Nanocrystals.* The Journal of Physical Chemistry, 1996. 100(2): p. 468-471.

10. C. B. Murray, D. J. Norris and M. G. Bawendi, *Synthesis and characterization of nearly monodisperse CdE (E = sulfur, selenium, tellurium) semiconductor nanocrystallites.* Journal of the American Chemical Society, 1993. 115(19): p.

8706-8715.

11. C. N. R. Rao, P. J. Thomas and G. U. Kulkarni, *Nanocrystals: Synthesis, Properties, and Applications*. Springer Series in Material Science. 2007: Springer-Verlag Berlin Heidelberg.

12. M. Drndic, M. V. Jarosz, N. Y. Morgan, M. A. Kastner and M. G. Bawendi, *Transport properties of annealed CdSe colloidal nanocrystal solids.* Journal of Applied Physics, 2002. 92(12): p. 7498-7503.

13. M. V. Jarosz, N. E. Stott, M. Drndic, N. Y. Morgan, M. A. Kastner and M. G. Bawendi, *Observation of Bimolecular Carrier Recombination Dynamics in Close-Packed Films of Colloidal CdSe Nanocrystals.* The Journal of Physical Chemistry B, 2003. 107(46): p. 12585-12588.

14. V. J. Porter, S. Geyer, J. E. Halpert, M. A. Kastner and M. G. Bawendi, *Photoconduction in annealed and chemically treated CdSe/ZnS inorganic nanocrystal films.* Journal of Physical Chemistry C, 2008. 112(7): p. 2308-2316.

15. M. Nirmal, B. O. Dabbousi, M. G. Bawendi, J. J. Macklin, J. K. Trautman, T. D. Harris and L. E. Brus, *Fluorescence intermittency in single cadmium selenide nanocrystals.* Nature, 1996. 383(6603): p. 802-804.

16. R. H. Bube, *Photoconductivity of Solids*. 1960: John Wiley & Sons, INC.

17. V. K. LaMer and R. H. Dinegar, *Theory, Production and Mechanism of Formation of Monodispersed Hydrosols.* Journal of the American Chemical Society, 1950. 72(11): p. 4847-4854.

18. C. B. Murray, C. R. Kagan and M. G. Bawendi, *Synthesis And Characterization of Monodisperse Nanocrystals And Close-Packed Nanocrystal Assemblies.* Annual Review of Materials Science, 2000. 30(1): p. 545-610.

19. L. Manna, Wang, R. Cingolani and A. P. Alivisatos, *First-Principles Modeling of Unpassivated and Surfactant-Passivated Bulk Facets of Wurtzite CdSe:â€‰ A Model System for Studying the Anisotropic Growth of CdSe Nanocrystals.* The Journal of Physical Chemistry B, 2005. 109(13): p. 6183-6192.

20. W. Ostwald, *Lehrbuch der Allgemeinen Chemie*. Vol. 2. 1896.

21. W. Ostwald, *Studien uber die Bildung und Umwandlung fester Korper.* Z. Phys. Chem., 1897. 22: p. 289.

22. R. Boistelle and J. P. Astier, *Crystallization mechanisms in solution.* Journal of Crystal Growth, 1988. 90(1-3): p. 14-30.

23. Y. Yin and A. P. Alivisatos, *Colloidal nanocrystal synthesis and the organic-inorganic*

interface. Nature, 2005. 437(7059): p. 664-670.

24. B. von Holt, S. Kudera, A. Weiss, T. E. Schrader, L. Manna, W. J. Parak and M. Braun, *Ligand exchange of CdSe nanocrystals probed by optical spectroscopy in the visible and mid-IR.* Journal of Materials Chemistry, 2008. 18(23): p. 2728-2732.

25. K. Kim, J. Y. Woo, S. Jeong and C.-S. Han, *Photoenhancement of a Quantum Dot Nanocomposite via UV Annealing and its Application to White LEDs.* Advanced Materials, 2011. 23(7): p. 911-914.

26. M. Green, *The nature of quantum dot capping ligands.* Journal of Materials Chemistry, 2010. 20(28): p. 5797-5809.

27. G. Ouyang, W. G. Zhu, C. Q. Sun, Z. M. Zhu and S. Z. Liao, *Atomistic origin of lattice strain on stiffness of nanoparticles.* Physical Chemistry Chemical Physics, 2010. 12(7): p. 1543-1549.

28. R. Osovsky, D. Cheskis, V. Kloper, A. Sashchiuk, M. Kroner and E. Lifshitz, *Continuous-Wave Pumping of Multiexciton Bands in the Photoluminescence Spectrum of a Single CdTe-CdSe Core-Shell Colloidal Quantum Dot.* Physical Review Letters, 2009. 102(19): p. 197401.

29. P. Reiss, M. Protière and L. Li, *Core/Shell Semiconductor Nanocrystals.* Small, 2009. 5(2): p. 154-168.

30. R. F. Egerton, *Physical Principles of Electron Microscopy*. 2005: Springer.

31. C. B. Murray, *Watching Nanocrystals Grow.* Science, 2009. 324(5932): p. 1276-1277.

32. J. E. Evans, K. L. Jungjohann, N. D. Browning and I. Arslan, *Controlled Growth of Nanoparticles from Solution with In Situ Liquid Transmission Electron Microscopy.* Nano Letters, 2011: p. null-null.

33. N. W. Ashcroft and N. D. Mermin, *Solid State Physics*. 1976: Brooks Cole.

34. N. Bohr, *On the Constitution of Atoms and Molecules, Part II Systems Containing Only a Single Nucleus.* Philosophical Magazine, 1913. 26: p. 476-502.

35. A. L. Efros and M. Rosen, *The Electronic Structure of Semiconductor Nanocrystals.* Annual Review of Materials Science, 2000. 30(1): p. 475-521.

36. A. M. Smith and S. Nie, *Semiconductor Nanocrystals: Structure, Properties, and Band Gap Engineering.* Accounts of Chemical Research, 2009. 43(2): p. 190-200.

37. O. Millo, D. Katz, D. Steiner, E. Rothenberg, T. Mokari, M. Kazes and U. Banin, *Charging and quantum size effects in tunnelling and optical spectroscopy of CdSe*

nanorods. Nanotechnology, 2004. 15(1): p. R1.

38. R. Rossetti, J. L. Ellison, J. M. Gibson and L. E. Brus, *Size effects in the excited electronic states of small colloidal CdS crystallites.* The Journal of Chemical Physics, 1984. 80(9): p. 4464-4469.

39. D. Sergi, *Energy transport and fluctuations in small conductors.* Physical Review B, 2011. 83(3): p. 033401.

40. M. Buttiker, Y. Imry, R. Landauer and S. Pinhas, *Generalized many-channel conductance formula with application to small rings.* Physical Review B, 1985. 31(10): p. 6207.

41. D. J. Norris and M. G. Bawendi, *Measurement and assignment of the size-dependent optical spectrum in CdSe quantum dots.* Physical Review B, 1996. 53(24): p. 16338-16346.

42. W. W. Yu, L. Qu, W. Guo and X. Peng, *Experimental Determination of the Extinction Coefficient of CdTe, CdSe, and CdS Nanocrystals.* Chemistry of Materials, 2003. 15(14): p. 2854-2860.

43. J. van Embden, J. Jasieniak and P. Mulvaney, *Mapping the Optical Properties of CdSe/CdS Heterostructure Nanocrystals: The Effects of Core Size and Shell Thickness.* Journal of the American Chemical Society, 2009. 131(40): p. 14299-14309.

44. P. Frantsuzov, M. Kuno, B. Janko and R. A. Marcus, *Universal emission intermittency in quantum dots, nanorods and nanowires.* Nat Phys, 2008. 4(5): p. 519-522.

45. A. L. Efros and M. Rosen, *Random Telegraph Signal in the Photoluminescence Intensity of a Single Quantum Dot.* Physical Review Letters, 1997. 78(6): p. 1110.

46. S. Wang, C. Querner, M. D. Fischbein, L. Willis, D. S. Novikov, C. H. Crouch and M. Drndic, *Blinking Statistics Correlated with Nanoparticle Number.* Nano Letters, 2008. 8(11): p. 4020-4026.

47. C. Querner, S. Wang, K. Healy, J. A. Fairfield, M. D. Fischbein and M. DrndicÌ • , *Fluorescence Dynamics of Semiconductor Nanorod Clusters Studied by Correlated Atomic Force, Transmission Electron, and Fluorescence Microscopy.* The Journal of Physical Chemistry C, 2008. 112(50): p. 19945-19956.

48. S. Wang, C. Querner, T. Dadosh, C. H. Crouch, D. S. Novikov and M. Drndic, *Collective fluorescence enhancement in nanoparticle clusters.* Nat Commun, 2011. 2: p. 364.

49. X. Wang, X. Ren, K. Kahen, M. A. Hahn, M. Rajeswaran, S. Maccagnano-Zacher, J. Silcox, G. E. Cragg, A. L. Efros and T. D. Krauss, *Non-blinking semiconductor*

nanocrystals. Nature, 2009. 459(7247): p. 686-689.

50. S. Wu, G. Han, D. J. Milliron, S. Aloni, V. Altoe, D. V. Talapin, B. E. Cohen and P. J. Schuck, *Non-blinking and photostable upconverted luminescence from single lanthanide-doped nanocrystals.* Proceedings of the National Academy of Sciences, 2009. 106(27): p. 10917-10921.

51. S. Hohng and T. Ha, *Near-Complete Suppression of Quantum Dot Blinking in Ambient Conditions.* Journal of the American Chemical Society, 2004. 126(5): p. 1324-1325.

52. H. Steinberg, O. Wolf, A. Faust, A. Salant, Y. Lilach, O. Millo and U. Banin, *Electrical Current Switching in Single CdSe Nanorods.* Nano Letters, 2010. 10(7): p. 2416-2420.

53. P.-E. Trudeau, M. Sheldon, V. Altoe and A. P. Alivisatos, *Electrical Contacts to Individual Colloidal Semiconductor Nanorods.* Nano Letters, 2008. 8(7): p. 1936-1939.

54. U. Banin and O. Millo, *Tunneling And Optical Spectroscopy of Semiconductor Nanocrystals.* Annual Review of Physical Chemistry, 2003. 54(1): p. 465-492.

55. P. Liljeroth, P. A. Z. van Emmichoven, S. G. Hickey, H. Weller, B. Grandidier, G. Allan, D. Vanmaekelbergh and euml, *Density of States Measured by Scanning-Tunneling Spectroscopy Sheds New Light on the Optical Transitions in PbSe Nanocrystals.* Physical Review Letters, 2005. 95(8): p. 086801.

56. L. Jdira, K. Overgaag, J. Gerritsen, D. l. Vanmaekelbergh, P. Liljeroth and S. Speller, *Scanning Tunnelling Spectroscopy on Arrays of CdSe Quantum Dots: Response of Wave Functions to Local Electric Fields.* Nano Letters, 2008. 8(11): p. 4014-4019.

57. F. Gao, *Effects of quantum confinement and shape on band gap of core/shell quantum dots and nanowires.* Applied Physics Letters, 2011. 98(19): p. 193105.

58. N. Y. Morgan, C. A. Leatherdale, M. Drndic, M. V. Jarosz, M. A. Kastner and M. G. Bawendi, *Electronic transport in films of colloidal CdSe nanocrystals.* Physical Review B, 2002. 66(7): p. 075339.

59. A. Carbone and P. Mazzetti, *Current noise in barrier photoconducting devices. II. Experiment.* Physical Review B, 1994. 49(11): p. 7603.

60. A. K. Podborska, M. F. Oszajca, S. A. Gaweda and K. T. Szaciłowski, *Nanoparticles with logic and numeracy: towards 'computer-on-a-particle' optoelectronic devices.* IET Circuits, Devices & Systems, 2011. 5(2): p. 103-114.

61. P. Tyagi, R. R. Cooney, S. L. Sewall, D. M. Sagar, J. I. Saari and P. Kambhampati,

Controlling Piezoelectric Response in Semiconductor Quantum Dots via Impulsive Charge Localization. Nano Letters, 2010. 10(8): p. 3062-3067.

62. M. Califano, *Photoinduced Surface Trapping and the Observed Carrier Multiplication Yields in Static CdSe Nanocrystal Samples.* ACS Nano, 2011. 5(5): p. 3614-3621.

63. R. Beaulac, L. Schneider, P. I. Archer, G. Bacher and D. R. Gamelin, *Light-Induced Spontaneous Magnetization in Doped Colloidal Quantum Dots.* Science, 2009. 325(5943): p. 973-976.

64. A. Gasperin, E. Amat, M. Porti, J. Martin-Martinez, M. Nafria, X. Aymerich and A. Paccagnella, *Effects of the Localization of the Charge in Nanocrystal Memory Cells.* IEEE Transactions on Electron Devices, 2009. 56(10): p. 2319-2326.

65. W. A. Tisdale and X.-Y. Zhu, *Artificial atoms on semiconductor surfaces.* Proceedings of the National Academy of Sciences, 2011. 108(3): p. 965-970.

66. M. V. Kovalenko, M. Scheele and D. V. Talapin, *Colloidal Nanocrystals with Molecular Metal Chalcogenide Surface Ligands.* Science, 2009. 324(5933): p. 1417-1420.

67. D. V. Talapin and C. B. Murray, *PbSe Nanocrystal Solids for n- and p-Channel Thin Film Field-Effect Transistors.* Science, 2005. 310(5745): p. 86-89.

68. M. D. Fischbein, *Nanocrystal Quantum Dot Electronics and Nanofabrication by Electron Beam Ablation*, in *Physics and Astronomy*. 2009, Unverisity of Pennsylvania: Philadelphia.

69. R. Parthasarathy, X.-M. Lin, K. Elteto, T. F. Rosenbaum and H. M. Jaeger, *Percolating through Networks of Random Thresholds: Finite Temperature Electron Tunneling in Metal Nanocrystal Arrays.* Physical Review Letters, 2004. 92(7): p. 076801.

70. N. F. Mott, *Conduction in non-crystalline materials.* Philosophical Magazine, 1969. 19.

71. N. F. Mott and E. A. Davis, *Electronic Processes in Non-crystalline Materials*. 1979: Oxford University Press.

72. H. Liu, A. Pourret and P. Guyot-Sionnest, *Mott and Efros-Shklovskii Variable Range Hopping in CdSe Quantum Dots Films.* ACS Nano, 2010. 4(9): p. 5211-5216.

73. A. L. E. a. B. I. Shklovskii, *Coulomb gap and low temperature conductivity of disordered systems.* Journal of Physics C: Solid State Physics, 1975. 8(4): p. L49.

74. J. Zhang and B. I. Shklovskii, *Density of states and conductivity of a granular metal*

or an array of quantum dots. Physical Review B, 2004. 70(11): p. 115317.

75. A. Persano, G. Leo, L. Manna and A. Cola, *Charge carrier transport in thin films of colloidal CdSe quantum rods.* Journal of Applied Physics, 2008. 104(7): p. 074306-074306.

76. M. D. Fischbein and M. Drndic, *Nanogaps by direct lithography for high-resolution imaging and electronic characterization of nanostructures.* Applied Physics Letters, 2006. 88(6): p. 063116-063113.

77. V. I. Klimov, *Semiconductor and Metal Nanocrystals: Synthesis and Electronic and Optical Properties*. 2003: CRC Press.

78. B. S. Kim, M. A. Islam, L. E. Brus and I. P. Herman, *Interdot interactions and band gap changes in CdSe nanocrystal arrays at elevated pressure.* Journal of Applied Physics, 2001. 89(12): p. 8127-8140.

79. L. E. Brus, *Electron--electron and electron-hole interactions in small semiconductor crystallites: The size dependence of the lowest excited electronic state.* The Journal of Chemical Physics, 1984. 80(9): p. 4403-4409.

80. M. D. Fischbein and M. Drndic, *CdSe nanocrystal quantum-dot memory.* Applied Physics Letters, 2005. 86(19): p. 193106-193103.

81. M. D. Fischbein and M. Drndic, *Sub-10 nm device fabrication in a transmission electron microscope.* Nano Letters, 2007. 7(5): p. 1329-1337.

82. C. A. Leatherdale, C. R. Kagan, N. Y. Morgan, S. A. Empedocles, M. A. Kastner and M. G. Bawendi, *Photoconductivity in CdSe quantum dot solids.* Physical Review B, 2000. 62(4): p. 2669.

83. S. Li, M. L. Steigerwald and L. E. Brus, *Surface States in the Photoionization of High-Quality CdSe Core/Shell Nanocrystals.* ACS Nano, 2009. 3(5): p. 1267-1273.

84. H. Ye, H. S. Park, V. A. Akhavan, B. W. Goodfellow, M. G. Panthani, B. A. Korgel and A. J. Bard, *Photoelectrochemical Characterization of CuInSe2 and Cu(In1â^'xGax)Se2 Thin Films for Solar Cells.* The Journal of Physical Chemistry C, 2011. 115(1): p. 234-240.

85. A. Dong, J. Chen, P. M. Vora, J. M. Kikkawa and C. B. Murray, *Binary nanocrystal superlattice membranes self-assembled at the liquid-air interface.* Nature, 2010. 466(7305): p. 474-477.

86. B. Gudden and R. Pohl, *Lichtelektrische Beobachtungen an isolierenden Metallsulfiden.* Zeitschrift für Physik A Hadrons and Nuclei, 1920. 2(4): p. 361-372.

87. J. Aldana, Y. A. Wang and X. Peng, *Photochemical Instability of CdSe Nanocrystals Coated by Hydrophilic Thiols.* Journal of the American Chemical Society, 2001. 123(36): p. 8844-8850.

88. K. Kohary and G. A. Gibson, *Modelling photooxidation of CdSe-ZnS nanocrystals.* physica status solidi (c), 2011. 8: p. n/a-n/a.

89. D. Yu, C. Wang and P. Guyot-Sionnest, *n-Type Conducting CdSe Nanocrystal Solids.* Science, 2003. 300(5623): p. 1277-1280.

90. C. T. Black, C. B. Murray, R. L. Sandstrom and S. Sun, *Spin-Dependent Tunneling in Self-Assembled Cobalt-Nanocrystal Superlattices.* Science, 2000. 290(5494): p. 1131-1134.

91. P. Vettiger, M. Despont, U. Drechsler, U. Durig, W. Haberle, M. I. Lutwyche, H. E. Rothuizen, R. Stutz, R. Widmer and G. K. Binnig, *The "Millipede" - More than thousand tips for future AFM storage.* IBM Journal of Research and Development, 2000. 44(3): p. 323-340.

92. A. J. M. Giesbers, U. Zeitler, S. Neubeck, F. Freitag, K. S. Novoselov and J. C. Maan, *Nanolithography and manipulation of graphene using an atomic force microscope.* Solid State Communications, 2008. 147(9-10): p. 366-369.

93. L. Weng, L. Zhang, Y. P. Chen and L. P. Rokhinson, *Atomic force microscope local oxidation nanolithography of graphene.* Applied Physics Letters, 2008. 93(9): p. 093107-093103.

94. S. Wang, *Fluorescence Properties of Blinking Semiconducting Nanoparticles and Interaction Effects*, in *Physics and Astronomy*. 2011, University of Pennsylvania: Philadelphia.

95. O. Cherniavskaya, L. Chen, V. Weng, L. Yuditsky and L. E. Brus, *Quantitative Noncontact Electrostatic Force Imaging of Nanocrystal Polarizability.* The Journal of Physical Chemistry B, 2003. 107(7): p. 1525-1531.

96. D. Bonnell, *Scanning Probe Microscopy and Spectroscopy: Theory, Techniques, and Applications*. 2000: Wiley, John & Sons.

97. Z. Hu, M. D. Fischbein and M. Drndic, *Local Charge Transport in Two-Dimensional PbSe Nanocrystal Arrays Studied by Electrostatic Force Microscopy.* Nano Letters, 2005. 5(7): p. 1463-1468.

98. M. D. Fischbein, M. Puster and M. Drndic, *Monolayer Suppression of Transport Imaged in Annealed PbSe Nanocrystal Arrays.* Nano Letters, 2009. 10(6): p. 2155-2161.

99. T. D. Krauss and L. E. Brus, *Charge, Polarizability, and Photoionization of Single*

Semiconductor Nanocrystals. Physical Review Letters, 1999. 83(23): p. 4840.

100. O. Madelung, U. Rössler and M. Schulz, *Non-Tetrahedrally Bonded Elements and Binary Compounds I*. Vol. III/41C. 1998, Berlin, Germany: Springer-Verlag.

101. T. A. Witten and L. M. Sander, *Diffusion-Limited Aggregation, a Kinetic Critical Phenomenon.* Physical Review Letters, 1981. 47(19): p. 1400.

102. K. Elteto, X.-M. Lin and H. M. Jaeger, *Electronic transport in quasi-one-dimensional arrays of gold nanocrystals.* Physical Review B, 2005. 71(20): p. 205412.

103. M. Lunz, V. A. Gerard, Y. K. Gun'ko, V. Lesnyak, N. Gaponik, A. S. Susha, A. L. Rogach and A. L. Bradley, *Surface Plasmon Enhanced Energy Transfer between Donor and Acceptor CdTe Nanocrystal Quantum Dot Monolayers.* Nano Letters, 2011. 11(8): p. 3341-3345.

104. D. E. Gomez, K. C. Vernon, P. Mulvaney and T. J. Davis, *Surface Plasmon Mediated Strong Exciton-Photon Coupling in Semiconductor Nanocrystals.* Nano Letters, 2009. 10(1): p. 274-278.

105. C.-C. Chang, Y. D. Sharma, Y.-S. Kim, J. A. Bur, R. V. Shenoi, S. Krishna, D. Huang and S.-Y. Lin, *A Surface Plasmon Enhanced Infrared Photodetector Based on InAs Quantum Dots.* Nano Letters, 2010. 10(5): p. 1704-1709.

106. E. Hwang, I. I. Smolyaninov and C. C. Davis, *Surface Plasmon Polariton Enhanced Fluorescence from Quantum Dots on Nanostructured Metal Surfaces.* Nano Letters, 2010. 10(3): p. 813-820.

107. J. M. McMahon, S. K. Gray and G. C. Schatz, *Fundamental behavior of electric field enhancements in the gaps between closely spaced nanostructures.* Physical Review B, 2011. 83(11): p. 115428.

108. K. A. Willets and R. P. Van Duyne, *Localized Surface Plasmon Resonance Spectroscopy and Sensing.* Annual Review of Physical Chemistry, 2007. 58(1): p. 267-297.

109. J. Homola, S. S. Yee and G. Gauglitz, *Surface plasmon resonance sensors: review.* Sensors and Actuators B: Chemical, 1999. 54(1-2): p. 3-15.

110. M. G. Albrecht and J. A. Creighton, *Anomalously intense Raman spectra of pyridine at a silver electrode.* Journal of the American Chemical Society, 1977. 99(15): p. 5215-5217.

111. D. K. Gramotnev and S. I. Bozhevolnyi, *Plasmonics beyond the diffraction limit.* Nat Photon, 2010. 4(2): p. 83-91.

112. U. Kreibig and M. Vollmer, *Optical Properties of Metal Clusters*. Springer Series in Materials Science. 1995: Springer. 552.

113. G. Mie, *Beiträge zur Optik trüber Medien, speziell kolloidaler Metallösungen.* Ann. Physik, 1908. 4(25).

114. C. F. Bohren and D. R. Huffman, *Absorption and Scattering of Light by Small Particles*. 1983: John Wiley & Sons, Inc.

115. J. M. Luther, P. K. Jain, T. Ewers and A. P. Alivisatos, *Localized surface plasmon resonances arising from free carriers in doped quantum dots.* Nature Materials, 2011. 10(5): p. 361-366.

116. P. Rebentrost, M. Stopa and A. n. Aspuru-Guzik, *Forster Coupling in Nanoparticle Excitonic Circuits.* Nano Letters, 2010. 10(8): p. 2849-2856.

117. P. Banerjee, D. Conklin, S. Nanayakkara, T.-H. Park, M. J. Therien and D. A. Bonnell, *Plasmon-Induced Electrical Conduction in Molecular Devices.* ACS Nano, 2010. 4(2): p. 1019-1025.

118. P. K. Jain, W. Huang and M. A. El-Sayed, *On the Universal Scaling Behavior of the Distance Decay of Plasmon Coupling in Metal Nanoparticle Pairs: A Plasmon Ruler Equation.* Nano Letters, 2007. 7(7): p. 2080-2088.

119. J. Yao, A.-P. Le, S. K. Gray, J. S. Moore, J. A. Rogers and R. G. Nuzzo, *Functional Nanostructured Plasmonic Materials.* Advanced Materials, 2010. 22(10): p. 1102-1110.

120. M. G. Bawendi, P. J. Carroll, W. L. Wilson and L. E. Brus, *Luminescence properties of CdSe quantum crystallites: Resonance between interior and surface localized states.* The Journal of Chemical Physics, 1992. 96(2): p. 946-954.

121. M. V. Jarosz, V. J. Porter, B. R. Fisher, M. A. Kastner and M. G. Bawendi, *Photoconductivity studies of treated CdSe quantum dot films exhibiting increased exciton ionization efficiency.* Physical Review B, 2004. 70(19): p. 195327.

122. S. A. Crooker, T. Barrick, J. A. Hollingsworth and V. I. Klimov, *Multiple temperature regimes of radiative decay in CdSe nanocrystal quantum dots: Intrinsic limits to the dark-exciton lifetime.* Applied Physics Letters, 2003. 82(17): p. 2793-2795.

123. S. A. Crooker, J. A. Hollingsworth, S. Tretiak and V. I. Klimov, *Spectrally Resolved Dynamics of Energy Transfer in Quantum-Dot Assemblies: Towards Engineered Energy Flows in Artificial Materials.* Physical Review Letters, 2002. 89(18): p. 186802.

124. V. I. Klimov, *Optical Nonlinearities and Ultrafast Carrier Dynamics in*

Semiconductor Nanocrystals. The Journal of Physical Chemistry B, 2000. 104(26): p. 6112-6123.

125. L. J. Willis, J. A. Fairfield, T. Dadosh, M. D. Fischbein and M. Drndic, *Controlling Nanogap Quantum Dot Photoconductivity through Optoelectronic Trap Manipulation.* Nano Letters, 2009. 9(12): p. 4191-4197.

126. D. J. Norris and M. G. Bawendi, *Structure in the lowest absorption feature of CdSe quantum dots.* The Journal of Chemical Physics, 1995. 103(13): p. 5260-5268.

127. T. J. Liptay, L. F. Marshall, P. S. Rao, R. J. Ram and M. G. Bawendi, *Anomalous stokes shift in CdSe nanocrystals.* Physical Review B, 2007. 76(15): p. 7.

128. J. A. Fairfield, T. Dadosh and M. Drndic, *Characterization of memory and measurement history in photoconductivity of nanocrystal arrays.* Applied Physics Letters, 2010. 97(14): p. 143112-143113.

129. J. Jasieniak, L. Smith, J. v. Embden, P. Mulvaney and M. Califano, *Re-examination of the Size-Dependent Absorption Properties of CdSe Quantum Dots.* The Journal of Physical Chemistry C, 2009. 113(45): p. 19468-19474.

130. A. Carbone and P. Mazzetti, *Current noise in barrier photoconducting devices. I. Theory.* Physical Review B, 1994. 49(11): p. 7592.

131. A. Carbone and P. Mazzetti, *Current noise spectroscopy of deep energy levels in photoconductors.* Journal of Applied Physics, 1996. 80(3): p. 1559-1566.

132. M. Jones, J. Nedeljkovic, R. J. Ellingson, A. J. Nozik and G. Rumbles, *Photoenhancement of Luminescence in Colloidal CdSe Quantum Dot Solutions.* The Journal of Physical Chemistry B, 2003. 107(41): p. 11346-11352.

133. P. Chin, T. Buckle, A. de Miguel, S. Meskers, R. Janssen and F. van Leeuwen, *Dual Emissive Quantum Dots for Multispectral Intraoperative Fluorescence Imaging.* Biomaterials, 2010. 31(26): p. 6823-6832.

134. A. Carbone and P. Mazzetti, *Grain-boundary effects on photocurrent fluctuations in polycrystalline photoconductors.* Physical Review B, 1998. 57(4): p. 2454.

135. M. A. White, A. L. Weaver, R. m. Beaulac and D. R. Gamelin, *Electrochemically Controlled Auger Quenching of Mn2+ Photoluminescence in Doped Semiconductor Nanocrystals.* ACS Nano, 2011. 5(5): p. 4158-4168.

136. D. Mocatta, G. Cohen, J. Schattner, O. Millo, E. Rabani and U. Banin, *Heavily Doped Semiconductor Nanocrystal Quantum Dots.* Science, 2011. 332(6025): p. 77-81.

137. E. Talgorn, M. A. de Vries, L. D. A. Siebbeles and A. J. Houtepen,

Photoconductivity Enhancement in Multilayers of CdSe and CdTe Quantum Dots. ACS Nano, 2011. 5(5): p. 3552-3558.

138. D. A. R. Barkhouse, R. Debnath, I. J. Kramer, D. Zhitomirsky, A. G. Pattantyus-Abraham, L. Levina, L. Etgar, M. Grätzel and E. H. Sargent, *Depleted Bulk Heterojunction Colloidal Quantum Dot Photovoltaics.* Advanced Materials, 2011: p. n/a-n/a.

139. J. Jasieniak, B. I. MacDonald, S. E. Watkins and P. Mulvaney, *Solution-Processed Sintered Nanocrystal Solar Cells via Layer-by-Layer Assembly.* Nano Letters, 2011.

140. C. Lee, X. Wei, J. W. Kysar and J. Hone, *Measurement of the Elastic Properties and Intrinsic Strength of Monolayer Graphene*. 2008. p. 385-388.

141. A. H. Castro Neto, F. Guinea, N. M. R. Peres, K. S. Novoselov and A. K. Geim, *The electronic properties of graphene.* Reviews of Modern Physics, 2009. 81(1): p. 109.

142. A. Vakil and N. Engheta, *Transformation Optics Using Graphene.* Science, 2011. 332(6035): p. 1291-1294.

143. F. Bonaccorso, Z. Sun, T. Hasan and A. C. Ferrari, *Graphene photonics and optoelectronics.* Nat Photon, 2010. 4(9): p. 611-622.

144. F. Xia, T. Mueller, Y.-m. Lin, A. Valdes-Garcia and P. Avouris, *Ultrafast graphene photodetector.* Nature Nanotechnology, 2009. 4(12): p. 839-843.

145. F. Schedin, E. Lidorikis, A. Lombardo, V. G. Kravets, A. K. Geim, A. N. Grigorenko, K. S. Novoselov and A. C. Ferrari, *Surface-Enhanced Raman Spectroscopy of Graphene.* ACS Nano, 2010. 4(10): p. 5617-5626.

146. B. Chitara, L. S. Panchakarla, S. B. Krupanidhi and C. N. R. Rao, *Infrared Photodetectors Based on Reduced Graphene Oxide and Graphene Nanoribbons.* Advanced Materials, 2011: p. n/a-n/a.

147. A. N. Obraztsov, *Chemical vapour deposition: Making graphene on a large scale.* Nat Nano, 2009. 4(4): p. 212-213.

148. Z. Luo, Y. Lu, D. W. Singer, M. E. Berck, L. A. Somers, B. R. Goldsmith and A. T. C. Johnson, *Effect of Substrate Roughness and Feedstock Concentration on Growth of Wafer-Scale Graphene at Atmospheric Pressure.* Chemistry of Materials, 2011. 23(6): p. 1441-1447.

149. Z. Chen, S. p. Berciaud, C. Nuckolls, T. F. Heinz and L. E. Brus, *Energy Transfer from Individual Semiconductor Nanocrystals to Graphene.* ACS Nano, 2010. 4(5): p. 2964-2968.

150. G. Williams and P. V. Kamat, *Graphene-Semiconductor Nanocomposites: Excited-State Interactions between ZnO Nanoparticles and Graphene Oxide.* Langmuir, 2009. 25(24): p. 13869-13873.

151. H. Dong, W. Gao, F. Yan, H. Ji and H. Ju, *Fluorescence Resonance Energy Transfer between Quantum Dots and Graphene Oxide for Sensing Biomolecules.* Analytical Chemistry, 2010. 82(13): p. 5511-5517.

152. R. R. Nair, P. Blake, A. N. Grigorenko, K. S. Novoselov, T. J. Booth, T. Stauber, N. M. R. Peres and A. K. Geim, *Fine Structure Constant Defines Visual Transparency of Graphene.* Science, 2008. 320(5881): p. 1308.

153. K. F. Mak, M. Y. Sfeir, Y. Wu, C. H. Lui, J. A. Misewich and T. F. Heinz, *Measurement of the Optical Conductivity of Graphene.* Physical Review Letters, 2008. 101(19): p. 196405.

154. W. Ren, Y. Fang and E. Wang, *A Binary Functional Substrate for Enrichment and Ultrasensitive SERS Spectroscopic Detection of Folic Acid Using Graphene Oxide/Ag Nanoparticle Hybrids.* ACS Nano, 2011: p. null-null.

155. S. Sun, L. Gao, Y. Liu and J. Sun, *Assembly of CdSe nanoparticles on graphene for low-temperature fabrication of quantum dot sensitized solar cell.* Applied Physics Letters, 2011. 98.

156. H. Kroemer, *Nobel Lecture: Quasielectric fields and band offsets: teaching electrons new tricks.* Reviews of Modern Physics, 2001. 73(3): p. 783.